AN INVESTIGATION OF OPTICAL PROPERTIES OF POROUS SILICON: REFRACTIVE INDEX, PHOTOLUMINESCENCE AND RAMAN SCATTERING STUDIES

J ANTO PRADEEP

A THESIS SUBMITTED FOR THE AWARD OF

DOCTOR OF PHILOSOPHY

DEPARTMENT OF PHYSICS
INDIAN INSTITUTE OF TECHNOLOGY GUWAHATI
GUWAHATI – 781 039, INDIA

SEPTEMBER, 2011

DECLARATION

The work contained in this thesis entitled **"An Investigation of Optical Properties of Porous Silicon: Refractive Index, Photoluminescence and Raman Scattering Studies"** has been carried out by me under the supervision of Dr. Pratima Agarwal, Associate Professor, Department of Physics, Indian Institute of Technology, Guwahati, Assam, India. This thesis does not contain any material previously submitted for the award of any degree or diploma.

Date:

J Anto Pradeep
Department of Physics
Indian Institute of Technology Guwahati
Guwahati, India

TH-1099_04612102

भारतीय प्रौद्योगिकी संस्थान गुवाहाटी
Indian Institute of Technology Guwahati
North Guwahati, Guwahati
PIN- 781 039, Assam State, INDIA
Phone: +91 361 2583000 Extn 2702, 2582702
Fax: +91 361 2690 762(Institute), 2582749(Department)

Dr. Pratima Agarwal
Associate Professor
Department of Physics
E-mail: pratima@iitg.ernet.in

CERTIFICATE

This is certified that the work contained in this thesis entitled **"An Investigation of Optical Properties of Porous Silicon: Refractive Index, Photoluminescence and Raman Scattering Studies"** submitted by Mr. J Anto Pradeep, a Ph. D. student in the Department of Physics, Indian Institute of Technology, Guwahati, Assam, India, for the award of the degree of Doctor of Philosophy has been carried out under my supervision. This work has not been submitted elsewhere for the award of any degree or diploma.

2nd September 2011 (Dr. Pratima Agarwal)

.

TH-1099_04612102

For the love and affection

of my parents

TH-1099_04612102

ACKNOWLEDGEMENTS

I do not know whether or not the thesis is born out of the grace of the Almighty, but I do know that without a few persons for their timely help, fruitful discussions and constant encouragement this thesis would not have been possible. I keep this space to show my sincere gratitude to all those who have contributed for the successful completion of my doctoral thesis work.

First of all I would like to show my deepest gratitude to the thesis supervisor, Dr. Pratima Agarwal, who introduced me to this field of research. Her friendly nature and the freedom she had given me to work on my way might be the reasons that I did not feel any pressure or frustration, even though the present thesis work had taken a little more years than an average doctoral thesis work at the institute. I am greatly benefited with her knowledge and experience. Apart from academic grounds, she had also supported me financially by absorbing me in her research projects when I was found without fellowship. If my thesis had not been under her supervision, I certainly doubt that I could have done it to my full satisfaction.

I thank the members of doctoral committee Dr. Alika Khare, Dr. Saurabh Basu, Dr. G. Krishnamoorthy and Dr. P. S. Robi for regular monitoring of my progress. Their invaluable suggestions for improvement and their questions to deepen the understanding had immensely contributed to bring the thesis to its present form. I also thank all the heads of the department of physics during my academic programme Dr. A. Srinivasan, Dr. Alika Khare, Dr. S. Ravi and Dr. Saurabh Basu for all their support at necessary occasions. I also thank all my course teachers Mr. Britto Inigo, Ms. Chandra, Mr. Vincent, Mr. Dhanraj, Mr. Stalin, Dr. Balakrishnan, Dr. A. Srinivasan, Dr. Saurabh Basu, Dr. P. K. Giri, Dr. C. Kadolkar, Dr. Gin Jose and Dr. Girish Setlur from my elementary studies to the present for all their valuable inputs which had directly or indirectly had contributed to the quality of the doctoral thesis work.

I thank the department of physics for providing a very friendly environment and facilitating an easy access of the research facilities, which had been so beneficial for my thesis work.

TH-1099_04612102

I thank the present and past non-teaching staffs of the department of Physics Dr. Sidananda Sarma, Mr. Lokesh Chakravorthy, Mr. Atul Chandra Deka, Mr. Basab Bijoy Purakayasthya, Mr. Bimal Kumar Sarma, Mr. Panjak Goswami, Mr. Debabratha Purkayastha, Mr. Madan Deka and Mr. Jinto Boro for all their support during the course of the thesis work. Special thanks to Mr. Basab Bijoy Purakayasthya for his help in the familiarization of LabView programming environment during the initial phase of my research, and to Mr. Bimal Kurmar Sarma for his technical assistance in photoluminescence measurements.

I express my sincere thanks also to the staffs of central instruments facility (CIF), IIT Guwahati Dr. Chandan Borhogain, Dr. Kula Senapati, Mr. Madhurjya Bora and Mr. Kesho Singh for all their help during measurements at CIF.

I thank Dr. Ajay Gupta, Dr. Vasananth Sathe and Dr. Sripathi of IUC, Indore for allowing me to use the centre facilities on few of my samples. I also thank Dr. Deshpande and Mr. Manoj for their technical assistance at IUC, Indore.

I was fortunate to have Dr. Bulumoni Kalita, Dr. Purabi Gogoi, Dr. Gouri Sankar Paul, Mr. Himashu Shekhar Jha, Mr. Mukesh Kumar Singh, Mr. Lalhriatzuala, Ms. Asha and Mr. Ramakrishnan as lab mates. They had provided me an ample comfort environment in the lab.

My batchmates Dr. Manos Pratim Chakrapani Kalita, Dr. Sandeep Kumar Srivastava, Dr. Sabitha Mohan, Dr. Rupa Chaterjee and Ms. Krishna Kali Adhikari had made the first year of my stay at IIT Guwahati very enjoyable. During my stay at IIT Guwahati, most of my discussions on many topics of physics were mainly with Dr. Sabitha Mohan and Dr. Manos Pratim Chakrapani Kalita. They both had inspired at many levels, and improved my knowledge on the subject. Dr. Sabitha Mohan was also the one who taught me the importance of light scattering in materials, which actually helped me to formulate my thesis problem.

My stay at hostel would not have been so memorable without my hostel mates Dr. Muneer Ahamed, Dr. Murugadoss, Dr. Saravanan, Dr. William Bosco, Dr. Vadirajan, Dr. Gopinath, Dr. Arumugaperumal, Dr. Monash, Dr. Aadaleesan, Dr. Ashok, Dr. Ramakrishnan, Dr. Santhosh, Dr. Lakshmanan, Dr. Sateesh, Dr. Godfrey, Dr. Dilip Kumar Singh, Mr. Sakthivel, Mr. Agile Mathew and Tapan Mishra. No day ended without a chat

TH-1099_04612102

with Dr. Murugadoss and Dr. Arumugaperumal, until they were in the campus. I had many hot, and sometimes, violent discussions on many topics in chemistry with Dr. Murugadoss. Those discussions had stimulated interest altogether in chemistry. Dr. Murugadoss had also helped me in a few measurements at the department of chemistry, whenever I asked him for the same. Towards the end of my doctoral programme, I got the company of Dr. Monash, Dr. Ashok and Dr. Aadaleesan. Dr. Aadaleesan had been my inspiration for philosophical thoughts. I had several fruitful discussions with him on relativity theory, quantum physics and particle physics topics, though he was an electrical engineer. The time I spent with Dr. Monash and Dr. Ashok were one of the finest moments of my stay at the hostel. We had discussed many topics from religion, history of India, history of tamilnadu, tamil films, songs, music directors, politics, etc. with a plate of cooked chicken in front.

I must also thank my undergraduate friends Mr. Selva Kumar, Mr. Moorthy and Mr. Praveen Kumar and my postgraduate friends Mr. Roopas Kiran and Dr. Surya Prasad for their interest on the progress of my thesis work.

I am grateful to Indian Institute of Technology Guwahati, Department of Science and Technology, India and Board of Research in Fusion Science and Technology for providing me the financial support to carry out the present thesis work.

I had immensely benefited with the internet facilities provided by the institute to student hostels. Browsing over the web was one amongst a few pass times that I had during my stay at the hostel. That had improved my knowledge and interest on many diverse fields.

The list would certainly be incomplete if I end this with no mentioning of my family members. They gave me the moral support for all through the years. Although I did not tell them at anytime my situation at IIT Guwahati and the reasons for the delay in completion of my doctoral programme, they were the ones who understood, believed and had confidence over me than anybody else in the whole world. My elder brother, Mr. Robert Dhiliban, had taken the whole of the family responsibilities on his own shoulders. It was all because of him that I could have a comfortable life at the campus. My wife, Ms. Jacintha, also needs a special mention here. I am grateful for her understanding of my situation during the documentation of my thesis work. She had managed everything all by herself, and with due patience had waited for my coming back home. Her care and

TH-1099_04612102

affection were the reasons that I could able to document the thesis work speedily, which I had never done at anytime.

J Anto Pradeep
Guwahati

Indian Institute of Technology Guwahati

LIST OF PUBLICATIONS

Referred Journals

1. **J Anto Pradeep** and Pratima Agarwal, "Determination of Thickness, Refractive index, and Spectral Scattering of an Inhomogeneous Thin Film with Rough Interfaces", J. Appl. Phys. **108**, 043515 (2010)

2. **J Anto Pradeep** and Pratima Agarwal, "An Alternative Approach to Understand the Photoluminescence and the Photoluminescence Peak Shift with Excitation in Porous Silicon", J. Appl. Phys. **104**, 123515 (2008)

3. **J Anto Pradeep**, Purabi Gogoi and Pratima Agarwal, "Single and Multilayer Porous Silicon for Photonics Applications", J. Non-Cryst. Solids **354**, 2544 (2008)

International Conferences

1. J Anto Pradeep and Pratima Agarwal, "Refractive Index Calculation for Composites and Its Application in Fabricating Porous Silicon based Photonic Structures" in the abstract book of ICANS24, p. 249 (Aug 21–26, 2011 in Nara, Japan)

1. **J Anto Pradeep** and Pratima Agarwal, "Variation of Photoluminescence Peak Centre with the Excitation Energy in Porous Silicon", presented as poster in ICANN 2009 (Dec 9–11, 2009 in IIT Guwahati, India)

2. **J Anto Pradeep** and Pratima Agarwal, "Structural Investigation of Porous Silicon by Raman Scattering Spectroscopy" in the abstract book of ICANS23, p. 275 (Aug 23–28, 2009 in Utrecht, Netherlands)

3. **J Anto Pradeep** and Pratima Agarwal, "Preparation and Characterization of Porous Silicon Single and Multilayer for Photonic Applications", in abstract book of MESODIS06, p. 121 (Dec 04–08, 2006 in IIT Kanpur, India)

National Conferences

1. **J Anto Pradeep**, M Pandey, S M Sharma and Pratima Agarwal, "Effect of Anodization Current Density and Wafer Resistivity on the Raman Scattering in Porous Silicon", in

TH-1099_04612102

proceedings of DAE-SSPS 2009, p. 723 (Dec 14–18, 2009 in The Maharaja Sayajirao University of Baroda, Vadodara, India)

2. **J Anto Pradeep** and Pratima Agarwal, “X-ray Diffraction Studies on Porous Silicon”, in proceedings of DAE-SSPS 2007, p. 395 (Dec 27–31, 2007 in University of Mysore, Mysore, India)

TH-1099_04612102

SYNOPSIS

Porous Si (PS), a composite of Si and void, is known to scientific community ever since A. Uhlir reported his observation during electropolishing of Si in aqueous hydrofluoric acid in 1956. Until 1990, when Canham reported his discovery on PS that certain PS could show efficient visible photoluminescence at room temperature, the interest on PS was based on its possible use as a substrate material for heteroepitaxy. The discovery of Canham has altered the whole scenario from both basic science and applied areas of research. A plethora of research articles, following the discovery of PL from PS, is available in the literature. This is partly due to (i) the presence of Si, a well explored and technologically promising material both in crystalline and amorphous forms of matter, as a constituent (ii) ease and cost effective preparation technique and (iii) the intriguing efficient visible photoluminescence.

Photoluminescence, though considered to be one of the key factors that have stimulated the research interest on PS, the mechanism of the phenomenon is yet a topic of intense debate. Also, the refractive index of PS, which is fundamental to the understanding of processes that involve the interaction of electromagnetic wave with matter, is often overlooked. The determination of refractive index of PS, or in general, any composite is not straight forward. A propagating electromagnetic wave undergoes scattering due to spatial variation of refractive index in the media. The existing procedures for the determination of refractive index from transmittance or specular reflectance spectral measurements inherently consider non-scattering medium, so their applicability to composite is questionable. Also, the calculation of refractive index through effective medium theories has its own drawbacks. Effective medium theories demand a prior knowledge of the optical constants and the occupied volume fractions of all the individual homogeneous components constituting the composite and their microscopic geometry to determine the effective refractive index of the system. Depending on the microscopic geometry, there exist several effective medium theories, each specific to a particular

TH-1099_04612102

microscopic geometry. In reality, no composite would satisfy all the necessities for the applicability of the theory. In PS, the situation is even complicated by the presence of several surface adsorbed chemical species on the exposed Si surfaces. Practically, it is impossible to identify all the chemical species, their optical constants and their occupied volume fractions in PS matrix. These features make the determination of optical constants in PS as a formidable task through effective medium theories.

The present thesis proposes a data analysis procedure, which is not merely applicable to PS but to any composite or inhomogeneous films, for the determination of real part of the dispersion of refractive index $n(\lambda)$, thickness d and incoherent spectral scattering from the interference in transmittance or specular reflectance measurements. The proposal considers the qualities of practical thin films like compositional inhomogeneity resulting in the spatial variation of refractive index over the volume of the material, chemisorption/physisorption of foreign species on the vulnerable interfaces resulting in the refractive index of the interfaces different from the bulk of the material and rough interfaces.

The proposed data analysis procedure for the determination of $n(\lambda)$ and d is used in the characterization of PS layers. The PS layers are prepared on different resistive c-Si wafers (0.001, 0.01, 0.1, 1 and 50 Ω cm) under various current densities (1, 5, 25, 50, 75, 100 and 150 mA/cm^2) with pulsed current electrochemical etching process. As there existed no procedure to determine $n(\lambda)$ and d prior to this work, the thesis presents a systematic study on the effect of wafer resistivity and etching current density on $n(\lambda)$ and the etching rate. The study throws light on the dissolution kinetics of PS formation.

Photoluminescence is one of the most extensively studied phenomena in PS. There exist many controversial ideas for the origin of PL from PS, yet it is widely believed that the effect of quantum confinement persists at the absorption. The present investigation shows a close correspondence of photoluminescence excitation spectrum of PS, which is primarily an alternative to absorption on opaque samples, to that of the absorption spectrum of bulk c-Si. It is from the close correspondence of these spectra, we remark that effect of quantum confinement is not significant in PS. Following, the origin of PL is ascribed to surface states formed by hydrides and oxides bonded to the vulnerable exposed Si surfaces in PS matrix. A small correction in the traditional analysis of photoluminescence excitation spectrum is also pointed out to incorporate the spectral

TH-1099_04612102

reflectivity of the material in the case of solids. The blue shift of the photoluminescence peak centre with the increase in excitation energy is explained based on the quasithermalization and probability of occupation of carriers at the surface states. Several other common observations like increase in luminescence efficiency with aging and porosity are also explained.

Raman scattering (RS) spectroscopy, yet another optical characterization tool, is used for the structural characterization of PS. In Si, the red shift accompanied with a spectral asymmetry in the broadening of $\Gamma_{25'}$ component of the one-phonon RS, in the absence of non-uniform heating, is a clear indication of the presence of low dimensional Si structures. There exists a plethora of experimental data in the literature on the one-phonon RS of PS with a red shift accompanied with a spectral asymmetry in the broadening that has been ascribed to the presence of low dimensional Si structure in the material. The RS measurements, reported in this thesis, are preformed with low laser power so as to minimize the effect of local heating on the spectra. The RS from PS layers, under these conditions, are nearly identical to bulk c-Si. The inference from the spectra contradicts the usual belief on the existence of Si nanostructures in PS matrix.

However, on heavily B-doped Si wafers, where the RS by optical phonons is interfered by the continuum of intervalance electronic transitions, RS from PS show deviations in the asymmetric spectral broadening relative to the bulk counterpart. It is also observed that the deviation increases with the doping concentration and etching current density. This feature of RS from PS on heavily B-doped Si wafers is explained based on the effect of microstructure on the intervalance electronic transitions.

The knowledge on the effect of etching current density on the refractive index, *n* and the etching rate, and the ease of controlling *n* and *d* of PS layers are exploited in preparing the multilayer of PS. A few photonic structures are prepared on heavily B-doped c-Si wafers and are characterized with specular reflectance spectroscopy near around the visible region of the electromagnetic spectrum.

Organization of the thesis

The thesis is organized in eight chapters. Chapter 1, which is the introduction, gives the overall literature perspective of PS, the motivation of the present work and an outline of the work contained in the present thesis. Chapter 2 details the preparation of PS both single

TH-1099_04612102

and multilayer and all the characterization tools used in the present thesis. Chapter 3 is dedicated to the development of data analysis procedure for the determination of refractive index and thickness of practical thin films from transmittance and specular reflectance measurements. Chapter 4 deals with the determination of refractive index and thickness on PS prepared with systematic variation of B-doping concentration and etching current density through the procedure developed in Chapter 3. Chapter 5 presents the studies on photoluminescence of PS, which leads to the understanding of the origin of photoluminescence in PS and many other common observations in the photoluminescence of the material. Chapter 6 presents a systematic study on Raman scattering from differently prepared PS layers. Chapter 7 is dedicated to multilayer photonic structures of PS. Finally, Chapter 8 summarizes the results and presents the future scope of the work.

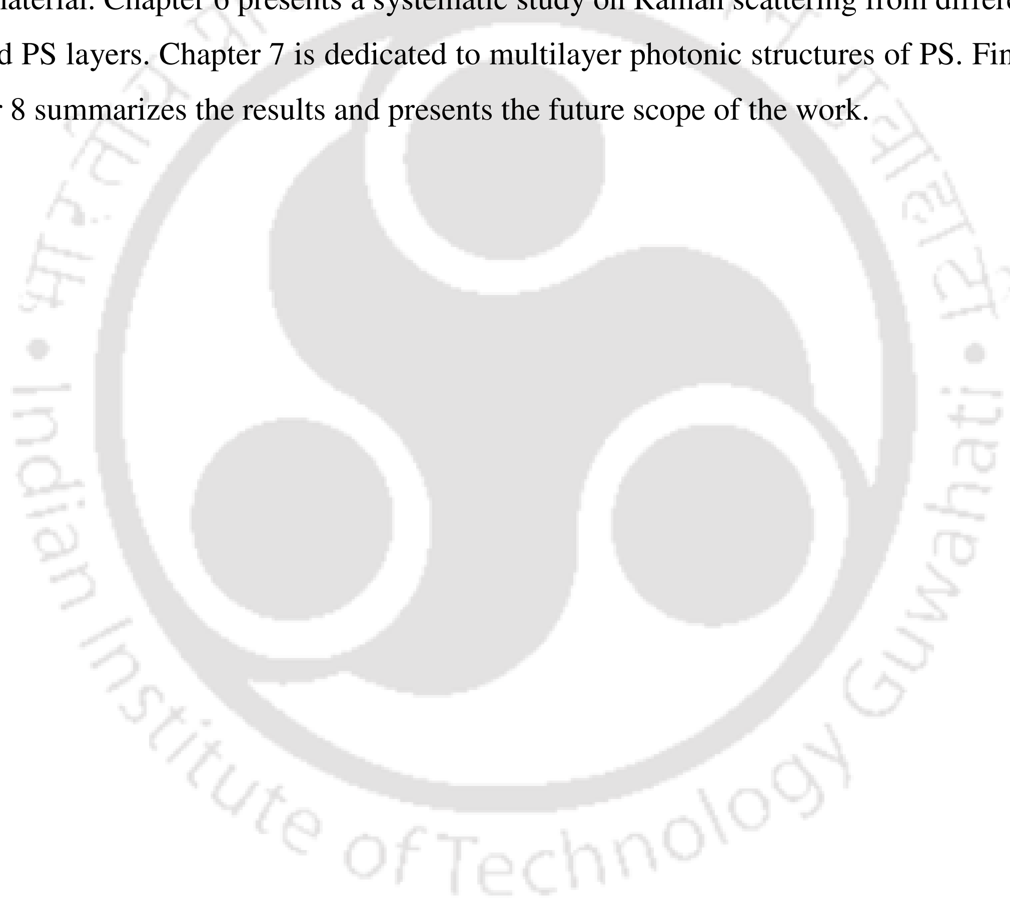

TH-1099_04612102

ABBREVIATIONS AND SYMBOLS

c-Si	Crystalline silicon
B-doping	Boron doping
DBM	Dielectric Bragg Mirror
EMT	Effective Medium Theory
FTIR	Fourier Transform Infrared Spectroscopy
HF	Hydrofluoric acid
PL	Photoluminescence
PLE	Photoluminescence Excitation
PS	Porous Silicon
QCM	Quantum Confinement Model
RS	Raman Scattering
SMC	Single Microcavity
T-matrix	Transfer matrix
UV-Vis-NIR	Ultraviolet visible near Infrared Spectroscopy

α_{ext}	Extinction coefficient
α_a	Absorption coefficient
α_s	Scattering coefficient
β	phase modulation in propagating electromagnetic wave in a medium
δ, γ	Refractive index dispersion between any two wavelengths
ζ	Fraction of the coherent radiation that would travel in the regular direction of propagation at an interface
θ	Angle of incidence of electromagnetic wave
λ	Wavelength or wavenumber
ρ	Resistivity
Ω	Interference fringe order for a particular fringe
ω	Angular frequency of the electromagnetic wave incident on the material

TH-1099_04612102

ω'	Angular frequency of the electromagnetic wave emitted from the material
c	Speed of light
d	Thickness of the film
d_{Op}	Optical thickness
E_F	Energy of electrons at the Fermi level
J	Anodization current density
K	Imaginary part of the refractive index of the substrate
k	Imaginary part of the refractive index of the film
m	Interference fringe order
n	Refractive index
n_{eff}	Effective refractive index
R	Specular reflectance
r_{ij}	Fresnel's reflectance coefficient at an interface separating the medium i and j
s	Real part of the refractive index of the substrate
T	Normal incidence transmittance
t_{ij}	Fresnel's transmittance coefficient at an interface separating the medium i and j

TH-1099_04612102

CONTENTS

Declaration i

Certificate ii

Acknowledgements iv

List of publications vi

Synopsis viii

Abbreviations and symbols xii

List of figures xix

List of tables xxviii

Chapter 1: Introduction 1

1.1 Literature perspectives of porous silicon 1

1.2 Motivations 3

1.2.1 Mechanism of photoluminescence 3

1.2.2 Shift of photoluminescence peak position with excitation energy 4

1.2.3 Determination of refractive index and thickness of composite films 4

1.2.4 Systematic studies on the variations of refractive index and growth rate with anodization conditions 5

1.2.5 Systematic study on Raman scattering with anodization conditions 6

1.2.6 Multilayer PS structures 6

1.3 Contents of the thesis chapters 6

TH-1099_04612102

1.4 References 7

Chapter 2: Porous silicon preparation and measurement details **13**

2.1 Preparation of porous silicon 13

2.2 Characterization measurement details 19

2.2.1 UV-Vis-NIR specular reflectance spectroscopy 19

2.2.2 Fourier transform infrared spectroscopy 21

2.2.3 Photoluminescence spectroscopy 21

2.2.4 Raman spectroscopy 22

2.3 References 22

Chapter 3: Theoretical formulation for the determination of refractive index and thickness **23**

3.1 Mathematical constructions of specular reflectance and transmittance for film-substrate system 23

3.1.1 Waves at rough interfaces 24

3.1.2 Waves in inhomogeneous medium 25

3.1.3 Mathematical expressions for specular reflectance and transmittance of film-substrate system 25

3.2 Interference conditions 30

3.3 Determination of interference fringe order, thickness and refractive index 30

3.3.1 Determination of interference fringe order, *m* 30

3.3.2 Determination of film thickness, *d* 32

3.3.3 Determination of the real part of the refractive index, *n* 35

TH-1099_04612102

3.4 Mathematical construction of specular reflectance of porous silicon system 35

3.4.1 Waves in PS media 36

3.4.2 Waves at PS interfaces 36

3.4.3 Mathematical expression for the specular reflectance of PS system 37

3.5 Numerical simulations 38

3.6 Summary 40

3.7 References 40

Chapter 4: Studies on growth rate and refractive index of porous silicon **41**

4.1 Determination of thickness and refractive index of PS 41

4.1.1 High B-doping concentration wafers 42

4.1.2 Low B-doping concentration wafers 50

4.2 Effects of anodization conditions on growth rate and effective refractive index of PS 62

4.2.1 Effects of anodization time on growth rate and effective refractive index of PS 62

4.2.2 Effects of anodization current density on growth rate and effective refractive index of PS 63

4.2.3 Effects of resistivity on growth rate and effective refractive index of PS 64

4.3 Summary 66

TH-1099_04612102

Chapter 5: Studies on photoluminescence in porous silicon 67

5.1 Experimental results on photoluminescence of PS ………….. 67

5.1.1 Photoluminescence spectra ………………………….. 68

5.1.2 Photoluminescence excitation spectra ……………….. 70

5.2 Theoretical simulation of optical absorption …………………. 72

5.3 Comparison of simulated optical absorption with PLE ……… 74

5.4 Structure of PS …………………………………………….. 75

5.5 Mechanism of PL in PS ……………………………………. 76

5.6 Understanding the experimental data ………………………. 79

5.6.1 Broad PL spectrum of PS …………………………….. 79

5.6.2 Excitation energy dependent peak position ………….. 79

5.6.3 Dissimilarities between PLE and absorption ………… 81

5.6.4 Luminescence enhancement with anodization current density ……………………………………………….. 83

5.7 Summary …………………………………………………….. 84

5.8 References …………………………………………………. 85

Chapter 6: Studies on Raman scattering in porous silicon 87

6.1 One-phonon Raman scattering in PS ………………………. 88

6.1.1 Low B-doping concentration wafers ………………… 90

6.1.2 High B-doping concentration wafers ………………… 94

6.1.3 One-phonon RS peak intensity with B-doping concentration ………………………………………… 97

6.2 Fano effect …………………………………………………. 98

TH-1099_04612102

6.2.1 Fano effect in RS of bulk c-Si ……………………….. 98

6.2.2 Fano effect in RS of PS ……………………………… 102

6.3 Summary ……………………………………………………... 106

6.4 References …………………………………………………… 106

Chapter 7: Porous silicon multilayer structures 109

7.1 Choice of wafer resistivity …………………………………… 110

7.2 Choice of refractive index and thickness …………………….. 111

7.3 PS multilayer structures ……………………………………… 113

7.3.1 Dielectric Bragg mirror ……………………………… 113

7.3.2 Single microcavity …………………………………… 116

7.4 Summary ……………………………………………………... 117

7.5 References …………………………………………………… 118

Chapter 8: Conclusions and future scopes 121

8.1 Thesis conclusions …………………………………………… 121

8.2 Future scopes ………………………………………………… 122

Appendix 123

TH-1099_04612102

List of Figures

1.1 Number of research publications per 5 year interval for the past 40 years. The data are obtained from SciFinder 2

2.1 Cross-section of electrolytic cell used for the preparation of PS. Different parts are not to the scale for the sake of visibility 14

2.2 Time evolution of pore formation at relatively low anodization current density. In the initial phase of the anodization, the dissolution of Si atoms creates depressions on the exposed Si surface. As the time elapses, the depressions would form as pores 15

3.1 A schematic of an inhomogeneous film with rough interfaces on a thick substrate 24

3.2 Simulations of normal incidence transmittance of homogeneous film with smooth interfaces (continuous line) and inhomogeneous film with rough interfaces (broken line) on transparent substrate through Eq. (3.5). Numerical values of optical and scattering parameters are from Section 3.5 (Numerical simulations) 27

3.3 Simulations of specular reflectance of homogeneous film with smooth interfaces (continuous line) and inhomogeneous film with rough interfaces (broken line) on transparent substrate through Eq. (3.8) at an incident angle of 20˚. Numerical values of optical and scattering parameters are from Section 3.5 (Numerical simulations) 29

3.4 Simulated spectra for the determination of d for the film on (a) transparent and (b) opaque substrate 32

3.5 Flow chart of the iterative procedure for the determination of film thickness *d* 34

3.6 A schematic of the cross-section of PS film on c-Si substrate 35

TH-1099_04612102

3.7 A closer view of the shift of the interference pattern with the change of angle of incidence in specular reflectance 38

4.1 Measured specular reflectance of PS prepared on 0.001–0.005 Ω cm c-Si wafer using (a) 25 mA/cm^2 current density for 60 sec (b) 50 mA/cm^2 current density for 45 sec and (c) 75 mA/cm^2 current density for 30 sec. The spectra are recorded at 8° angle of incidence 42

4.2 Measured specular reflectance of PS prepared on 0.01–0.05 Ω cm c-Si wafer using (a) 25 mA/cm^2 current density for 30 sec (b) 50 mA/cm^2 current density for 15 sec (c) 75 mA/cm^2 current density for 12 sec. The spectra are recorded at 45° angle of incidence 43

4.3 Theoretical fit to the interference pattern in the measured reflectance spectrum of PS prepared on 0.001–0.005 Ω cm resistivity c-Si wafer using 50 mA/cm^2 anodization current density for 45 sec. The theoretical fit is obtained through Eq. 3.6 using Bruggeman's EMT with porosity and thickness as the fitting parameters. The values of porosity and thickness used to fit the measured interference pattern are given at the inset. The interference orders that label the interference fringes have been determined through Eq. 3.7 44

4.4 Measured and theoretically fitted $d_{Op}(\lambda)$ of PS prepared on c-Si wafer of resistivity 0.001–0.005 Ω cm using 50 mA/cm^2 current density for 45 sec .. 45

4.5 Measured FTIR specular reflectance spectra of PS prepared on c-Si wafer of resistivity 0.001–0.005 Ω cm using 50 mA/cm^2 current density for 45 sec at 17.5° and 25° angles of incidence in the spectral range 5000–7000 cm^{-1}. The interference pattern shifts with the change of angle of incidence. The interference fringes are labelled with the interference fringe order …... 47

4.6 Measured and theoretically fitted dispersion of effective refractive index $n_{eff}(\lambda)$ of PS prepared on c-Si wafer of resistivity 0.001–0.005 Ω cm using 50 mA/cm^2 current density for 45 sec 48

4.7 Dispersion of effective refractive index $n_{eff}(\lambda)$ of PS prepared under various anodization current densities on c-Si wafers of resistivities (a) 0.001–0.005 Ω cm and (b) 0.01–0.05 Ω cm 49

TH-1099_04612102

4.8	Measured specular reflectance of PS prepared on 0.1–0.5 Ω cm c-Si wafer using (a) 25 mA/cm^2 current density for 2 min and (b) 75 mA/cm^2 current density for 45 sec ………………………………………………………...	50
4.9	Measured specular reflectance of PS prepared on c-Si wafers of resistivity 1–10 Ω cm using (d) 25 mA/cm^2 current density for 1.5 min (e) 50 mA/cm^2 current density for 45 sec (f) 75 mA/cm^2 anodization current density for 45 sec ………………………………………………………...	51
4.10	Measured specular reflectance of PS prepared on >50 Ω cm c-Si wafer using (a) 25 mA/cm^2 current density for 1.5 min (b) 50 mA/cm^2 current density for 45 sec (c) 75 mA/cm^2 current density for 30 sec ………………	52
4.11	Theoretical fit to the interference pattern in the measured reflectance spectrum of PS prepared on 0.1–0.5 Ω cm resistivity c-Si wafer using 25 mA/cm^2 current density for 2 min. The theoretical fit is obtained through Eq. 3.6 using Bruggeman's EMT with porosity and thickness as the fitting parameters. The values of porosity and thickness used to fit the measured interference pattern are given at the inset …………………………………..	53
4.12	A closer view of the extreme interference fringes towards optically thin region in the measured specular reflectance of PS prepared on c-Si wafer of resistivity 0.1-0.5 Ω cm under 25 mA/cm^2 current density for 2 min. The spectral positions are marked for the purpose of the determination of interference orders…………………………………………………………..	54
4.13	The interference fringe orders of the interference fringes in the measured specular reflectance of PS prepared on c-Si wafer of resistivity 0.1-0.5 Ω cm using 25 mA/cm^2 current density for 2 min. The interference orders are obtained from the conception that the interference orders of the neighbouring interference fringes differ only by 0.5………………………..	55
4.14	Dispersion of optical thickness $d_{Op}(\lambda)$ through the RHS of Eq. (3.7) with (a) one order lowered from the determined interference orders (b) no change in the determined interference orders and (c) one order raised from the determined interference orders …………………………......................	56

TH-1099_04612102

4.15 Experimentally determined and spline interpolated optical thickness dispersion $d_{Op}(\lambda)$ of PS prepared on c-Si wafer of resistivity 0.1–0.5 Ω cm using 25 mA/cm^2 current density for 2 min ………………………………. 57

4.16 Measured FTIR specular reflectance spectra of PS prepared on c-Si wafer of resistivity 0.1–0.5 Ω cm using 25 mA/cm^2 current density for 2 min at 17.5° and 25° angles of incidence in the spectral range 5400–7000 cm^{-1}. The interference pattern shifts with the change of angle of incidence. The interference fringes are labelled with the interference fringe orders determined through Method *II* of Chapter 3 ………………………………. 58

4.17 Experimentally determined and spline interpolated effective refractive index dispersion neff(λ) of PS prepared on c-Si wafer of resistivity 0.1–0.5 Ω cm using 25 mA/cm^2 current density for 2 min 59

4.18 Dispersion of effective refractive index $n_{eff}(\lambda)$ of PS prepared under various anodization current densities on c-Si wafer of resistivities (a) 0.1-0.5 Ω cm (b) 1-10 Ω cm and (c) > 50 Ω cm 60

4.19 Effect of anodization current density on (a) growth rate and (b) effective refractive index of PS prepared on various c-Si wafer resistivities……………………………………………………………….. 63

4.20 Effect of wafer resistivity on the growth of PS for various anodization current densities ………………………………………………………. 65

4.21 Effect of wafer resistivity on the effective refractive index n_{eff} of (a) aged and (b) as-prepared PS for various anodization current densities. n_{eff} of PS prepared on different resistive c-Si wafers are compared at 700 nm radiation ……………………………………………………………… 65

5.1 Measured PL spectra of aged PS prepared on c-Si wafers of resistivity 1–10 Ω cm under constant current anodization process using (a) 50 mA/cm^2 anodization current density for 15 min and (b) 80 mA/cm^2 anodization current density for 5 min …………………………………….. 68

5.2 Measured PL spectra of (a) as-prepared and (b) aged PS prepared under pulsed current (Freq = 20 Hz and Duty cycle = 40 %) anodization process on 1–10 Ω cm using 80 mA/cm^2 anodization current density for 5 min.

TH-1099_04612102

Also, the PL spectra of PS prepared under pulsed current (Freq = 10 Hz and Duty cycle = 60 %) anodization process using 25 mA/cm^2 anodization current density on c-Si wafers of resistivities (c) 1–10 Ω cm and (d) 5K–12K Ω cm for 45 and 160 sec, respectively ………………………………... 69

5.3 Measured PLE spectra of aged PS prepared on c-Si wafers of resistivity 1–10 Ω cm under constant current anodization process using (a) 50 mA/cm^2 anodization current density for 15 min and (b) 80 mA/cm^2 anodization current density for 5 min …………………………………… 70

5.4 Measured PLE spectra of (a) as-prepared and (b) aged PS prepared under pulsed current (Freq = 20 Hz and Duty cycle = 40 %) anodization process on 1–10 Ω cm using 80 mA/cm^2 anodization current density for 5 min. Also, the PLE spectra of PS prepared under pulsed current (Freq = 10 Hz and Duty cycle = 60 %) anodization process using 25 mA/cm^2 anodization current density on c-Si wafers of resistivities (c) 1–10Ωcm and (d) 5K–12K Ω cm for 45 and 160 sec, respectively ……………………………….. 71

5.5 Dispersions of (a) complex refractive index and (b) normal incidence reflectivity of bulk c-Si ……………………………………………………... 73

5.6 Theoretical simulations of normal incidence optical absorption of thin films with bulk c-Si optical constants for various thicknesses and zero reflectance condition through Eq. (5.2) …………………………………... 74

5.7 Measured normal incidence transmittance spectra of (a) c-Si of resistivity 1–10 Ω cm and (b) PS prepared by pulsed current electrochemical etching process on c-Si wafer of resistivity 1–10 Ω cm using 80 mA/cm^2 anodization current density for 5 min …………………………………….. 75

5.8 The effect of aging on the PL of PS recorded at (a) 3.81 eV and (b) 3.31eV excitations. The PS is prepared by pulsed current electrochemical process on c-Si wafer of resistivity 1–10 Ω cm using 80 mA/cm^2 anodization current density for 5 min …………………………….. 77

5.9 Measured normal incidence FTIR transmittance spectra of both as-prepared and stored in ambient conditions for 5 months prepared by pulsed current electrochemical etching of 1–10 Ω cm resistivity c-Si wafer with a current density of 80 mA/cm^2 for 5 min in the spectral range

TH-1099_04612102

(a) 500–1500 cm^{-1} and (b) 2000–2350 cm^{-1} ………………………………….. 78

5.10 Plot of energy difference between the excitation and PL peak position to the energy of excitation of aged PS ……………………………………... 80

5.11 (a) specular reflectance and (b) incoherent spectral scattering of PS prepared by pulsed current anodization on c-Si wafer of resistivity 0.001–0.005 Ω cm ………………………………………………………. 82

5.12 Measured PL of aged PS prepared by constant current anodization of c-Si wafers of resistivity 1–10 Ω cm using 50 and 80 mA/cm^2 anodization current densities ………………………………………………………… 83

6.1 Measured Raman scattering spectrum of a bulk c-Si of resistivity >50 Ω cm recorded under 632.8 nm laser excitation (a) the complete spectrum and (b) closer view of the multiphonon RS …………………… 88

6.2 A comparison of one-phonon RS spectral features of a nano-crystalline Si (top) with the bulk c-Si (bottom). The RS of nano-crystalline Si is simulated for 2.75 nm crystallite using the relation given in Ref [2]……… 89

6.3 A comparison of the spectral features of RS in high (top) and low (bottom) B-doped c-Si wafers. The spectra are recorded under 632.8 nm laser excitation ……………………………………………………………… 90

6.4 Measured one-phonon RS of both PS prepared using many different anodization current densities and the respective bulk c-Si wafer of resistivities 0.1–0.5 and 1–10 Ω cm with (a) and (c) vertically shifted and (b) and (d) no vertical shift. The spectra are recorded under 632.8 nm laser excitation, and are normalized to unity ……………………………………. 91

6.5 Measured one-phonon RS of both PS prepared using many different anodization current densities and the respective bulk c-Si wafer of resistivities >50 and 5K–12K Ω cm with (a) and (c) vertically shifted and (b) and (d) no vertical shift. The spectra are recorded under 632.8 nm laser excitation, and are normalized to unity 92

6.6 Variations of the peak intensity of one-phonon RS of PS with anodization current density for different wafer resistivities. The 0 mA/cm^2 corresponds to the respective bulk c-Si wafers ………………………………………….. 93

TH-1099_04612102

6.7 Measured one-phonon RS of both PS under many different anodization current densities and the respective bulk c-Si wafer of resistivities 0.001–0.005 Ω cm (a) vertically shifted and (b) no vertical shift and 0.01–0.05 Ω cm (c) vertically shifted and (d) no vertical shift. The spectra are recorded under 632.8 nm laser excitation, and are normalized to unity……………………………………………………………….. 95

6.8 Measured one-phonon RS of both PS under many different anodization current densities and the respective bulk c-Si wafer of resistivities 0.001–0.005 and 0.01–0.05 Ω cm with (a) and (c) vertically shifted and (b) and (d) no vertical shift. The spectra are recorded under 488 nm laser excitation, and are normalized to unity ……………………………………….. 96

6.9 The variation of peak intensity of one-phonon RS of (a) bulk c-Si and (b) PS prepared using 25, 50 and 75 mA/cm^2 anodization current densities with wafer resistivity. The RS for both bulk c-Si and PS are recorded under 632.8 nm laser excitation.…………………………………………………….... 97

6.10 A typical one-dimensional or isotropic band structure of a p-type semiconductor close to Brillouin zone centre. The Fermi energy EF is in the valance band. The incident photon of frequency ω excites an electron from the light-hole band to the conduction band. The excited electron into the conduction band de-excites to heavy-hole band by the emission of a scattered photon ω′. These intervanlance band electronic transitions give Raman spectrum with low and high frequency cut-offs denoted as Ω_m and Ω_M, respectively …………………………………………………….. 99

6.11 Measured RS of bulk c-Si wafers for several B-doping concentrations under the laser excitations 632.8 nm (a) closer view of the line-shape asymmetry of one-phonon RS and (b) closer view of the background inter-valance band electronic RS and the mulitphonon RS and 488 nm (c) closer view of the line-shape asymmetry of one-phonon RS and (b) closer view of the background inter-valance band electronic RS and the mulitphonon RS 100

6.12 Measured (discrete) and fit (continuous) of the Fano pattern of c-Si wafers of resistivities (a) 0.001–0.005 Ω cm and (b) 0.01–0.05 Ω cm for 488 nm (top) and 632.8 nm (bottom) laser excitations ……………………………. 101

TH-1099_04612102

6.13 Measured one-phonon RS of both PS under many different anodization current densities and the respective bulk c-Si wafer of resistivities (a) 0.001-0.005 Ω cm (b) 0.01-0.05 Ω cm (c) 0.1-0.5 Ω cm (d) 1-10 Ω cm and (e) >50 Ω cm. The spectra are recorded under 488 nm laser excitation, and are normalized to unity 103

6.14 Measured (discrete) and fit (continuous) of the line-shape asymmetry of RS of both PS and the respective bulk c-Si wafer of resistivity 0.01-0.05 Ω cm under the excitation wavelengths (a) 488 nm and (b) 632.8 nm. The line-shape asymmetry is fitted with the Fano function of Eq. (6.1) 104

7.1 Effect of anodization current density on (a) effective refractive index at 700 nm radiation and (b) growth rate of PS prepared on various c-Si wafer resistivities 111

7.2 Dispersions of effective refractive indices of PS prepared on c-Si wafers of resistivity 0.001–0.005 Ω cm under 5 (top) and 75 (bottom) mA/cm^2 anodization current density. The discrete data points (shown as ■) are experimental points and the continuous line is the fit through Bruggeman's EMT 112

7.3 A schematic of the cross section of a free standing DBM of 5 periods. A period consists of one n_H and n_L layers. n_H (n_L) and d_H (d_L) are the refractive index and thickness of high (low) refractive index layers, respectively where $d_H = \lambda_0/4n_H$ and $d_L = \lambda_0/4n_L$ and λ_0 is the centre of the reflectance band 113

7.4 Measured specular reflectance spectra (left) of PS DBMs are compared with the theoretical simulations (right) of identical structures. The theoretical simulations are performed using T-matrix method. The high refractive index layers are prepared with 5 mA/cm^2 anodization current density for 20 sec and the low refractive index layers are prepared with 75 mA/cm^2 anodization current density for 3 sec. The estimated thicknesses of high and low refractive index layers are 86 and 109 nm, respectively. The DBM structure can be given in short as $[HL]^5$ for (a) and

TH-1099_04612102

(b) and $[HL]^{15}$ for (c) and (d) where H and L denote high and low refractive index layers, respectively ……………………………………… 114

7.5 A schematic of the cross section of a free standing SMC with 2 periods before and after the cavity layer. n_H (n_L and n_C) and d_H (d_L and d_C) are the refractive index and thickness of high (low and cavity) refractive index layers, respectively where $d_H = \lambda_0/4n_H$, $d_L = \lambda_0/4n_L$ and $d_C = \lambda_0/2n_C$ and λ_0 is the centre of the reflectance band ……………………………………… 116

7.6 Measured specular reflectance spectra (left) of PS SMC is compared with the theoretical simulation (right) of identical structure through T-matrix method. PS SMC consists of 5 periods before and after the cavity layer. The high refractive index layers are prepared with 5 mA/cm^2 anodization current density for 20 sec and the low refractive index layers are prepared with 75 mA/cm^2 anodization current density for 3 sec. The estimated thicknesses of high and low refractive index layers are 86 and 109 nm, respectively. The cavity layer is prepared with 5 mA/cm^2 anodization current density for 40 sec. The SMC structure can be given in short as $[HL]^5HH[LH]^5$ where H and L denote high and low refractive index layers, respectively ………………………………………………………….............. 117

TH-1099_04612102

LIST OF TABLES

2.1 Details of anodization for the preparation of single layer PS ………….. 17

2.2 Details of anodization for the preparation of multilayer photonic structures on c-Si wafers of resistivity 0.001–0.005 Ω cm. High and low refractive index layers are denoted as H and L, respectively. By the end of every layer a stop for 3 sec is introduced for all structures. The superscripted Arabic numerals for the layer structures denote the number of times of repetition of the structure ………………………….. 19

3.1 Summary of the results of the iteration in the determination of *d* ……… 39

4.1 Summary of the results of the iteration in the determination of d for PS prepared on c-Si wafer of resistivity 0.001–0.005 Ω cm using 50 mA/cm^2 current density for 45 sec …………………………………… 47

4.2 Summary of thickness and growth rate of PS prepared on c-Si wafers of resistivities 0.001–0.005 and 0.01–0.05 Ω cm under various anodization current densities for various times …………………………………… 49

4.3 Summary of the results of the iteration in the determination of d for PS prepared on 0.1–0.5 Ω cm resistivity c-Si wafer using 25 mA/cm^2 current density for 2 min ………………………………………………... 58

4.4 Thickness and growth rate of PS prepared on c-Si wafers of resistivities 0.1–0.5, 1–10 and >50 Ω cm under various anodization current densities for various times ……………………………………………………… 61

4.5 Summary of growth rate and effective refractive index of PS prepared on c-Si wafers of resistivity 0.001-0.005 Ω cm using 25, 50 and 75 mA/cm^2 anodization current densities for various times ……………….. 62

5.1 The details of the anodization process, electrolyte concentration, wafer resistivity, anodization current density, anodization time and sample

TH-1099_04612102

conditioning of the representative PS 68

6.1 Values of q and Γ that fit the Fano line-shape of the measured RS of bulk c-Si wafer of resistivities 0.001–0.005 and 0.01–0.05 Ω cm for 488 and 632.8 nm excitations shown in Fig. 6.12 101

6.2 The best fit values of q and Γ for the asymmetric line-shape of PS prepared on c-Si wafers of resistivities 0.001–0.005, 0.01–0.05 and 0.1–0.5 Ω cm under 488 and 632.8 nm excitation wavelengths. The 0 mA/cm^2 anodization current density corresponds to the respective c-Si wafers 105

7.1 Details of anodization current density and time for the preparation of high and low refractive index layers, and their thicknesses and growth rates 112

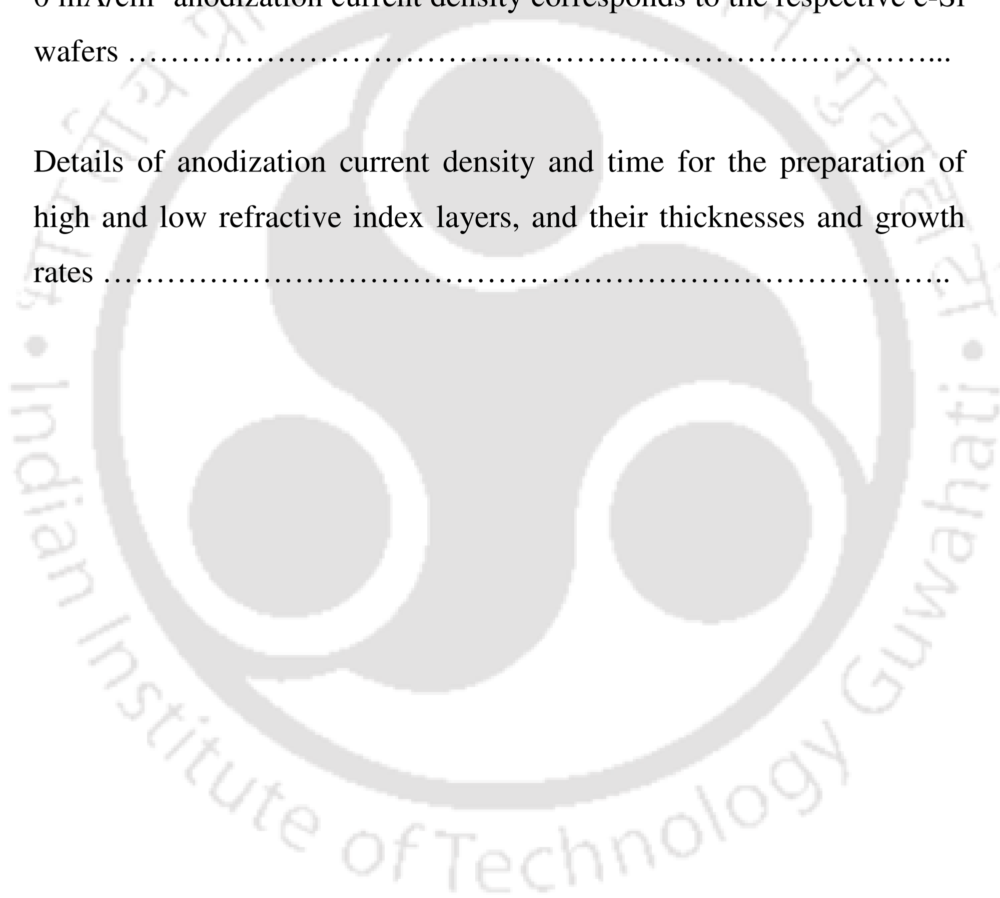

TH-1099_04612102

CHAPTER

1

INTRODUCTION

Understanding [1-3] of experimental observations and validation [4-8] of theoretical predictions have been the core of modern science development. Over the last century, with the advent of quantum mechanics, there have been renewed interests on the electrical, magnetic and optical properties of materials. Also, newer forms of the materials that have already been explored have come under close scrutiny [9-12]. One such material that has fascinated the material scientists by the end of the last century is porous Si (PS). This chapter presents the literature perspectives of PS, motivations behind the present work and the outline of the work contained in the present thesis.

1.1 LITERATURE PERSPECTIVES OF POROUS SILICON

Porous Si (PS) was discovered during electropolishing of Si in aqueous hydrofluoric acid in 1956 [13]. The material's dull and matte appearance had clearly distinguished it from the polished Si. By that time, as the interest was only to get a polished Si, this matte Si was considered to be an unwanted form of Si. A year after the first report on PS, similar films were prepared by stain-etching of Si in HF–HNO_3 solutions [14]. Only later, detailed studies on the structure, composition and growth rate of both anodic [15] and stain-etched

TH-1099_04612102

[16] Si films were reported. Even after these detailed studies, the films were not considered as porous, but as Si nanostructures. It actually took little more than a decade to recognize the porous nature of the material [17]. Soon then, the ease with which the material could be converted to Si oxide film was realized [18]. The conversion of PS to Si oxide film was to insulate the electronic circuits [19-21]. The interest on PS was not limited to insulating the electronic circuits only. The surface roughness, which was initially the cause of negligence of PS, later found to be useful to serve as a substrate material in heteroepitaxy [22]. These were the perspectives of PS until 1990.

In 1990, a discovery of a phenomenon in PS, the efficient visible photoluminescence (PL) at room temperature [23], had changed the whole perspectives of the material. This discovery had urged to consider once again the material as Si nanostructures [23-27]. But this time, the interest was more on the basic science aspect [28-30] rather than the technological applications [31, 32]. A plethora of research publications, far greater than the publications on the material until 1990, emerged after the discovery of the efficient PL as

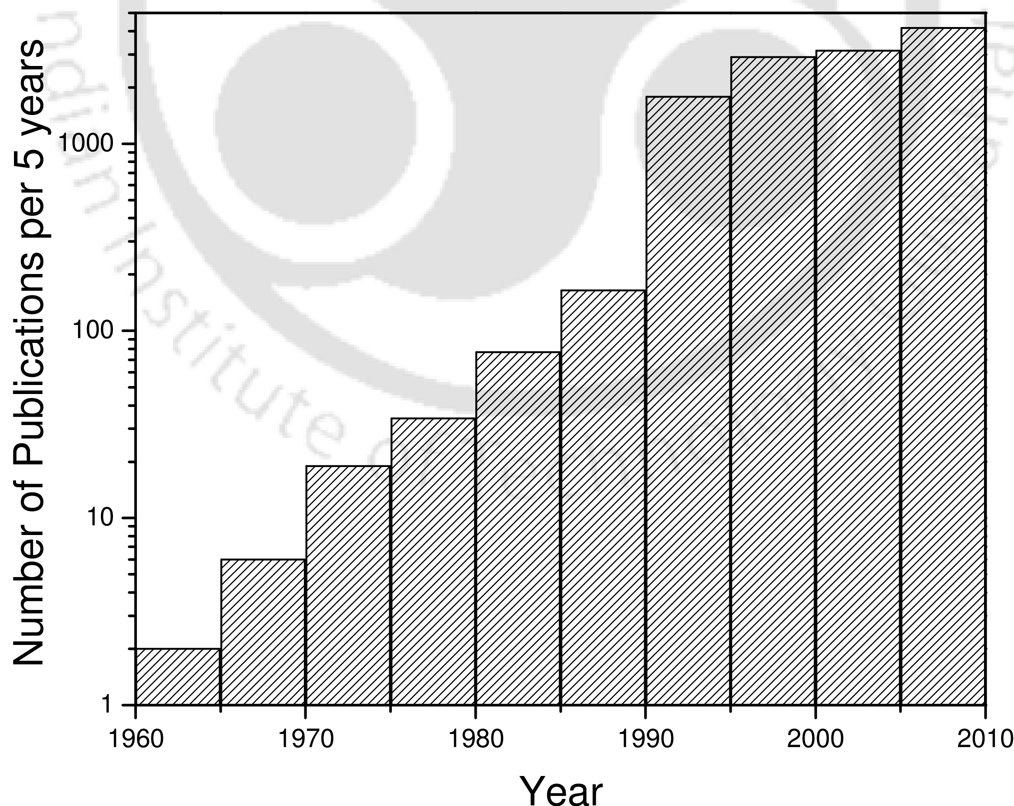

Figure 1.1 Number of research publications on porous Si per 5 year interval for the past 40 years. The data are obtained from SciFinder®.

TH-1099_04612102

can be seen in Fig. 1.1. The large number of research publications following the discovery of efficient PL was partly due to (i) the presence of Si, a well explored and technologically promising material both in crystalline and amorphous forms of matter, as a constituent (ii) ease and cost effective preparation technique (iii) the intriguing efficient visible photoluminescence and (iv) the growing interest on the low dimensional structures.

PS would be considered as a form of low dimensional Si structure only when interpreting the experimental observations like PL [33-36] and Raman scattering (RS) [37-41] spectrum. When dealing with the refractive index of the material, PS would be considered as a composite of Si particles and voids [42-45]. Effective medium theories (EMTs) have been used to determine the effective refractive index of PS [42-45]. In the literature, there even exists a detailed study on the choice of the EMT for the determination of the refractive index depending on the porosity of the material [45].

On a different perspective, it was identified that dielectric multilayer structures can be made with ease in PS [46]. Many complex PS multilayer structures had been realized during the years [47-55]. In fact, the optical analogue of electronic Bloch oscillations, optical Bloch oscillations, was even shown by a few research groups in specially designed PS multilayer structures [56, 57].

1.2 MOTIVATIONS

Following the discovery of efficient visible PL from PS in 1990, many excellent original works [33-36, 58-67] and review articles [28-30] have been published on the structural and optical properties of PS. However, there are certain issues on the PL of PS and some on the composite nature of the material itself remain yet unresolved. In this section, the motivations behind the thesis work are given in detail.

1.2.1 Mechanism of photoluminescence

Photoluminescence is although one of the key factors that have stimulated the research interest on PS, the mechanism of the phenomenon is yet a topic of intense debate. Canham, upon observation, was the first to suggest the quantum confinement model (QCM) to the efficient visible luminescence at room temperature [23]. Independently, Lehmann and Gösele ascribed the up-shift of the fundamental absorption edge of Si in PS to the effect of quantum confinement [68]. That was the very first convincing experimental evidence for

the QCM. Following that observation, many theoretical calculations [25-27] have been reported based on the QCM that could exactly retrace the experimental PL spectrum. However, many experimental observations in the PL of PS could not be explained by QCM. To mention a few, experimental observations such as temperature [69, 70] and pressure [71] dependence of PL peak energy, light-induced luminescence degradation [60] and results of heat and HF recycling [72] could not be explained on the lines of QCM. In fact, the temperature dependence of PL peak energy is claimed anomalous [69, 70] as the variation in PL peak energy deviate from that expected from quantum confinement concepts. Subsequently, many other models for the PL of PS have been proposed. The other proposed models suggest the visible luminescence is due to the presence of siloxene [73], hydride species [74], or hydrogenated amorphous Si [75, 76]. Of these models, the presence of siloxene has gained appreciation due the popularity of the visible luminescence in siloxene since 1922 [77]. Yet, the presence of siloxene and other forms of Si to the PL of PS is supported only by certain specific observations [76, 78]. This controversial scenario in the PL of PS has motivated to identify the origin of the phenomenon in PS.

1.2.2 Shift of photoluminescence peak position with excitation energy

There is an intriguing feature in the PL of PS – the PL peak position blue-shifts with the increase of excitation energy [58]. This feature has also been observed in the PL of siloxene. This feature being common to both PS and siloxene is also one of the reasons to ascribe PL in PS to the presence of siloxene [67]. However, the understanding of the peak shift itself is not clear in both siloxene and PS. So, the understanding of the blue-shift of the PL peak position with the increase of excitation energy has been another motive behind the thesis work.

1.2.3 Determination of refractive index and thickness of composite films

PS is a composite of Si particles and voids. Due to its composite nature, the material possesses refractive index of neither of its constituents. There exist EMTs for the determination of optical constants for composites [79-83]. The use of any EMT demands a prior knowledge of optical constants and occupied volume fractions of all the individual homogeneous components constituting the composite and their microscopic geometry. Depending on the microscopic geometry, there exist several EMTs, each specific to a

particular microscopic geometry. In reality, no composite would satisfy all the necessities for the applicability of the theory. In PS, the situation is even more complicated due to the presence of several adsorbed chemical species on the exposed Si surfaces. Practically, it is impossible to precisely identify all the chemical species, their optical constants and their occupied volume fractions in the material. These features make the determination of optical constants in PS films as a formidable task through EMTs.

The problem is not only in the theoretical determination of refractive index, but also in the experimental determination of the parameter. Composites being composed of several microscopic components are inherently inhomogeneous. Traditional determination procedures for refractive index and thickness are applicable only to homogeneous thin films [84-93] or films with weak inhomogeneity [94, 95], so that the incoherent scattering is not dominant in the magnitude of spectral transmittance or reflectance. A few proposals for the determination of refractive index and thickness of films with moderate inhomogeneity exist in the literature [43, 96-99]. However, those proposals are applicable only to specific cases due to certain limitations like requiring (i) optically thick films [98], (ii) additional measurements other than spectral transmittance and reflectance, which may sometimes be destructive [43], (iii) prior knowledge of dispersion of refractive index [99] and (iv) prior knowledge of incoherent spectral scattering due to inhomogeneity [99].

The non-existence of determination procedures for refractive index and thickness of inhomogeneous films, and PS system being one such case of the generality, has motivated to the theoretical formulation for the determination of refractive index and thickness of a general inhomogeneous thin film.

1.2.4 Systematic studies on the variations of refractive index and growth rate with anodization conditions

In spite of the close scrutiny on the optical properties of PS, systematic studies on the variations of refractive index and growth rate are still absent. By knowing the effects of anodization conditions on refractive index and growth rate, the understanding of the formation kinetics of PS would be improved. Also, the knowledge of refractive index and growth rate is necessary to optimize the anodization conditions to prepare PS multilayer structures with good optical response. These have motivated to study systematically the variations of refractive index and growth rate with anodization conditions.

1.2.5 Systematic study on Raman scattering with anodization conditions

Unlike with the phenomenon of PL from PS, there are no controversial issues with the interpretation of RS from PS in the literature. For nearly two decades, RS studies on PS have been supporting the existence of nanometre sized Si particles in PS. However, the finding of the present investigation on the PL is inconsistent with the plethora of literature on RS from PS. This inconsistency has motivated for a systematic study on the RS of PS with anodization conditions so that the finding of PL investigation could be verified and also the true nature of the structure of PS could be identified.

1.2.6 Multilayer PS structures

Generally, research on PS multilayer structures is with an application motive. Many complex PS multilayer structures have been prepared and shown to have properties like dielectric Bragg mirror, single microcavity, coupled microcavities, optical superlattices, etc. However, it has not been shown yet whether or not the single layer optical properties are affected with the preparation process of multilayer PS structures. A clear comparison of the optical response of multilayer PS structure with that of the expected response from the knowledge of single layer optical properties is missing. Such a comparison would not only show the effect of the preparation process on the structure, but also, whether or not the bulk and interfacial refractive indices are same for a composite. These have motivated to investigate multilayer PS structures.

1.3 CONTENTS OF THE THESIS CHAPTERS

Following this introductory chapter is Chapter 2, which gives a quick review on the formation of PS and details of the preparation procedures and conditions of both single and multilayer PS used in this thesis. The chapter also contains the details of the measurement tools used for the investigations of both single and multilayer PS films and the processing of as-measured data to remove any instrumental response embedded with the data.

Chapter 3 describes a general theoretical formulation for the determination of refractive index and thickness of thin films. The chapter gives the complete parametrical dependence for the magnitude of specular reflectance and transmittance for inhomogeneous thin films with rough interfaces on opaque and transparent substrates, respectively. The chapter also discusses the specular reflectance of PS on c-Si substrate.

TH-1090_04612102

After the descriptions on the determination of refractive index and thickness of thin films, Chapter 4 is the first results chapter of the thesis, which is on the determination of effective refractive index and growth rate of PS films prepared under many different anodization conditions. The determination of the parameters is made through the theoretical formulation described in Chapter 3. The variations of effective refractive index and growth rate with anodization conditions are explained on the basis of the effects of anodization conditions on the microstructure of PS.

Chapter 5 contains extensive studies on the PL of PS. A possible mechanism for the phenomenon, substantiated with the experimental observations, is given in the chapter. Also, the blue-shift of the PL peak position with the increase of excitation energy and a few other common observations in the PL of PS are explained in the chapter.

Chapter 6 presents a systematic study on the RS of PS prepared under the variations of anodization current density and B-doping concentration. The Fano effect, which is an interference phenomenon between the processes from discrete and continuum quantum eigenstates, is discussed in detail in the chapter on both bulk c-Si wafer and PS.

Chapter 7 is on the modulations of electromagnetic wave propagation in multilayer PS structures. The necessary factors that are to be considered in preparing multilayer PS structures are given in detail. Also, the chapter presents the comparison of optical responses of a few multilayer PS structures with theoretical simulations.

Chapter 8 is the final chapter of the thesis, which summarizes the contents of individual chapters and gives the final conclusion based on the work reported in this thesis. The chapter also lists the scope for future work from the present investigation.

1.4 REFERENCES

[1] M. Planck, Ann. Physik **4**, 553 (1901)

[2] A. Einstein, Ann. Physik **17**, 132 (1905)

[3] J. Bardeen, L. N. Cooper and J. R. Schrieffer, Phys. Rev. **106**, 162 (1957)

[4] A. A. Michelson and E. H. Morley, Am. J. Sci. **34**, 333 (1887)

[5] A. H. Compton, Phys. Rev. **21**, 483 (1923)

[5] C. J. Davisson and L. H. Germer, Phys. Rev. **30**, 705 (1927)

[6] G. P. Thomson, Proc. Roy. Soc (Lond.), Ser. A., **117**, 600 (1928)

[7] C. Jonsson, Z. Phys. **161**, 454 (1961)

[8] I. Estermann, R. Frisch, and O. Stern, Z. Phys. **73**, 348 (1931)

[9] P. Drude, Ann. Physik **36**, 532 (1889)

[10] S. Iijima and T. Ichihashi, Nature **363**, 603 (1993)

[11] A. K. Geim and K. S. Novoselov, Nat. Mater. **6**, 183 (2007)

[12] H. Fritzche, Annu. Rev. Mater. Sci. **2**, 697 (1972)

[13] A. Uhlir, Bell Syst. Tech. J. **35**, 333 (1956)

[14] C. S. Fuller and J. A. Ditzenberger, J. Appl. Phys. **27**, 544 (1957)

[15] D. R. Turner, J. Electrochem. Soc. **105**, 402 (1958)

[16] R. J. Archer, J. Phys. Chem. Solids **14**, 104 (1960)

[17] Y. Wantanabe and T. Sakai, Rev. Electron. Commun. Labs. **19**, 899 (1971)

[18] Y. Wantanabe, Y. Arita, T. Yokoyama, and Y. Igarashi, J. Electrochem. Soc. **122**, 1351 (1975)

[19] Y. Arita, K. Kato, and T. Sudo, IEEE Trans. Electron Devices **24**, 756 (1977)

[20] K. Imai and Y. Yoriume, Jpn. J. Appl. Phys. **16**, 1635 (1977)

[21] K. Imai, Solid-State Electron. **24**, 159 (1981)

[22] Y. C. Kao, B, J. Wu, K. L. Wang, C. W. Nieh, D. N. Jamieson, Y. J. Mii, T. L. Lin, and J. K. Liu, J. Vac. Sci. Technol. B **6**, 696, (1988)

[24] L. T. Canham, Appl. Phys. Lett. **57**, 1046 (1990)

[25] G. C. John, and V. A. Singh, Phys. Rev. B **50**, 5329 (1994)

[26] H. Yorikawa, and S. Muramatsu, Appl. Phys. Lett. **71**, 644 (1997)

[27] S. Chen, Y. Huang, and B. Cai, Solid-State Electron **49**, 940 (2005)

[28] A. G. Cullis, L. T. Canham, and P. D. J. Calcott, J. Appl. Phys. **82**, 909 (1997)

[29] D. J. Lockwood, Solid State Commun. **92**, 101 (1994)

[30] S. M. Prokes and O. J. Glembocki, Mater. Chem. Phys. **35**, 1 (1993)

[31] A. Richter, P. Steiner, F. Kozlowski, and W. Lang, IEEE Electron. Dev. Lett. **12**, 691 (1991)

[32] L. Pavesi, R. Guardini, and C. Mazzoleni, Solid State Commun. **97**, 1051 (1996)

[33] M. V. Wolkin, J. Jorne, P. M. Fauchet, G. Allan, and C. Delerue, Phys. Rev. Lett. **82**, 197 (1999)

[34] X. J. Li and Y. H. Zhang, Phys. Rev. B **61**, 12605 (2000)

[35] L. Wang, M. T. Wilson, and N. M. Haegel, Appl. Phys. Lett. **62**, 1113 (1993)

TH-1099_04612102

[36] M. Voos, P. Uzan, C. Delalande, G. Bastard, and A. Halimauli, Appl. Phys. Lett. **61**, 1213 (1992)

[37] H. Münder, C. Andrzejak, M. G. Berger, U. Klemradt, H. Lüth, R. Herino, and M. Ligeon, Thin Solid Films, **221**, 27 (1992)

[38] Md. N. Islam, R. N. Panda, A. Pradhan, and S. Kumar, Phys. Rev. B **65**, 033314 (2002)

[39] M. A. Ferrara, M. G. Donato, L. Sirleto, G. Messina, S. Santangelo, and I. Rendina, J. Raman Spectrosc. **39**, 199 (2008)

[40] H. Münder, C. Andrzejak, M. G. Berger, T. Eickhoff, H. Lüth, W. Theiss, U. Rossow, W. Richter, R. Herino, and M. Ligeon, Appl. Surf. Sci. **56-58**, 6 (1992)

[41] D. Abidi, B. Jusserand, and J. –L. Fave, Phys. Rev. B **82**, 075210 (2010)

[42] P. Petrik, M. Fried, É. Vázsonyi, T. Lohner, E. Horváth, O. Polgár, P. Basa, I. Bársony, and J. Gyulai, Appl. Surf. Sci. **253**, 200 (2006)

[43] A. Wolf, B. Terheiden, and R. Brendel, J. Appl. Phys. **104**, 033106 (2008)

[44] W. Theiβ, S. Henkel, and M. Arntzen, Thin Solid Films **255**, 177 (1995)

[45] W. Theiβ, Surf. Sci. Rep. **29**, 91 (1997)

[46] M. G. Berger, C. Dieker, M. Thönissen, L. Vescan, H. Lüth, H. Münder, W. Theiβ, M. Wernke, and P. Grosse, J. Phys. D: Appl. Phys. **27**, 1333 (1994)

[47] L. Pavesi and V. Mulloni, J. Lumin. **80**, 43 (1999)

[48] J. O. Estevez, J. Arriaga, A. M. Blas, and V. Agarwal, Appl. Phys. Lett. **93**, 191915 (2008)

[49] E. Lorenzo, C. J. Oton, N. E. Capuj, M. Ghulinyan, D. N. –Urrios, Z. Gaburro, L. Pavesi, Appl. Opt. **44**, 5415 (2005)

[50] M.S. Salem, M. J. Sailor, T. Sakka, Y. H. Ogata, J. Appl. Phys. **101**, 063503 (2007)

[51] N. Ishikura, M. Fujii, K. Nishida, S. Hayashi, J. Diener, Opt. Express **16**, 15531 (2008)

[52] L. Moretti, I. Rea, L. Rotiroti, I. Rendina, G. Abbate, A. Marino, L. D. Stefano, Opt. Express **14**, 6264 (2006)

[53] M. B. H. Breese and D. Mangaiyarkarasi, Opt. Express **15**, 5537 (2007)

[54] L. Pavesi, G. Panzarini, and L. C. Andreani, Phys. Rev. B **58**, 15794 (1998)

[55] M. Ghulinyan, C. J. Oton, L. D. Negro, L. Pavesi, R. Sapienza, M. Colocci, D. S. Wiersma, Phys. Rev. B **71**, 094204 (2005)

[56] R. Sapienza, P. Costantino, D. Wiersma, M. Ghulinyan, C. J. Oton, L. Pavesi, Phys. Rev. Lett. **91**, 263902 (2003)

[57] V. Agarwal, J. A. D. Río, G. Malpuech, M. Zamfirescu, A. Kavokin, D. Coquillat, D. Scalbert, M. Vladimirova, and B. Gil, Phys. Rev. Lett. **92**, 097401 (2004)

[58] O. K. Andersen, and E. Veje, Phys. Rev. B **53**, 15643 (1996)

[59] G. G. Qin, H. Z. Song, B. R. Zhang, J. Lin, J. Q. Duan, and G. Q. Yao, Phys. Rev. B **54**, 2548 (1996)

[60] I. M. Chang, S. C. Pan, and Y. F. Chen, Phys. Rev. B **48**, 8747 (1993)

[61] S. Sawada, N. Hamada, and N. Ookubo, Phys. Rev. B **49**, 5236 (1994)

[62] J. L. Gole, F. P. Dudel, D. Grantier, and D. A. Dixon, Phys. Rev. B **56**, 2137 (1997)

[63] Y. Kanemitsu and S. Okamoto, Phys. Rev. B **58**, 9652 (1998)

[64] H. D. Fuchs, M. Stutzmann, M. S. Brandt, M. Rosenbauer, J. Weber, A. Breitschwerdt, P. Deák, and M. Cardona, Phys. Rev. B **48**, 8172 (1993)

[65] T. George, M. S. Anderson, W. T. Pike, T. L. Lin, R. W. Fathauer, K. H. Jung, and D. L. Kwong, Appl. Phys. Lett. **60**, 2359 (1992)

[66] S. –F. Chuang, S. D. Collins, and R. L. Smith, Appl. Phys. Lett. **55**, 1540 (1989)

[67] M. S. Brandt, H. D. Fuchs, M. Stutzmann, J. Weber, and M. Cardona, Solid State Commun. **81**, 307 (1992)

[68] V. Lehmann, and U. Gösele, Appl. Phys. Lett. **58**, 856 (1991)

[69] X. L. Zheng, W. Wang, and H. C. Cheng, Appl. Phys. Lett. **60**, 986 (1992)

[70] Z. Y. Xu, M. Gal, and M. Gross, Appl. Phys. Lett. **60**, 1375 (1992)

[71] W. Zhou, H. Shen, J. F. Harvey, R. A. Lux, M. Dutta, F. Lu, C. H. Perry, R. Tsu, N. M. Kalkhoran, and F. Namavar, Appl. Phys. Lett. **61**, 1435 (1992)

[72] S. M. Prokes, W. E. Carlos, and V. M. Bermudez, Appl. Phys. Lett. **61**, 1447 (1992)

[73] R. T. Collins, M. A. Tischler, and J. H. Stathis, Appl. Phys. Lett. **61**, 1649 (1992)

[74] S. M. Prokes, O. J. Glembocki, V. M. Bermudez, R. Kaplan, L. E. Friedersdorf, and P.C. Searson, Phys. Rev. B **45**, 13788 (1992)

[75] R. P. Vasquez, R. W. Fathauer, T. George, A. Ksendzov, and T. L. Lin, Appl. Phys. Lett. **60**, 1004 (1992)

[76] J. M. Perez, J. Villalobos, P. McNeill, J. Prasad, R. Cheek, J. Kelber, J. P. Estrera, P. D. Stevens, and R. Glosser, Appl. Phys. Lett. **61**, 563 (1992)

[77] H. Kautsky, and H. Zocher, Z. Phys. **9**, 267 (1922)

TH-1090_04612102

[78] P. Deák, M. Rosenbauer, M. Stutzmann, J. Weber, and M. S. Brandt, Phys. Rev. Lett. **69**, 2531 (1992)

[79] D. A. G. Bruggeman, Ann. Phys. **24**, 636 (1935)

[80] H. Looyenga, Physica (Amsterdam) **31**, 401 (1965)

[81] J. C. M. Garnett, Philos. Trans. R. Soc. London, Ser. A **203**, 385 (1904)

[82] D. J. Bergman, Physics Reports **43**, 377 (1978)

[83] R. J. Gehr and R. W. Boyd, Chem. Mater. **8**, 1807 (1996)

[84] J. F. Hall, Jr. and W. F. C. Ferguson, J. Opt. Soc. Am. **45**, 714 (1955)

[85] P. R. Wessel, Phys. Rev. **153**, 836 (1967)

[86] G. D. Cody, C. R. Wronski, B. Abeles, R. B. Stephens and B. Brooks, Solar Cells **2**, 227 (1980)

[87] J. C. Manifacier, J. Gasiot and J. P. Fillard, J. Phys. E: Sci. Instrum. **9**, 1002 (1976)

[88] R. Swanepoel, J. Phys. E: Sci. Instrum. **16**, 1214 (1983)

[89] D. B. Kushev, N. N. Zheleva, Y. Demakopoulou and D. Siapkas, Infrared Phys. **26**, 385 (1986)

[90] D. A. Minkov, J. Phys. D: Appl. Phys. **22**, 199 (1989)

[91] D. P. Arndt, R. M. A. Azzam, J. M. Bennett, J. P. Borgogno, C. K. Carniglia, W. E. Case, J. A. Dobrowolski, U. J. Gibson, T. T. Hart, F. C. Ho, V. A. Hodgkin, W. P. Klapp, H. A. Macleod, E. Pelletier, M. K. Purvis, D. M. Quinn, D. H. Strome, R. Swenson, P. A. Temple and T. F. Thonn, Appl. Opt. **23**, 3571 (1984)

[92] Rusli and G. A. J. Amaratunga, Appl. Opt. **34**, 7914 (1995)

[93] S. D. Ventura, E. G. Birgin, J. M. Martínez and I. Chambouleyron, J. Appl. Phys. **97**, 043512 (2005)

[94] B. Bovard, F. J. V. Milligen, M. J. Messerly, S. G. Saxe and H. A. Macleod, Appl. Opt. **24**, 1803 (1985)

[95] L. De Caro and M. C. Ferrara, Thin Solid Films **342**, 153 (1999)

[96] M. Nowak, Thin Solid Films **254**, 200 (1995)

[97] J. C. Martínez-Antón, Appl. Opt. **39**, 4557 (2000)

[98] J. C. Martínez-Antón and E. Bernabeu, Optics Comm. **132**, 321 (1996)

[99] M. Montecchi, R. M. Montereali and E. Nichelatti, Thin Solid Films **396**, 262 (2001)

TH-1099_04612102

CHAPTER

2

POROUS SILICON PREPARATION AND MEASUREMENT DETAILS

In this chapter, the preparation of porous Si (PS) (both single and multilayer) films and the various characterization tools used to study PS would be discussed in detail. The purpose of this chapter is to elucidate the utile details obtained through different experimental techniques and to ensure the comparability of results with the already existing reports in literature.

2.1 PREPARATION OF POROUS SILICON

One of the reasons for the popularity of porous Si (PS) among the scientific community is the ease and cost effective preparation technique. Traditional route to the preparation of porous Si is the electrochemical etching of Si in aqueous hydrofluoric acid [1-3]. A schematic of the set-up used for the preparation of PS is shown in Fig. 2.1. Electrolyte, the mixture of HF (48% aqueous) and ethanol with 2:3 by volume, is taken in a vertical Teflon electrochemical cell. Monocrystalline Si (c-Si) (1.2 cm diameter), with the mirror-polished face exposed to the electrolyte, acts as an anode and a platinum ring (2.9 cm diameter), at a distance of 1 cm from the anode, acts as a cathode. Prior to use the c-Si wafer as the anode, a thick layer of Al is deposited on the textured back surface of the wafer, and annealed for

TH-1099_04612102

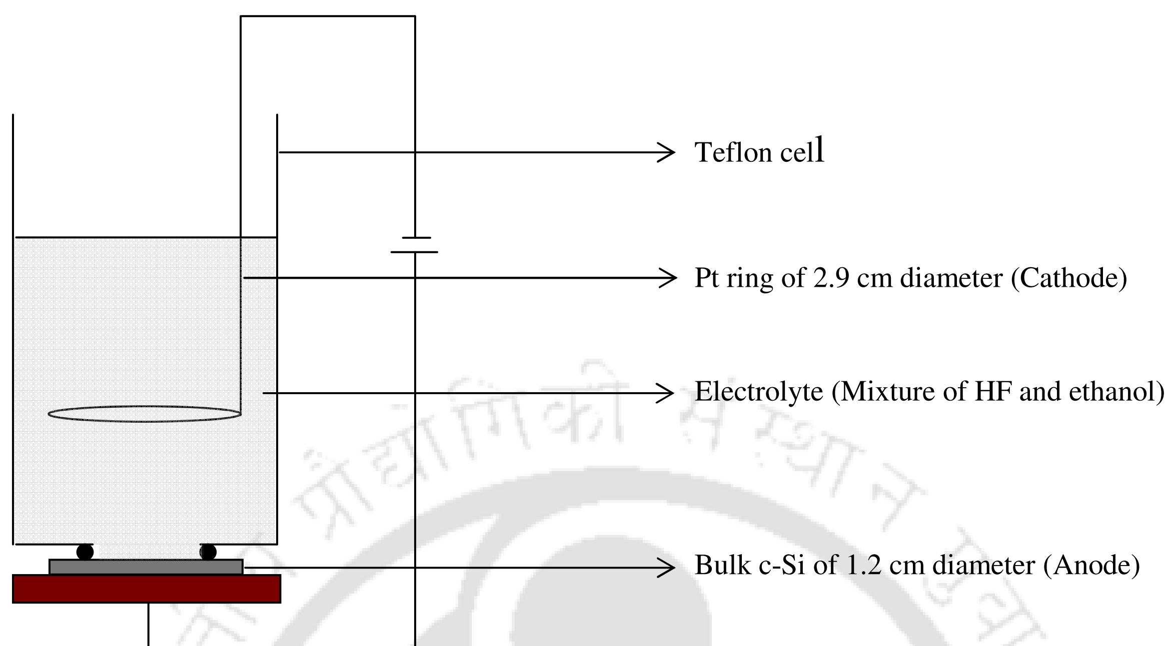

Figure 2.1 Cross-section of electrolytic cell used for the preparation of PS. Different parts are not to the scale for the sake of visibility.

5 minutes at 525 ˚C under vacuum (~6 x 10^{-6} mbar). This processing of c-Si wafer, prior to use it as the anode, is necessary for a good ohmic contact with the rest of the circuit and also for the uniform distribution of electric field throughout the exposed Si surface. In the electrochemical process, the c-Si wafer, which is the anode, is being etched. So, henceforth in the thesis, the electrochemical process is addressed as *anodization*.

The anodization of c-Si wafer is due to the presence of holes and F^- ions in the electrochemical system [4], which are sourced by the c-Si wafer and electrolyte, respectively. The time evolution of pore formation during the anodization process is illustrated in Fig. 2.2. Before the anodization current density is set, the holes and F^- ions accumulate at the solid/liquid interface depending on their concentrations in the respective media. At a relatively low anodization current density to the system, due to inherent inhomogeneity in the carriers' concentrations, the dissolution of Si atoms is effective on the regions where the carriers' concentrations are more and are readily available for dissolution [5]. This results in the formation of depressions on the exposed Si surface. As the time elapses, more carriers get closer to those depressions and the dissolution proceeds in depth. This results in pore formation. The pores as formed permeate through

TH-1099_04612102

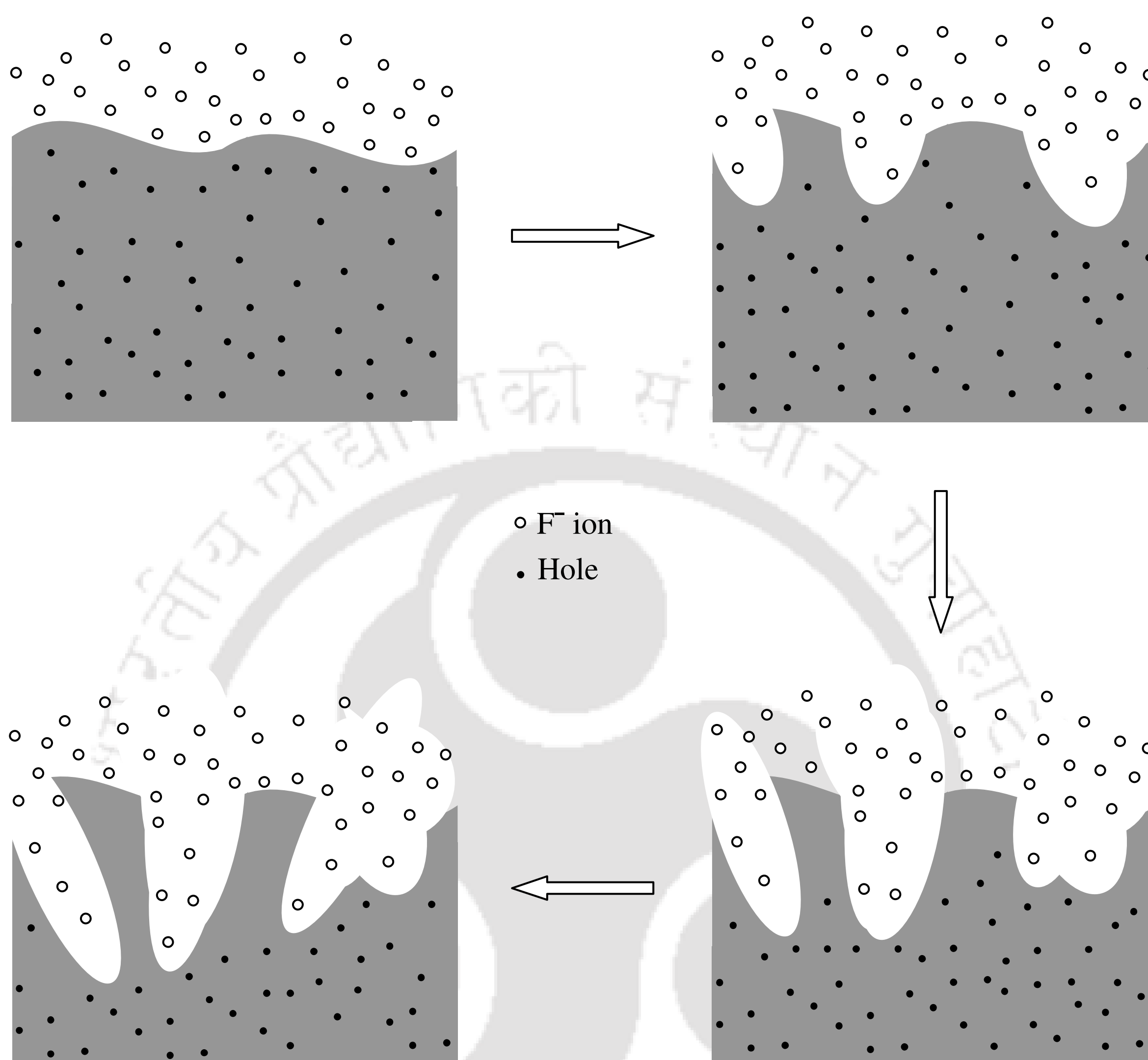

Figure 2.2 Time evolution of pore formation at relatively low anodization current density. In the initial phase of the anodization, the dissolution of Si atoms creates depressions on the exposed Si surface. As the time elapses, the depressions would form as pores.

c-Si wafer and form a labyrinthine network of pores. On the other hand, at relatively high anodization current densities, the dissolution of Si atoms is more uniform over the exposed Si surface, where the Si atoms are evenly removed layer after layer, thereby resulting in *electropolishing*.

For the dissolution to be uniform, (whereby it is meant that the pore geometry and the porosity are same throughout the PS layer), there must be a constant supply of free holes and F^- ions to the solid/liquid interface during the course of anodization. However, the

transport of holes and F^- ions is affected as the time elapses. In the initial phase of the dissolution process, the transport of holes and F^- ions to the solid/liquid interface is affected by the electrical resistances of c-Si wafer and electrolyte, respectively. As the dissolution proceeds, the etching of Si atoms is predominant on the freshly exposed Si surfaces at the pore depths. So, the transport of holes, as they reach the solid-liquid interface through the bulk of the c-Si, is seldom affected by the labyrinthine network of pores. However, the F^- ions travel through the pores and reach the pore depths to meet the holes in freshly exposed Si surfaces. So, the transport of F^- ions, in addition to the resistance offered by the electrolyte, is also affected by the pore geometry. On a certain pore geometry, where the transport of the ions is seriously affected, the concentration of F^- ions at the pore depths decreases as the time elapses. This condition would affect both the pore geometry and the porosity of the material in depth. To compensate the slow movement of the ions, a stop is introduced, in an otherwise constant current anodization. The concentration of F^- ions in the electrolyte at the pore depths regenerates during the period of stop. When the introduced stop is periodic in the anodization current density, the electrochemical process is said to be *pulsed current electrochemical process*.

PS prepared by pulsed current electrochemical process has a better uniformity in depth. The PS layers reported in this thesis are mostly prepared by pulsed current electrochemical process at a frequency of 10 Hz and 60% duty cycle. To further improve the uniformity in depth, additional periodic intermittence of 3 sec is introduced. The frequency of stop for the additional intermittence has an increasing trend with current density. The etching time specified in the later part of this report is actually the total duration of the active cycle in the pulsed electrochemical process. The preparation details of single layer PS considered for various investigations in this thesis are given in Table 2.1. Three PS listed at the end of the Table 2.1, which are prepared under slightly different conditions from the rest of the PS, are mainly used for the investigation of photoluminescence of PS. Table 2.2 gives the details of preparation of multilayer PS. The PS layers thus obtained are rinsed with deionised water, instantly, and are then dried in ambient.

The etching processes for the preparation of both single and multilayer PS are carried out by a computer controlled constant current source (HIOKI 7020). The interfacing of constant current source with the computer is made through our own customised LabVIEW programs.

TH-1099_04612102

Table 2.1 Details of anodization for the preparation of single layer PS.

Resistivity (Ω cm)	Electrolyte HF : Ethanol	Anodization current density (mA/cm^2)	Anodization time (min)	Elapse between successive stops (sec)	Pulse
5K–12 K	2 : 3	25	2.00	10	
		50	1.00	06	
		75	0.50	04	
>50	2 : 3	25	1.50	10	
		50	0.75	06	
		75	0.50	04	
1–10	2 : 3	05	2.00	10	
		25	1.50	10	
			1.00		
			0.75		
		50	1.00	06	
			0.75		Freq = 10 Hz and 60 % duty cycle
			0.50		
		75	0.75	04	
			0.50		
			0.25		
		100	0.10	03	
		150	0.10	02	
0.1–0.6	2 : 3	05	2.00	10	
		25	2.00	10	
			1.50		
			1.00		
		50	1.00	06	
			0.50		
			0.75		

Resistivity (Ω cm)	Electrolyte HF : Ethanol	Anodization current density (mA/cm^2)	Anodization time (min)	Elapse between successive stops (sec)	Pulse
0.1–0.6	2 : 3	75	0.75	04	Freq = 10 Hz and 60 % duty cycle
			0.50		
			0.25		
		100	0.25	03	
		150	0.20	02	
0.01–0.05	2 : 3	25	0.50	10	
		50	0.25	06	
		75	0.20	04	
0.001–0.005	2 : 3	01	4.00	10	
		05	3.00		
		25	2.00	10	
			1.50		
			1.00		
		50	1.50	06	
			1.00		
			0.75		
		75	1.00	04	
			0.75		
			0.50		
		100	0.75	03	
		150	0.50	02	
1–10	1 : 1	80	5.00	---	Freq = 20 Hz and 40 % duty cycle
		50	15.00		---
		80	5.00		

Indian Institute of Technology Guwahati

Table 2.2 Details of anodization for the preparation of multilayer photonic structures on c-Si wafers of resistivity 0.001–0.005 Ω cm. High and low refractive index layers are denoted as H and L, respectively. By the end of every layer a stop for 3 sec is introduced for all structures. The superscripted Arabic numerals for the layer structures denote the number of times of repetition of the structure.

Photonic crystal	Layer structure	H layer		L layer	
		Current density (mA/cm^2)	Anodization time (sec)	Current density (mA/cm^2)	Anodization time (sec)
Bragg mirror	$[HL]^5$	5	20	75	3
	$[HL]^{15}$				
Microcavity	$[HL]^5HH[LH]^5$	5	20	75	3

2.2 CHARACTERIZATION MEASUREMENT DETAILS

The characterization tools used for the investigation of various optical processes in PS are mainly spectroscopic tools like UV-Vis-NIR spectroscopy, Fourier transform infrared spectroscopy, Raman spectroscopy, photoluminescence spectroscopy and photoluminescence excitation spectroscopy. The PS layers reported in this thesis are thin layers of thicknesses ranging from a few hundred nanometres to a few micrometers, and are supported by the bulk c-Si wafers from which the PS layers are made. All the measurements are preformed on commercial instruments with the PS facing the incoming radiation, and sampled near around the same region of the film.

2.2.1 UV-Vis-NIR Specular Reflectance Spectroscopy

Bulk c-Si, on the rear side of the PS, strongly absorbs the electromagnetic radiation near around the visible region of the spectrum. So, UV-Vis-NIR spectroscopy is preformed in reflectance geometry rather than transmittance geometry. Reflectance spectroscopy is broadly categorized as specular and diffused reflectance spectroscopies. In the present thesis, UV-Vis-NIR spectroscopy is performed only in specular reflectance mode.

Specular reflectance spectra of PS prepared under different anodization conditions are recorded on two commercial dual beam spectrometers – PerkinElmer and Varian Cary 50.

PS prepared from c-Si wafers of resistivity 0.001–0.005, 0.1–0.6 and 1–10 Ω cm are recorded on PekinElmer at 8° angle of incidence in the spectral range from 300 to 880 nm. The as-recorded spectra, in PerkinElmer, are relative to an internal mirror. Varian Cary 50 is used to record the spectra on PS prepared from c-Si wafers of resistivity 0.01–0.05 and >50 Ω cm at 45° angle of incidence in the spectral range from 300 to 1100 nm. The multilayer PS structures are also characterized with Cary 50 at 45° angle of incidence. The as-recorded spectra, in Varian Cary 50, are relative to a reference mirror provided by the manufacturer.

With commercial dual beam spectrometers, the measurement of absolute transmittance of a material is a simple and routine task. However, with the majority of the spectrometers, the measurement of absolute reflectance is not so. The as-measured reflectance spectrum is with respect to a reference mirror either internal (as in the case of PerkinElmer) or external (as in the case of Varian Cary 50) and can mathematically be represented as

$$R^{sam}_{meas}(\omega) = R^{sam}_{abs}(\omega) / R_{ref}(\omega) \qquad (2.1)$$

where R^{sam}_{meas} is the as-measured reflectance, R^{sam}_{abs} is the absolute reflectance of the material, R_{ref} is the absolute reflectance of the reference (mirror) and ω is the frequency of radiation.

At this stage of measurement, the only known parameter is R^{sam}_{meas}. The parameters R^{sam}_{abs} and R_{ref} are unknowns. To obtain R^{sam}_{abs}, R_{ref} has to be identified. This can be done by repeating the measurement on a material whose reflectance is already known, which is considered as the standard. The information obtained by doing so can mathematically be represented as

$$R^{std}_{meas}(\omega) = R^{std}_{abs}(\omega) / R_{ref}(\omega) \qquad (2.2)$$

where R^{std}_{meas} is the as-measured reflectance of the standard and R^{std}_{abs} is the absolute reflectance of the standard. Equation (2.2) has been rearranged to obtain R_{ref}, which is the only unknown in the equation, and also a necessary parameter to obtain the absolute reflectance of the material.

In the present thesis, the material chosen as the standard to obtain the R_{ref} is the mirror-polished face of c-Si wafer. The as-measured reflectance spectra of the PS films are then corrected for any spectral dependence of the reference mirror. The UV-Vis-NIR specular reflectance spectra of PS layers presented in the later chapters of this thesis are all

TH-1090_04612102

corrected for the spectral dependence of the reference mirror.

2.2.2 Fourier Transform Infrared Spectroscopy

PerkinElmer Spectrum BX, a single beam infrared spectrometer working on the principle of Fourier transform, is used for infrared studies. The spectrometer is operated with a resolution of 4 cm^{-1} on both transmittance and reflectance geometry. In transmittance geometry, the infrared radiation falls on the PS sample at normal incidence. The spectra collected in the transmittance geometry are used to identify the chemical species in PS matrix.

In reflectance geometry, the infrared radiation falls on the sample at an oblique incidence. The spectra, in the reflectance geometry, are collected at 17.5° and 25° angles of incidence from the surface normal. As discussed in UV-Vis-NIR specular reflectance spectroscopy, here too the as-measured reflectance spectra are relative to a reference mirror. The spectra are then corrected for any spectral dependence of the reference mirror. The FTIR specular reflectance spectra of PS layers presented in the later chapters of this thesis are all corrected for the spectral dependence of the reference mirror. The specular reflectance spectra of PS collected at two different angles of incidence are used to determine the thickness of the PS layers.

2.2.3 Photoluminescence Spectroscopy

Photoluminescence (PL) is an optical process whereby low energetic photons are emitted by the sample when excited with high energetic photons. AMINCO-Bowman Series 2 Luminescence spectrometer is used for the study of PL of PS. A 150 W Xenon arc lamp followed by a monochromator is the excitation source for the spectrometer. Both PL and photoluminescence excitation (PLE) spectra are recorded on the same spectrometer without disturbing the sample position. In the present thesis, the PL spectra are recorded at fixed excitation energy with the scan for the emission energies, whereas, the PLE spectra are recorded at fixed emission energy with the scan for the excitation energies. During the scans, the sample is oriented in such a way that the excitation radiation does not get through the emission slit. Besides, an optical filter, which blocks any radiation below 450 nm, is used at the entrance of the emission slit to suppress the higher orders of the excitation radiations. All PL and PLE spectra are corrected for the relative excitation photon flux and the transmission of the optical filter.

2.2.4 Raman Scattering Spectroscopy

Raman scattering is inelastic scattering of photons by the fluctuations such as atomic vibrations, charge density, spin density and so on in the material. Horiba JY Labram HR800 micro-Raman system is used to study Raman scattering in backscattering geometry. Of the inelastically scattered photons only Stoke shifted photons, which are lower in energy than the incident photons, are recorded. The resolution and the recorded spectral range of Raman shifts are 1 and 50–1200 cm^{-1}, respectively. The monochromatic laser excitation wavelengths used to record Raman shifts are 488 and 632.8 nm. The Raman shifts reported in this thesis are relative to the corresponding monochromatic laser excitation wavelengths. While recording the Raman shifts, the excitation laser radiations are tightly focussed on the surface of the sample to a spot size of <5 μm. As the micro-Raman system employs confocal optics to collect the Raman scattered photons from the sample, the recorded Raman shifts are basically dominated by the region covered by the plane of focus of the laser beam.

2.3 REFERENCE

[1] A. Uhlir, Bell Syst. Tech. J. **35**, 333 (1956)

[2] L. T. Canham, Appl. Phys. Lett. **57**, 1046 (1990)

[3] R. L. Smith and S. D. Collins, J. Appl. Phys. **71**, R1 (1992)

[4] V. Lehmann, and U. Gösele, Appl. Phys. Lett. **58**, 856 (1991)

[5] W. Theiβ, Surf. Sci. Rep. **29**, 91 (1997)

TH-1092_04612102

CHAPTER

3

THEORETICAL FORMULATION FOR THE DETERMINATION OF REFRACTIVE INDEX AND THICKNESS

Refractive index and thickness are generally considered to be the fundamental parameters in optical characterization of thin films. The inhomogeneity and interfacial roughness, which are the characteristics of practical thin films, complicate the determination of these fundamental parameters on such films. This chapter presents a general theoretical formulation for the determination of refractive index and thickness, which is completely based on the multiple beam interference pattern in specular reflectance and transmittance measurements. The theoretical formulation is general in the sense that it is not merely applicable to PS systems but to any thin film whether or not it contains inhomogeneity and interfacial roughness.

3.1 MATHEMATICAL CONSTRUCTIONS OF SPECULAR REFLECTANCE AND TRANSMITTANCE FOR FILM–SUBSTRATE SYSTEM

On films with inhomogeneity and interfacial roughness, a propagating electromagnetic wave undergoes scattering. The scattering affects the magnitudes of specular reflectance and transmittance. This section presents the mathematical constructions of specular reflectance and transmittance for such thin films.

TH-1099_04612102

3.1.1 Waves at rough interfaces

Specular reflectance and transmittance of an electromagnetic wave from a smooth interface, separating the medium i and j, can be given by Fresnel's coefficients r_{ij} and t_{ij}, respectively. In the case of rough interface, the specular reflectance r_{ij}' and the transmittance t_{ij}', in the amplitude, are given by [1]

$$r_{ij}' = \zeta^{1/2} r_{ij} \tag{3.1a}$$

$$t_{ij}' = \zeta^{1/2} t_{ij} \tag{3.1b}$$

where $\zeta^{1/2}$ is the modulation in the amplitude due to interfacial roughness. $\zeta^{1/2}$, in general, is a complex number; the real part corresponds to the fraction of coherent radiation in the regular propagation direction and the imaginary part corresponds to the surface diffraction. For systems, where the interfacial roughness shows no regularity, as in Fig. 3.1, $\zeta^{1/2}$ is a real and positive number. Henceforth, the discussions on interfacial roughness would be based on the systems that show no regularity in roughness. In such systems, the intensity equivalent of $\zeta^{1/2}$ is denoted as ζ, the interfacial modulation coefficient, which corresponds to the intensity of coherent radiation in the direction of normal propagation. Then, the term

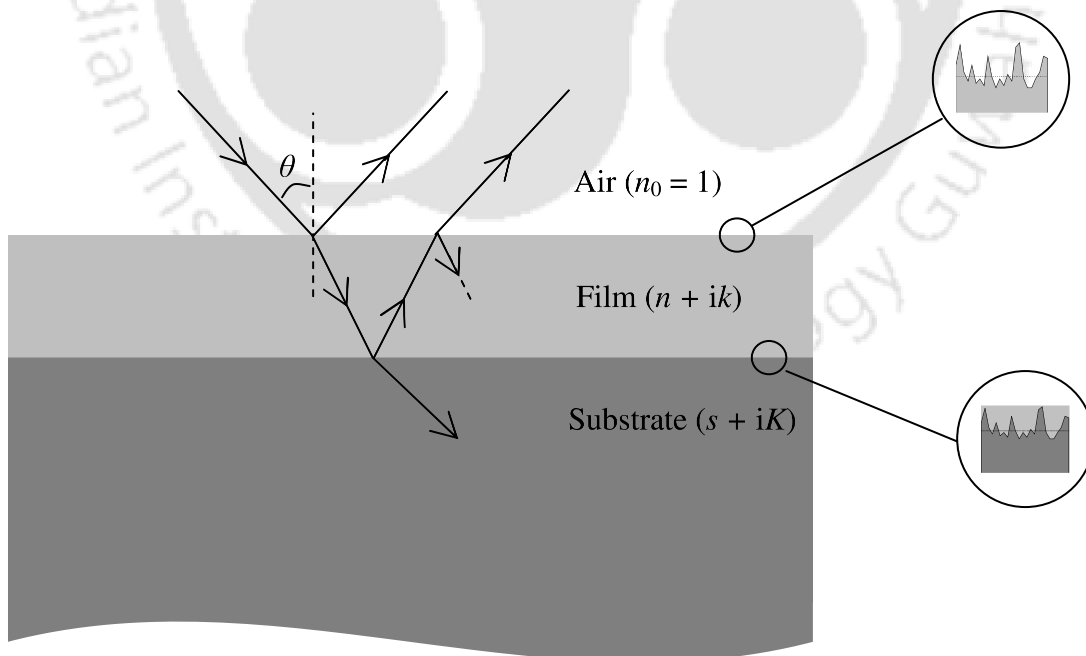

Figure 3.1 A schematic of an inhomogeneous film with rough interfaces on a thick substrate.

TH-1094_04612102

(1-ζ) would signify both the loss of coherency and magnitude in the regular propagation direction at the interface. Numerical values of ζ would lie between 1 and 0 (1 is for a smooth interface and 0 is for a rough interface where there is a total loss of coherence).

3.1.2 Waves in inhomogeneous medium

The amplitude E of a propagating electromagnetic wave, in an inhomogeneous medium, is given by [2, 3]

$$E = E_0 \exp[i(4\pi\, n\, d / \lambda + i\, \alpha_{ext}\, d)] \tag{3.2}$$

where E_0 is the amplitude at the entrance of the medium, n is the real part of the complex refractive index, α_{ext} is extinction coefficient, which is the sum of absorption and volume scattering coefficients α_a and α_s, respectively i.e., $\alpha_{ext} = \alpha_a + \alpha_s$ and d is the penetration depth. The volume scattering coefficient α_s would correspond to the loss of both coherency and magnitude in the regular propagation direction. Unlike ζ, α_s is not bound. However, there exists a lower bound – zero, which is for a homogeneous medium. For an inhomogeneous medium, α_s is a positive non-zero number.

3.1.3 Mathematical expressions for specular reflectance and transmittance of film-substrate system

The practical situation of a film-substrate system is depicted in Fig. 3.1, where the film is considered to have both interfacial roughness and inhomogeneity with refractive index $n + ik$. A complete mathematical treatment of specular reflectance or transmittance of an electromagnetic wave, for the system shown in Fig. 3.1, would necessarily consider the superposition of multiple reflections at all the three interfaces (air/film, film/substrate and substrate/air interfaces) and the scattering due to interfacial roughness and inhomogeneity. Depending on the substrate's optical properties and the transmittance or reflectance of the system, there exist several cases. In the following, the mathematical expressions for two major practical cases are shown:

3.1.3.1 *Case I: Normal incidence transmittance of an inhomogeneous film on homogeneous transparent substrate*

In this case, the substrate, onto which the film is deposited, is considered transparent with refractive index s and also homogeneous with optically smooth surfaces. By

homogeneous and smooth surfaces, it is meant that the incoherent scattering, due to inhomogeneity and surface roughness, is not dominant in the magnitude of spectral transmittance.

Now, the normal incidence transmittance of the film-substrate system, for a plane wave, considering the superposition of multiple reflections at all the three interfaces and the scattering due to inhomogeneity and interfacial roughness of the film, is given by

$$T = \frac{|t_{12}\, t_{23}\, (x\, \zeta_I\, \zeta_{II})^{1/2} \exp(i\beta_T/2)|^2\, |t_{31}|^2}{|1 + r_{12}\, r_{23}\, x\, (\zeta_I\, \zeta_{II})^{1/2} \exp(i\beta_T)|^2 - \zeta_{II}\, |r_{31}|^2 |r_{23} + r_{12}\, x\, (\zeta_I\, \zeta_{II})^{1/2} \exp(i\beta_T)|^2} \qquad (3.3)$$

where

$$t_{12} = \frac{2}{(n+1) + ik} \qquad t_{23} = \frac{2\,(n + ik)}{(s+n) + ik} \qquad t_{31} = \frac{2\,s}{1+s} \qquad (3.4a)$$

$$r_{12} = \frac{(n-1) + ik}{(n+1) + ik} \qquad r_{23} = \frac{(s-n) - ik}{(s+n) + ik} \qquad r_{31} = \frac{1-s}{1+s} \qquad (3.4b)$$

$$x = \exp[-\alpha_{ext}\, d] \qquad (3.4c)$$

$$\beta_T = 4\pi\, n\, d\, /\, \lambda \qquad (3.4d)$$

and ζ_I and ζ_{II} are the interfacial modulation coefficients of the air/film and film/substrate interfaces, respectively.

On performing the algebra of Eq. (3.3), the transmittance of the film-substrate system would be given as

$$T = \frac{A_T\, x\, \zeta_I\, \zeta_{II}}{B_T + C_T\, x\, (\zeta_I\, \zeta_{II})^{1/2} + D_T\, x^2\, \zeta_I\, \zeta_{II}} \qquad (3.5)$$

where

$$A_T = 64\, s^2\, (n^2 + k^2)$$

$$B_T = [(n+1)^2 + k^2]\, \{[(s+n)^2 + k^2]\, (s+1)^2 - [(s-n)^2 + k^2]\, \zeta_2 (s-1)^2\}$$

$$C_T = \{(n^2 + k^2 - 1)\, (s^2 - n^2 - k^2)\, [(s+1)^2 - \zeta_2\, (s-1)^2] + 4k^2 s\, [(s+1)^2 + \zeta_2 (s-1)^2]\}\, 2\cos\beta_T$$
$$- \{k(s^2 - n^2 - k^2)\, [(s+1)^2 - \zeta_2 (s-1)^2] - ks\, (n^2 + k^2 - 1)\, [(s+1)^2 + \zeta_2 (s-1)^2]\}\, 2\sin\beta_T$$

$$D_T = [(n-1)^2 + k^2]\, \{[(s-n)^2 + k^2]\, (s+1)^2 - [(s+n)^2 + k^2]\, \zeta_2 (s-1)^2\}$$

TH-1096_04612102

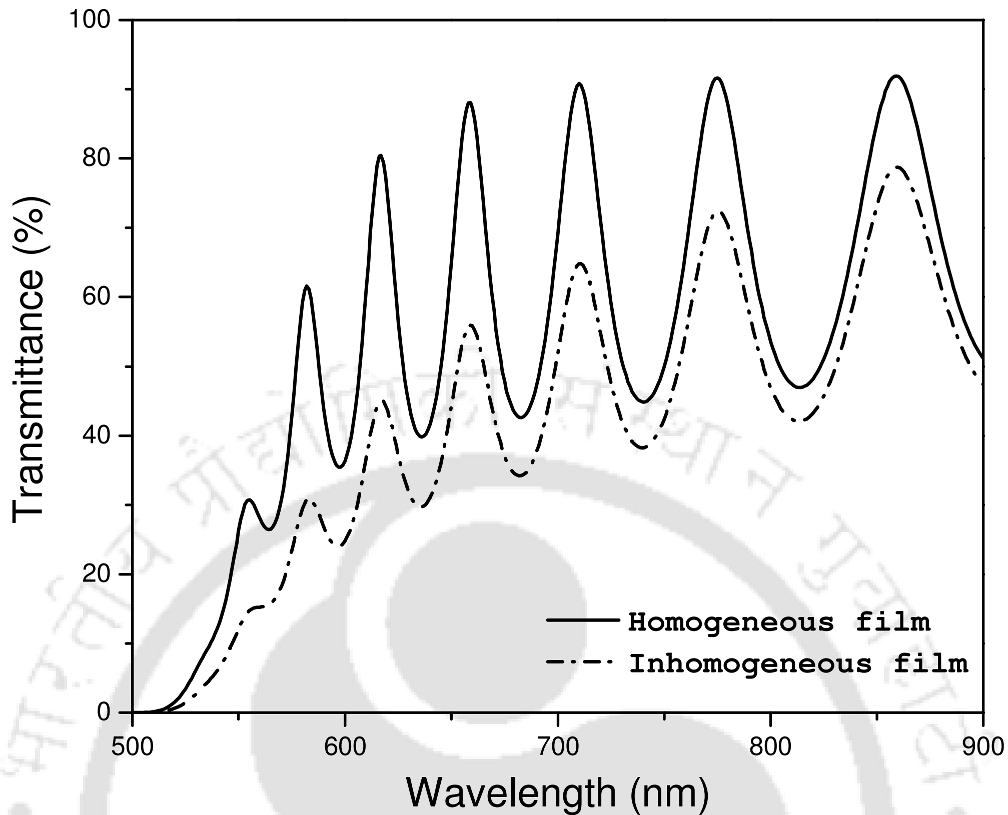

Figure 3.2 Simulations of normal incidence transmittance of homogeneous film with smooth interfaces (continuous line) and inhomogeneous film with rough interfaces (broken line) on transparent substrate through Eq. (3.5). Numerical values of optical and scattering parameters are from Section 3.5 (Numerical simulations).

To give an idea on the effect of inhomogeneity and interfacial roughness on the transmittance, simulations of spectral transmittance, through Eq. (3.5), are shown in Fig. 3.2. The optical and scattering parameters for the simulation of the spectra are given in Sec. 3.5 (Numerical simulations).

3.1.3.2 *Case II: Specular reflectance of an inhomogeneous film on strongly absorbing substrate*

Unlike transmittance measurements, specular reflectance measurements are performed at oblique incidence due to the limitations of optics. At oblique incidence, it is necessary to consider the polarization state of the electromagnetic wave. However, at small angles from the surface normal, the magnitudes of reflectance and transmittance of s- and p- polarized waves show insignificant deviation from the normal incidence magnitudes. So, at near

normal incidence, the normal incidence Fresnel's coefficients would suffice for the mathematical treatment of electromagnetic wave propagation.

In this case, since the substrate, onto which the film is deposited, is strongly absorbing with refractive index $s + iK$, the complexity in the mathematics is reduced by omitting the reflection from substrate's back interface, i.e., substrate/air interface. A film deposited on a strongly absorbing substrate not only simplifies the mathematics, but also avoids the modulations in the measured reflectance spectrum due to substrate/air interfacial roughness and inhomogeneity of the substrate.

Now, considering the superposition of multiple reflections only within the film and the scattering due to inhomogeneity and rough interfaces of the film, the specular reflectance of the film-substrate system at a small angle of incidence θ from the normal, for a plane wave, is given by

$$\mathrm{R} = \frac{\zeta_{\mathrm{I}} \, |r_{12} + r_{23}\, x\, (\zeta_{\mathrm{I}}\, \zeta_{\mathrm{II}})^{1/2} \exp(i\beta_{\mathrm{R}})|^2}{|1 + r_{12}\, r_{23}\, x\, (\zeta_{\mathrm{I}}\, \zeta_{\mathrm{II}})^{1/2} \exp(i\beta_{\mathrm{R}})|^2} \qquad (3.6)$$

where

$$\beta_{\mathrm{R}} = \frac{4\pi\, d}{\lambda} \left(\tfrac{1}{2} \{(n_{\mathrm{i}}^2 - k_{\mathrm{i}}^2 - \sin^2\theta_{\mathrm{j}}) + [(n_{\mathrm{i}}^2 - k_{\mathrm{i}}^2 - \sin^2\theta_{\mathrm{j}})^2 + 4\, n_{\mathrm{i}}^2\, k_{\mathrm{i}}^2]^{1/2}\}\right)^{1/2} \qquad (3.7)$$

and r_{12}, r_{23}, x, ζ_{I} and ζ_{II} retain their mathematical forms and meanings as in Eq. (3.3).

On performing the algebra of Eq. (3.6), the reflectance of the film-substrate system would be given as

$$\mathrm{R} = \frac{\zeta_{\mathrm{I}}\, [\mathrm{A_R} + \mathrm{B_R}\, x\, (\zeta_{\mathrm{I}}\, \zeta_{\mathrm{II}})^{1/2} + \mathrm{C_R}\, x^2\, \zeta_{\mathrm{I}}\, \zeta_{\mathrm{II}}]}{\mathrm{D_R} + \mathrm{E_R}\, x\, (\zeta_{\mathrm{I}}\, \zeta_{\mathrm{II}})^{1/2} + \mathrm{F_R}\, x^2\, \zeta_{\mathrm{I}}\, \zeta_{\mathrm{II}}} \qquad (3.8)$$

where

$$\mathrm{A_R} = [(n + 1)^2 + k^2]\, [(n - 1)^2 + k^2]\, [(s + n)^2 + (K + k)^2]$$

$$\begin{aligned}\mathrm{B_R} = 4\, [&\{(s^2 - n^2 + K^2 - k^2)\, [(n^2 + k^2 + n)\, (n - 1) + k^2] + 2\, [(Kn - ks)k(n^2 + k^2 + 1)]\}\, 2 \cos\beta_R \\ &- \{2\, (Kn - ks)\, [(n^2 + k^2 + n)\, (n - 1) + k^2] - (s^2 - n^2 + K^2 - k^2)\, k\, (n^2 + k^2 + 1)\}\, 2 \sin\beta_R] \\ &+ \\ &[(n - 1)^2 + k^2]\, [\{(s^2 - n^2 + K^2 - k^2)\, [(n^2 + k^2 - 1)\, (n - 1) + k^2] - 4\, (Kn - ks)\, k\}\, 2 \cos\beta_R \\ &- \{2\, (Kn - ks)\, (n^2 + k^2 - 1) - 2\, (s^2 - n^2 + K^2 - k^2)\, k\}\, 2 \sin\beta_R]\end{aligned}$$

$$\mathrm{C_R} = [(s - n)^2 + (K - k)^2]\, \{16\, (n^2 + k^2) + [(n - 1)^2 + k^2]^2 + 8\, [(n\, (n - 1)^2 + k^2\, (n - 2)]\}$$

TH-1098_04612102

$D_R = [(n + 1)^2 + k^2]^2 [(s + n)^2 + (K + k)^2]$

$E_R = [(n + 1)^2 + k^2] [\{(s^2 - n^2 + K^2 - k^2) (n^2 + k^2 - 1) - 4 (K n - k s) k\} 2 \cos\beta_R$
$- \{2 (s^2 - n^2 + K^2 - k^2) k + 2 (K n - k s) (n^2 + k^2 - 1)\} 2 \sin\beta_R]$

$F_R = [(n + 1)^2 + k^2] [(n - 1)^2 + k^2] [(s - n)^2 + (K - k)^2]$

To give an idea on the effect of inhomogeneity and interfacial roughness on the spectral reflectance, simulations of specular reflectance at 20° angle of incidence, through Eq. (3.8), are shown in Fig. 3.3. The optical and scattering parameters for the simulation of the spectra are given in Sec. 3.5 (Numerical simulations).

From the comparison of the simulations of both transmittance and reflectance of homogeneous and inhomogeneous films, it is observed that the inhomogeneity merely affects the magnitude of the spectra and not their interference fringe positions. This would mean that the conditions for interference are unaffected by the inhomogeneity.

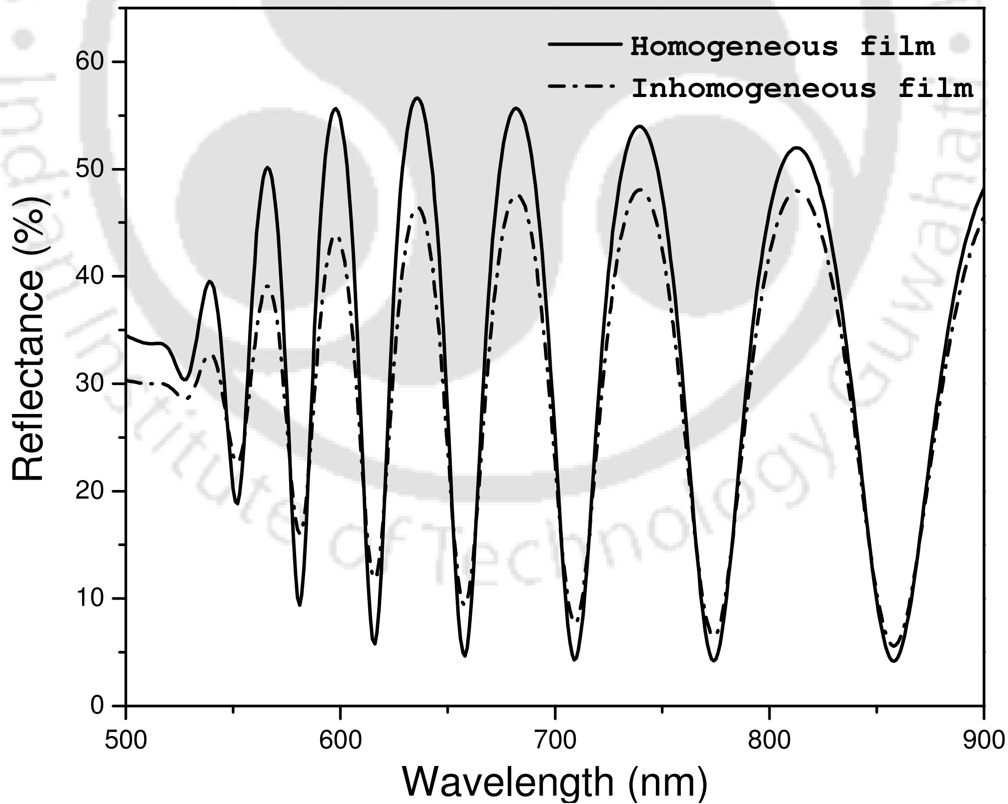

Figure 3.3 Simulations of specular reflectance of homogeneous film with smooth interfaces (continuous line) and inhomogeneous film with rough interfaces (broken line) on transparent substrate through Eq. (3.8) at an incident angle of 20°. Numerical values of optical and scattering parameters are from Section 3.5 (Numerical simulations).

3.2 INTERFERENCE CONDITIONS

The condition for interference fringes in the normal incidence transmittance spectrum under the assumptions that the scattering due to inhomogeneity and interfacial roughness and the absorption are weakly spectral dependent can be given as

$$2\, d\, n_{\mathrm{i}} = m\, \lambda_{\mathrm{i}} \qquad (3.9)$$

where m is the interference fringe order and the subscript 'i' is to indicate the dispersion. When the film is deposited on a lower index substrate, i.e, $s<n$, m takes integer and half integer values for maxima and minima, respectively. When $s>n$, the condition for maxima and minima would be reversed.

With the same assumptions, the condition for interference fringes in the specular reflectance spectrum would be given as

$$2\, d\, (\tfrac{1}{2}\, \{(n_{\mathrm{i}}^2 - k_{\mathrm{i}}^2 - \sin^2\theta_{\mathrm{j}}) + [(n_{\mathrm{i}}^2 - k_{\mathrm{i}}^2 - \sin^2\theta_{\mathrm{j}})^2 + 4\, n_{\mathrm{i}}^2\, k_{\mathrm{i}}^2]^{1/2}\})^{1/2} = m\, \lambda_{\mathrm{i}} \qquad (3.10)$$

where the subscript 'j' is to indicate the interference fringe shift with θ. When $s<n$, m takes integer and half integer values for minima and maxima, respectively, and would be reversed when $s>n$.

In the spectral region of interference fringes, $k^2 << n^2$ [4], so, Eq. (3.10) can be reduced to

$$2\, d\, (n_{\mathrm{i}}^2 - \sin^2\theta_{\mathrm{j}})^{1/2} = m\, \lambda_{\mathrm{i}} \qquad (3.11)$$

3.3 DETERMINATION OF INTERFERENCE FRINGE ORDER, THICKNESS AND REFRACTIVE INDEX

Equations (3.9) and (3.11) are the governing relations for the spectral interference in transmittance and reflectance measurements, respectively. The parameters m, d and n in Eqs. (3.9) and (3.11) are to be determined. In the following, the mathematical steps in the determination of these parameters are presented only for the reflectance case. The determination procedures for the case of transmittance are given at the APPENDIX.

3.3.1 Determination of the interference fringe order, *m*

As a first step towards the determination of optical constants, the interference fringe order m is to be determined for every maximum and minimum in the measured spectrum. In literature, there exist a few procedures for the determination of m. However, the existing

TH-1090_04612102

procedures either demand optically thick films [5] or destructive imaging techniques (cross-sectional imaging) [6]. Here, two non-destructive methods for the determination of m are suggested. The only prerequisite for the methods is to have a knowledge of whether the substrate's refractive index s is greater or lower than the film's refractive index n, i.e., $s>n$ or $s<n$.

3.3.1.1 *Method I*

Simulate a reflectance (transmittance) spectrum through Eq. (3.8) (Eq. (3.5) for transmittance) such that the simulated spectrum closely resembles the interference pattern in the measured spectrum. For the purpose of simulation, it is sufficient to consider an arbitrary $n(\lambda)$ and d, which are not necessarily appropriate to the system under consideration. Also, since the interference conditions in Section 3.2 are under the assumptions that the absorption and scattering are weakly spectral dependent, for the purpose of simulation, the system can be considered non-absorbing and homogeneous. For the simulated spectrum, m follows from Eq. (3.11) (Eq. (3.9) for transmittance). As the simulated spectrum closely resembles the measured spectrum, m for any maximum or minimum in the simulated spectrum could be assigned to the corresponding maximum or minimum in the measured spectrum.

It is noteworthy that m as obtained by this procedure is independent of the kind of $n(\lambda)$ and d used for the reproduction of the measured interference pattern.

3.3.1.2 *Method II*

An alternate method, which is applicable only in optically thin region of the spectrum, i.e., the region of lower interference orders, is given in the following.

Consider the interference conditions in the specular reflectance spectrum for two adjacent interference orders

$$2\, d\, (n_1^2 - \sin^2\theta)^{1/2} = \Omega\, \lambda_1 \tag{3.12}$$

$$2\, d\, (n_2^2 - \sin^2\theta)^{1/2} = (\Omega - 0.5)\, \lambda_2 \tag{3.13}$$

where Ω is the interference order, which is to be determined.

From Eqs. (3.12) and (3.13), Ω is given as

$$\Omega = \frac{0.5\, \lambda_2}{(\lambda_2 - \lambda_1)} - \frac{2\, d\, (n_1 - n_2)}{(\lambda_2 - \lambda_1)} \left\{ 2 + \frac{\sin^2\theta}{n_1\, n_2} \right\} \tag{3.14}$$

In optically thin region of the spectrum, the denominator of second term, in Eq. (3.14), is several times greater than the numerator, and so Eq. (3.14) can be reduced to

$$\Omega_0 = \frac{0.5\,\lambda_2}{(\lambda_2 - \lambda_1)} \tag{3.15}$$

where the subscript '0' is to indicate the approximation.

Ω_0 is clearly an overestimate of Ω. However, since we already know whether a particular interference order is integer or half integer (from the knowledge of whether $s>n$ or $s<n$), the nearest lower integer or half integer is the interference order Ω for the particular fringe.

3.3.2 Determination of film thickness, *d*

For the determination of *d*, minimum two spectral measurements with different angles of incidence, in the spectral region of interference fringes, are required. When the film is deposited on a transparent substrate, a normal incidence transmittance and an oblique incidence specular reflectance would suffice for the determination of *d*. When the film is deposited on an opaque substrate, specular reflectance at two different angles of incidence can be considered. Figures 3.4(a) and 3.4(b) show the simulated spectra for the determination of *d* for the film on transparent and opaque substrates, respectively. In the following, the necessary mathematical relations for a film on opaque substrate considering the reflectance measurements at two different angles of incidence are presented.

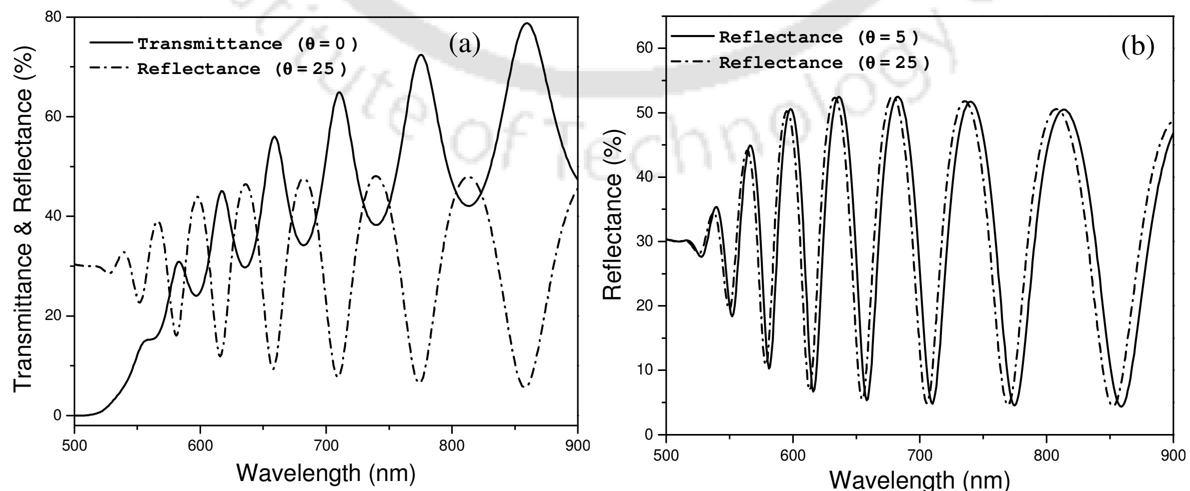

Figure 3.4 Simulated spectra for the determination of d for the film on (a) transparent and (b) opaque substrate.

TH-1092_04612102

(Necessary mathematical relations for the determination of d for the film on a transparent substrate are given in APPENDIX)

The interference conditions for the incident angles θ_I and θ_{II} at a particular interference fringe order Ω would be given as

$$2\,d\,(n_1^2 - \sin^2\theta_I)^{1/2} = \Omega\,\lambda_1 \tag{3.16}$$

$$2\,d\,(n_1^2 + \gamma - \sin^2\theta_{II})^{1/2} = \Omega\,\lambda_2 \tag{3.17}$$

where Ω is the interference fringe order at λ_1 and λ_2 and γ compensates the dispersion of refractive index between λ_1 and λ_2.

From Eqs. (3.16) and (3.17), d would be given as

$$d = \left[\frac{\Omega^2\,(\lambda_1^2 - \lambda_2^2)}{4\,(\sin^2\theta_{II} - \sin^2\theta_I - \gamma)}\right]^{1/2} \tag{3.18}$$

Since Eq. (3.18) contains an undetermined parameter γ, d is not calculable from Eq. (3.18). If γ = 0, then, Eq. (3.18) reduces to

$$d_0 = \left[\frac{\Omega^2\,(\lambda_1^2 - \lambda_2^2)}{4\,(\sin^2\theta_{II} - \sin^2\theta_I)}\right]^{1/2} \tag{3.19}$$

where the subscript '0' is to indicate the approximation.

Now, d_0 is although calculable and a close estimate of d, it can only be considered as a first step in the determination of d. A better estimation of d can be made through Eq. (3.18) once γ is found.

For the determination of γ, consider the interference condition, adjacent to the interference fringe order Ω, in the specular reflectance at θ_I, which follows from Eq. (3.9) as

$$2\,d\,(n_1^2 + \delta - \sin^2\theta_I)^{1/2} = (\Omega + 0.5)\,\lambda_3 \tag{3.20}$$

where δ compensates the dispersion of refractive index between λ_1 and λ_3.

From Eqs. (3.16) and (3.20), δ would be given by

$$\delta = \frac{(\Omega + 0.5)^2\,\lambda_3^2 - \Omega^2\,\lambda_1^2}{4\,d^2} \tag{3.21}$$

In the spectral region of interference fringes ($k^2 << n^2$), the normal dispersion of

refractive index can be given as

$$n_i^2 = G + \frac{H}{\lambda_i^p} \tag{3.22}$$

where G, H and p are constants whose values depend on the material and the subscript 'i' is used to indicate the dispersion.

Then, γ would be given by

$$\gamma = \frac{\delta\, \lambda_3^p\, (\lambda_2^p - \lambda_1^p)}{\lambda_2^p\, (\lambda_3^p - \lambda_1^p)} \tag{3.23}$$

Having shown the necessary mathematical relations, the determination of d is made by an iterative procedure. The flowchart of the iteration is shown in Fig. 3.5.

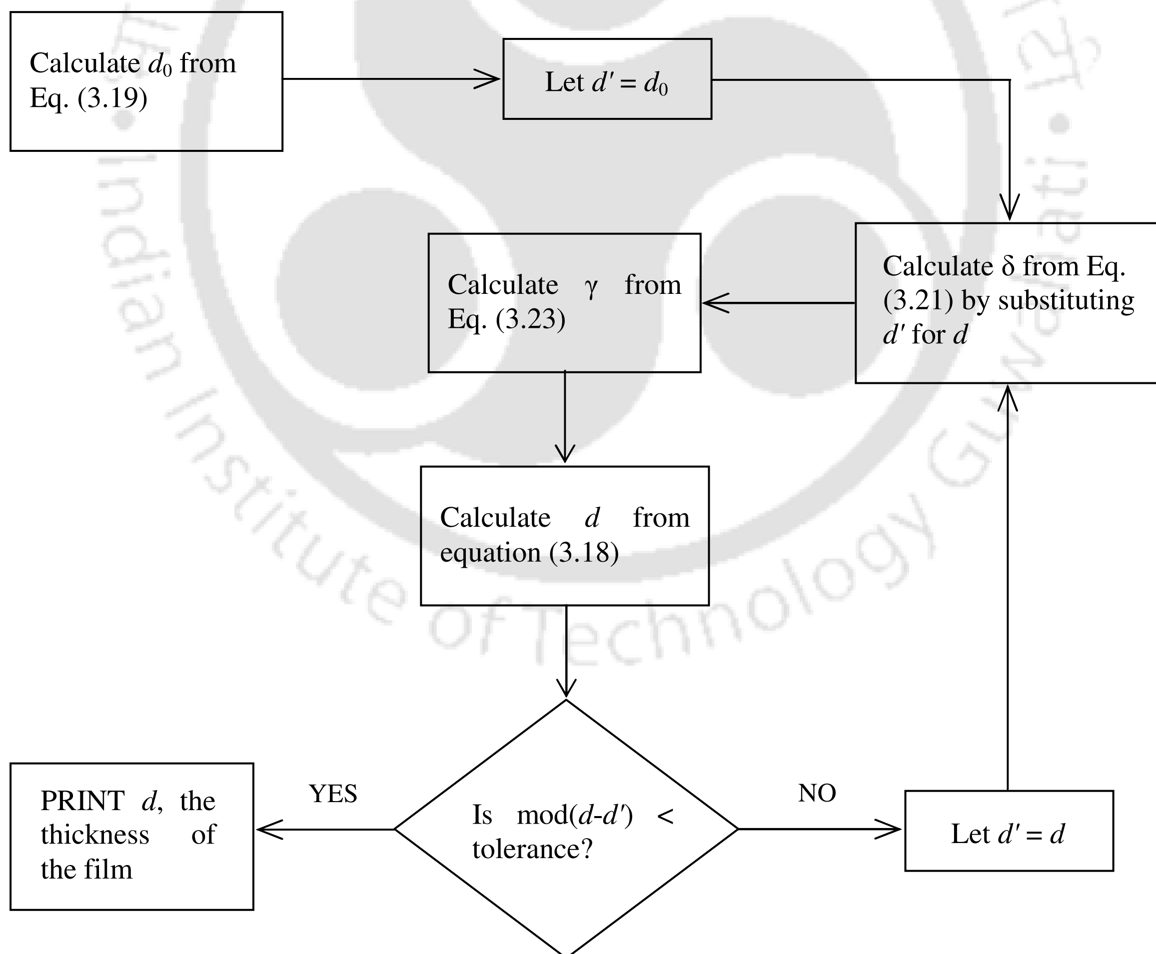

Figure 3.5 Flow chart of the iterative procedure for the determination of film thickness d.

TH-1094_04612102
Indian Institute of Technology Guwahati

3.3.3 Determination of the real part of the refractive index, *n*

Once m and d are determined, n for normal incidence spectral transmittance follows from Eq. (3.9) as

$$n_i = \frac{m\,\lambda_i}{2\,d} \tag{3.24}$$

and for specular reflectance at an angle of incidence θ_j, n follows from Eq. (3.11) as

$$n_i = \left[\frac{m^2\lambda_i^{\,2}}{4\,d^2} + \sin^2\theta_j\right]^{1/2} \tag{3.25}$$

where d is the thickness of the film as obtained from the iterative procedure.

Equations (3.24) and (3.25) allow the determination of n only at discrete values of λ. However, using numerical interpolation techniques n at all intermediate values of λ can be determined.

3.4 MATHEMATICAL CONSTRUCTION OF SPECULAR REFLECTANCE OF POROUS SILICON SYSTEM

Porous Si (PS) is a composite of Si and voids. Inherent to any composite are inhomogeneity and interfacial roughness. A schematic of PS on c-Si substrate is shown in Fig. 3.6. The determination procedures of n and d as described in the previous sections for films with inhomogeneity and interfacial roughness are applicable to PS systems also. However, due to its composite nature, there are a few conceptual differences in the mathematical construction of specular reflectance of PS system that are elaborated in the following subsections with reference to Fig. 3.6.

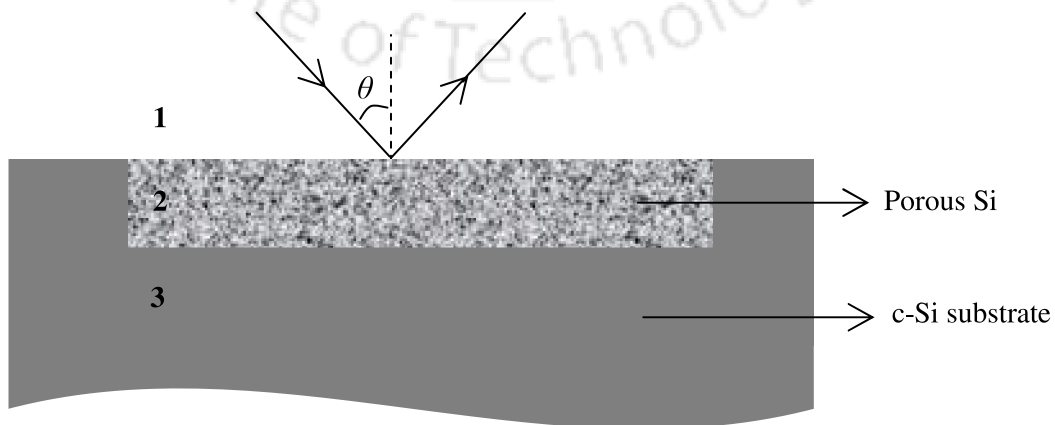

Figure 3.6 A schematic of the cross-section of PS film on c-Si substrate.

3.4.1 Waves in PS media

The propagation of an electromagnetic wave in a composite media, where the size of the constituents and the average distance between the constituents are much less than the wavelength of the propagating wave, is described by an effective refractive index. In the case of PS, at optical wavelengths and above, the propagation of an electromagnetic wave can be described by an effective refractive index. Hence, the amplitude of the propagating electromagnetic wave E, in a PS medium, is given by

$$E = E_0 \exp[\mathrm{i}(4\pi\, n_{\mathrm{eff}}\, d / \lambda + \mathrm{i}\, \alpha_{\mathrm{ext}}\, d)] \tag{3.26}$$

where E_0 is the amplitude of the wave at the entrance of the medium, n_{eff} is the real part of the effective refractive index, α_{ext} is the extinction coefficient and d is the depth of penetration of the wave. Equation (3.26) is very similar to that of Eq. (3.2) with the only difference being n replaced by n_{eff}.

3.4.2 Waves at PS interfaces

Specular reflectance and transmittance at the interfaces of non-composite materials are given by Fresnel's reflectance and transmittance coefficients, respectively, which are the functions of bulk refractive indices of the materials on either side of the interface. However, in composite systems, specular reflectance and transmittance are associated with the optical constants and the occupied volume fractions of all the individual homogeneous components constituting the composite at the interfaces (air/film and film/substrate interfaces) and their microscopic geometry. In the case of PS, for the air/PS film interface, the specular reflectance r_{12}' and transmittance t_{12}' of an electromagnetic wave, with due considerations of the fractional occupancy of Si and voids and the surface roughness of the constituents (in this case, the roughness is only for Si), are given by

$$r_{12}' = \zeta_{\mathrm{I}}^{1/2}\, r_{12} \tag{3.27a}$$

$$t_{12}' = \zeta_{\mathrm{I}}^{1/2}\, t_{12} \tag{3.27b}$$

and similarly, for the PS film/Si substrate interface, specular reflectance r_{23}' and transmittance t_{23}' are given by

$$r_{23}' = \zeta_{\mathrm{II}}^{1/2}\, r_{23} \tag{3.28a}$$

$$t_{23}' = \zeta_{\mathrm{II}}^{1/2}\, t_{23} \tag{3.28b}$$

where r_{ij} and t_{ij} are the Fresnel's reflectance and transmittance coefficients, respectively at

TH-1096_04612102

an interface separating the media i and j of two different refractive indices and $\zeta_\alpha^{1/2}$ is the modulated fraction of the coherent radiation in the regular propagation direction of the wave due to surface roughness at the interface α.

3.4.3 Mathematical expression for the specular reflectance of PS system

A schematic of the cross-section of PS on c-Si substrate is shown in Fig. 3.6. A complete mathematical treatment of specular reflectance of an electromagnetic wave, for the system under consideration, would necessarily consider the superposition of multiple reflections at the interfaces of PS (air/PS film and PS film/Si substrate interfaces) and the scattering due to interfacial roughness and inhomogeneity. Since the underneath c-Si is strongly absorbing in the visible region of the spectrum and its rear face is textured, the reflection from substrate's back interface, i.e., substrate/air interface is omitted. This reduces the complexity in the mathematics for the specular reflectance of PS film-Si substrate system.

Now, with these considerations the specular reflectance of the PS film-Si substrate system at an angle of incidence θ from the normal, for a plane wave, is given by

$$\mathrm{R} = \frac{\zeta_\mathrm{I}\, |r_{12} + r_{23}\, x\, (\zeta_\mathrm{I}\, \zeta_\mathrm{II})^{1/2} \exp(\mathrm{i}\beta)|^2}{|1 + r_{12}\, r_{23}\, x\, (\zeta_\mathrm{I}\, \zeta_\mathrm{II})^{1/2} \exp(\mathrm{i}\beta)|^2} \tag{3.29}$$

where

$$\beta = \frac{4\pi\, d}{\lambda} (n_\mathrm{eff}^2 - \sin^2\theta)^{1/2} \tag{3.30a}$$

$$x = \exp[-\, \alpha_\mathrm{ext}\, d] \tag{3.30b}$$

and r_{12}, r_{23}, ζ_I and ζ_II retain their meanings as in Eqs. (3.27) and (3.28). Equation (3.29) is functionally same as that of Eq. (3.6). However, as the bulk and interfacial refractive indices are different due to its composite nature, on performing the algebra of Eq. (3.29), the specular reflectance of the PS film-Si substrate system would be given as

$$\mathrm{R} = \frac{\zeta_\mathrm{I}\, [r_{12}^2 + 2\, r_{12}\, r_{23}\, x\, (\zeta_\mathrm{I}\, \zeta_\mathrm{II})^{1/2} \cos\beta + r_{23}^2\, x^2\, \zeta_\mathrm{I}\, \zeta_\mathrm{II}]}{1 + 2\, r_{12}\, r_{23}\, x\, (\zeta_\mathrm{I}\, \zeta_\mathrm{II})^{1/2} \cos\beta + r_{12}^2\, r_{23}^2\, x^2\, \zeta_\mathrm{I}\, \zeta_\mathrm{II}} \tag{3.31}$$

Equation (3.31) can be written in a similar form of Eq. (3.8) by replacing the reflectance coefficients r_{12} and r_{23} with their explicit mathematical functions in terms of the interfacial refractive indices. Doing so would merely increase the number of undeterminable

parameters in the expression and increase its complexity. Besides, as the determination of refractive index and thickness is based only on the interference condition, any further expansion of Eq. (3.31) is not necessary.

The interference pattern of PS systems is entirely governed by the term β in Eq. (3.31). The functional form of β as given by Eq. (3.30a) can be shown to be very similar to that of β_R in Eq. (3.7) when $k^2 << n^2$ with n_{eff} in place of n. As the interference condition in PS systems is same as that of an inhomogeneous film with rough interfaces, the determination procedures developed for n and d of an inhomogeneous film could be used for the determination of n_{eff} and d of PS systems.

3.5 NUMERICAL SIMULATIONS

In order to test the accuracy of the proposed procedure, in the following, the determination of d for a modelled system is presented. Figure 3.7 shows a closer view of the interference pattern of the simulated reflectance spectra for 5° and 25° angles of

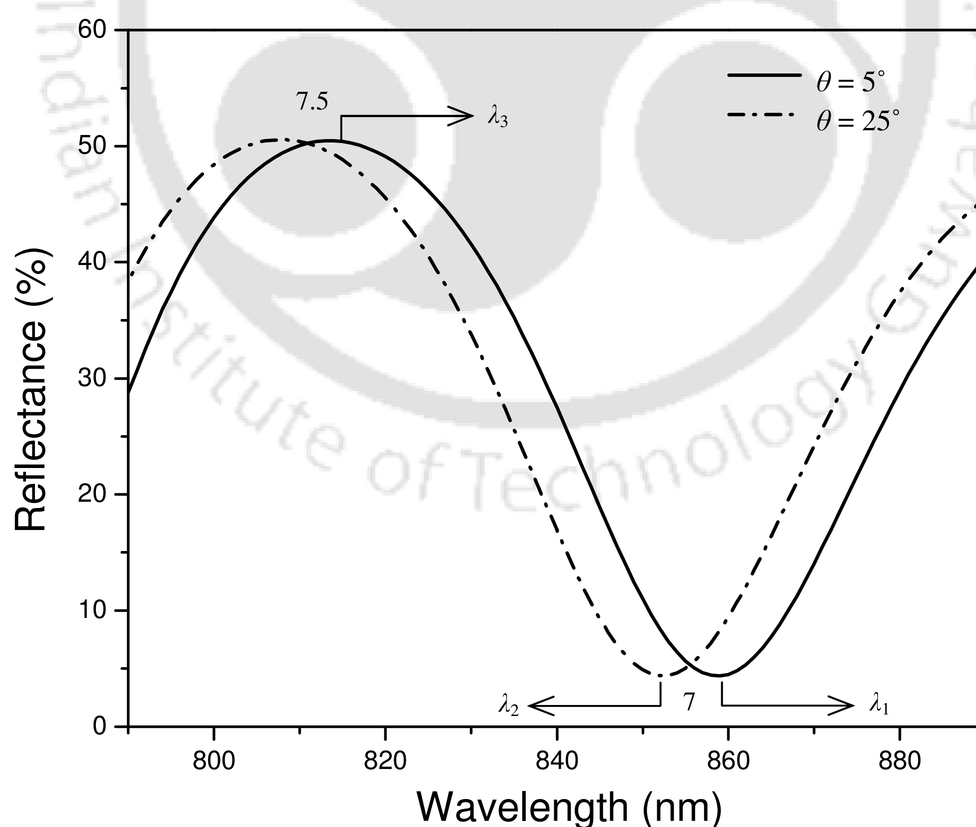

Figure 3.7 A closer view of the shift of the interference pattern with the change of angle of incidence in specular reflectance.

TH-1098_04612102

incidence. The complete spectra have already been shown in Fig. 3.4(b). The numerical values of the optical parameters (n, k and d) and the scattering due to inhomogeneity and interfacial roughness for the simulation of the spectra are given below

$n = (3 \times 10^5) / \lambda^2 + 2.6$ (λ in nm)

$k = \lambda \times 10^{(1.5 \times 10^6 / \lambda^2 - 8)} / (4\pi)$ (λ in nm)

$s = 1.51$

$d = 1000$ nm

$1\text{-}\zeta_I = 7.5 \times 10^9 / \lambda^4$ (λ in nm)

$1\text{-}\zeta_{II} = 5.0 \times 10^9 / \lambda^4$ (λ in nm)

$\alpha_s = 5.0 \times 10^{10} / \lambda^4$ (λ in nm)

The inputs for the determination of d and the results of the iterations are summarized in Table 3.1. In the iteration, the dispersion of refractive index between λ_1 and λ_3 is assumed

Table 3.1 Summary of the results of the iteration in the determination of d.

Inputs			Outputs	
Interference orders	Maxima/minima positions (nm)	Angle of incidence (°)	Resulting d after every iteration (nm)	Error (%)
7	$\lambda_1 = 858.5$	5	$d_0 = 892.4$	10.76
			$d_1 = 1052.7$	5.27
			$d_2 = 999.1$	0.09
	$\lambda_2 = 852.0$	25	$d_2 = 1013.4$	1.34
			$d_2 = 1009.3$	0.93
			$d_2 = 1010.4$	1.04
7.5	$\lambda_3 = 813.5$	5	$d_2 = 1010.1$	1.01
			$d_2 = 1010.2$	1.02
			$d_2 = 1010.2$	1.02

to be proportional to $1/\lambda$. It is observed in Table 3.1 that the results of the iterations oscillate, and finally converges to a value which is very close (~ 1% error) to the actual thickness of the film. To improve the accuracy in the determination of d, it would be sufficient to end the iteration process with d_2, which is the closest estimate of d.

3.6 SUMMARY

To summarize, a general theoretical formulation for the determination of refractive index n and thickness d of thin films through interference in spectral transmittance and reflectance is presented. The conceptual differences in the mathematical construction of specular reflectance of PS systems due to its composite nature and the applicability of the proposed determination procedures to PS systems have been discussed. The accuracy in the determination of d is then shown for a modelled system with simulated spectral reflectance for 5° and 25° angles of incidence. The accuracy in the determination of d is found to be within 0.09 % error.

3.7 REFERENCES

[1] A. Ishimaru, Wave Propagation and Scattering in Random Media, Vol. 2 (Academic Press, Inc, New York, 1978), p. 463

[2] F. A. Jenkins and H. E. White, Fundamentals of Optics, 4th ed. (McGraw-Hill Book Co., Singapore, 1981) p. 458

[3] C. F. Klingshirn, Semiconductor Optics, (Springer-Verlag Berlin Heidelberg New York, 1997) p. 35

[4] M. Nowak, Thin Solid Films **254**, 200 (1995)

[5] J. C. Martínez-Antón and E. Bernabeu, Optics Comm. **132**, 321 (1996)

[6] A. Wolf, B. Terheiden and R. Brendel, J. Appl. Phys. **104**, 033106 (2008)

TH-1090_04612102

CHAPTER

4

STUDIES ON GROWTH RATE AND REFRACTIVE INDEX OF POROUS SILICON

The procedures for determination of refractive index and thickness of thin films as described in Chapter 3 are used in the present chapter for PS films prepared under systematic variations of anodization current density, anodization time and B-doping concentration. The effect of anodization conditions on the refractive index and thickness would provide details on the modulations of microstructure and growth kinetics of PS with the anodization conditions.

4.1 DETERMINATION OF THICKNESS AND REFRACTIVE INDEX OF PS

Although the determination procedures of refractive index and thickness follow from Chapter 3, when applied to real thin films, the procedures slightly get modified depending on the qualities of the thin films. In PS prepared on high B-doping concentration c-Si wafers (0.001–0.005 and 0.01–0.05 Ω cm), the interference pattern in the measured spectrum could readily be fitted with effective medium theory (EMT). However, in PS prepared on low B-doping concentration c-Si wafers (0.1-0.5, 1-10 and >50 Ω cm), the interference pattern in the measured spectrum could not be fitted with EMT. Depending on fitting and non-fitting of the measured interference pattern with EMT, the determination

TH-1099_04612102

procedures of refractive index and thickness slightly differ between PS prepared from high and low B-doping concentration c-Si wafers. In the following, the determination procedures of thickness *d* and effective refractive index n_{eff} of PS prepared on high and low B-doping concentration wafers are exemplified with two PS films, which are the representatives of the two cases.

4.1.1 High B-doping concentration wafers (0.001-0.005 and 0.01-0.05 Ω cm)

Figures 4.1 and 4.2 show the measured specular reflectance spectra of PS prepared on c-Si wafers of resistivities 0.001–0.005 and 0.01–0.05 Ω cm, respectively. The anodization current densities used for the preparation of these PS are 25, 50 and 75 mA/cm^2. The

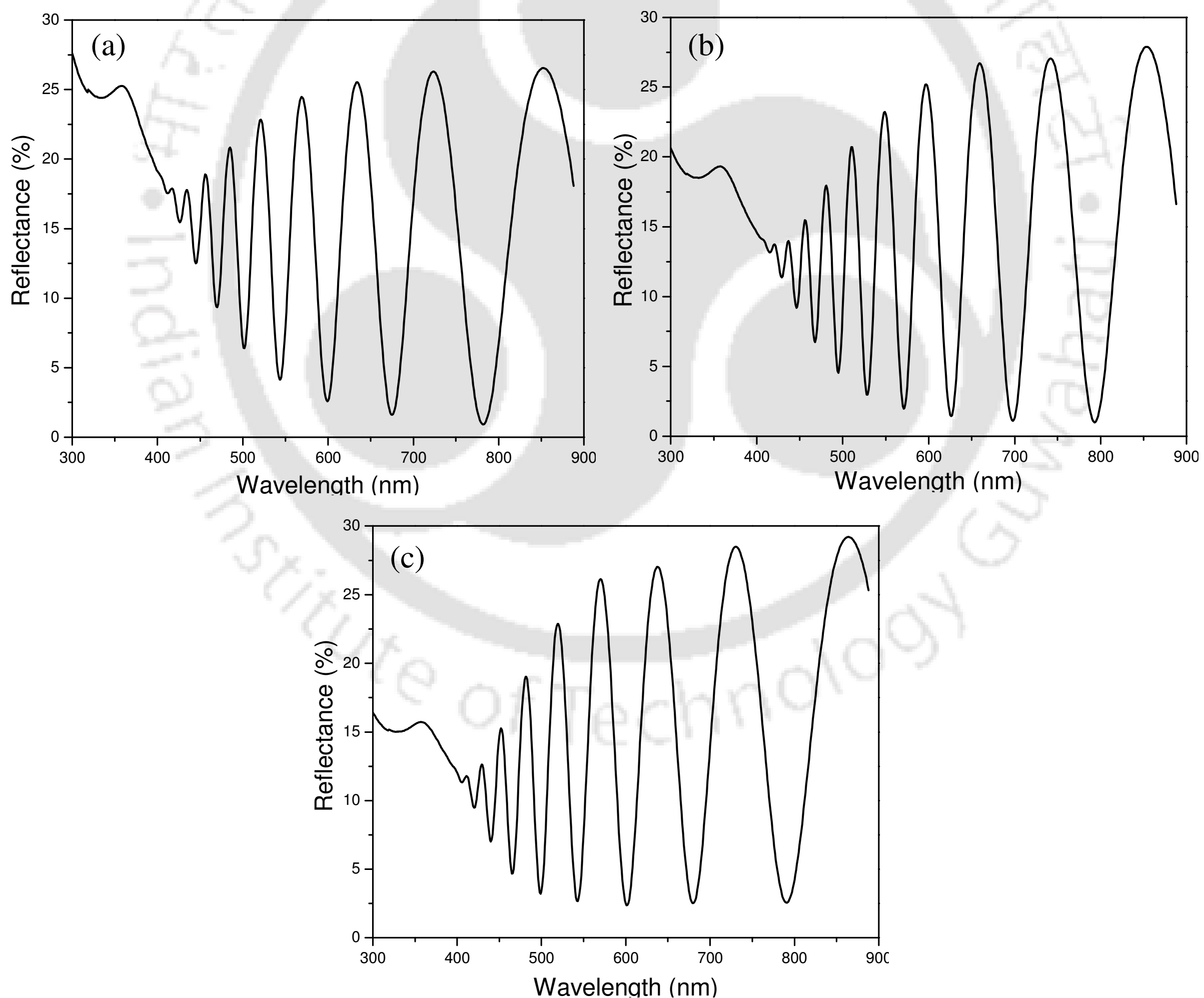

Figure 4.1 Measured specular reflectance of PS prepared on 0.001–0.005 Ω cm c-Si wafer using (a) 25 mA/cm^2 current density for 60 sec (b) 50 mA/cm^2 current density for 45 sec and (c) 75 mA/cm^2 current density for 30 sec. The spectra are recorded at 8° angle of incidence.

TH-1092_04612102

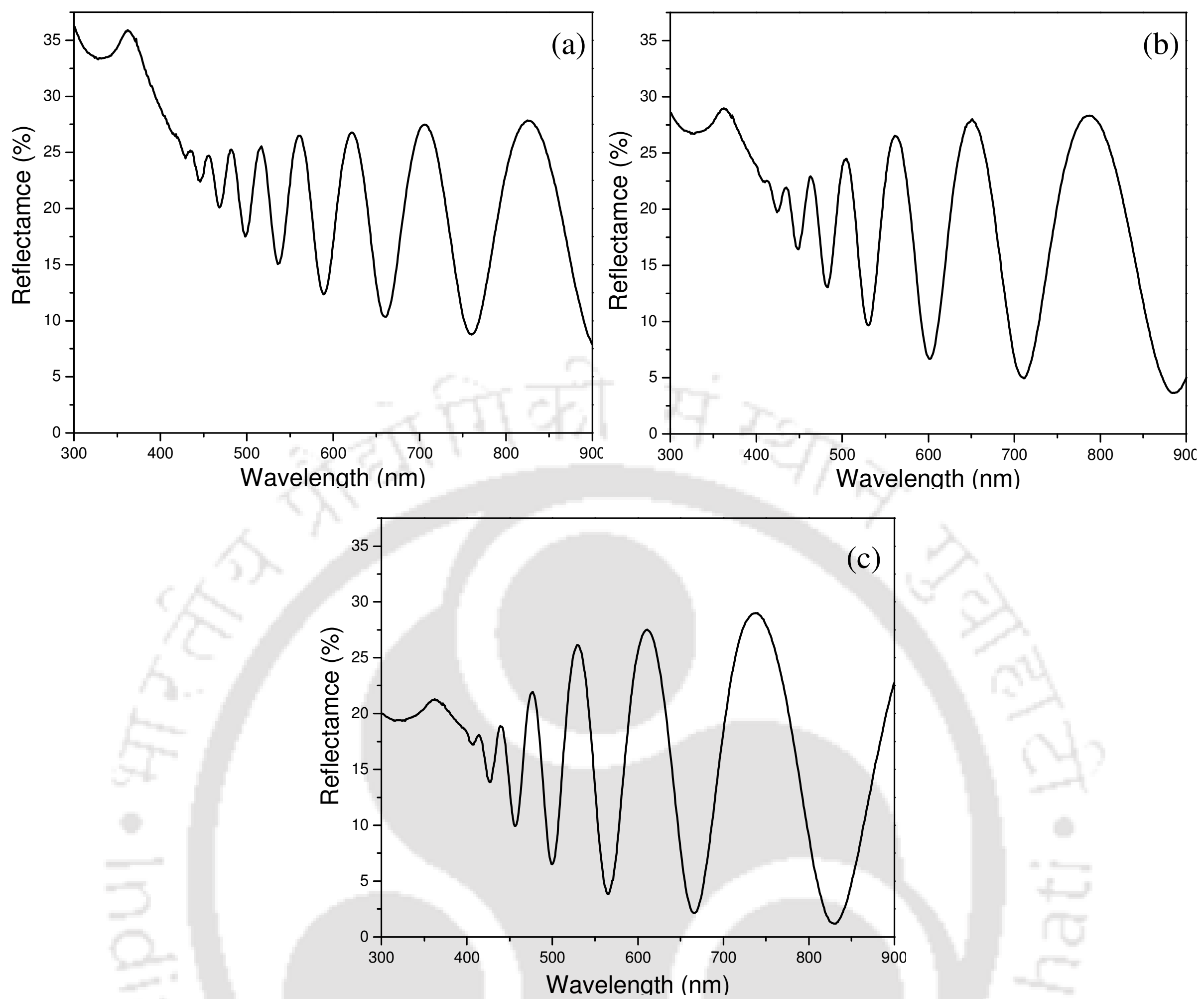

Figure 4.2 Measured specular reflectance of PS prepared on 0.01–0.05 Ω cm c-Si wafer using (a) 25 mA/cm^2 current density for 30 sec (b) 50 mA/cm^2 current density for 15 sec (c) 75 mA/cm^2 current density for 12 sec. The spectra are recorded at 45° angle of incidence.

observed oscillations in the reflectance spectra are the multiple beam interference patterns similar to that of the simulations of Chapter 3. In all the spectra, the interference pattern fades with the decrease of wavelength, and disappears completely near around 400 nm. This fading of the interference pattern, in general, is due to incoherent scattering and absorption of electromagnetic radiation in the medium. In the present case of PS, it is largely due to the absorption of radiation in the medium. It is also observed in Figs. 4.1 and 4.2 that the interference free reflectance decreases with the increase of anodization current density. This feature may indicate that the n_{eff} decreases with the increase of anodization current density in PS. These inferences are although correct, they are only qualitative in nature. A clear discussion on these aspects would be given in a later section

after the determination of n_{eff} and d of the PS films.

To exemplify the determination procedures of n_{eff} and d of these films, PS prepared on c-Si wafer of resistivity 0.001–0.005 Ω cm using 50 mA/cm^2 current density for 45 sec, whose specular reflectance is shown in Fig. 4.1(b), is considered as a representative. As a first step in the determination procedure, the interference pattern in the measured reflectance spectrum is fitted through Eq. (3.31) using an EMT. The goodness of the fit can be seen in Fig. 4.3. The EMT used to fit the interference pattern is Bruggeman's EMT with porosity and thickness as the fitting parameters obtained by trial and error method. At this stage of the analysis, mere resemblance of the interference pattern in the measured spectrum is sufficient. A perfect fit is not warranted.

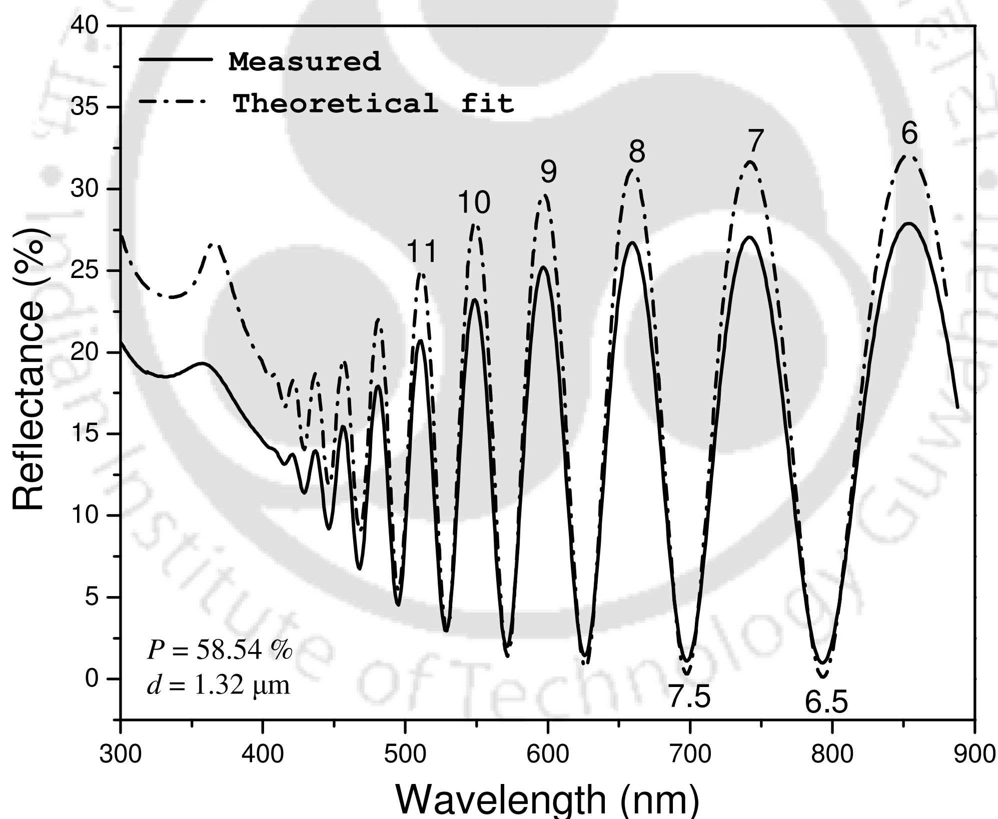

Figure 4.3 Theoretical fit to the interference pattern in the measured reflectance spectrum of PS prepared on 0.001–0.005 Ω cm resistivity c-Si wafer using 50 mA/cm^2 anodization current density for 45 sec. The theoretical fit is obtained through Eq. (3.31) using Bruggeman's EMT with porosity and thickness as the fitting parameters. The values of porosity and thickness used to fit the measured interference pattern are given at the inset. The interference orders that label the interference fringes have been determined through Eq. (3.11).

TH-1094_04612102

The fitting of the interference pattern over a broad spectral range, as in Fig. 4.3, ensures that the interference condition has completely been satisfied. Then, through Eq. (3.11), *m* for every fringe is determined for the simulated spectrum, and has been labelled as shown in Fig. 4.3. As the interference condition is satisfied by the simulated spectrum, *m* for every fringe in the simulated spectrum could also label the corresponding interference fringe in the measured spectrum. It is noteworthy that *n* and *d* that are used to fit the interference pattern are not the physical parameters of the real film.

Following the determination of *m* for the measured spectrum, the RHS of Eq. (3.11), i.e., the product of *m* and the corresponding wavelength, having been scaled down by a factor of 2, is plotted against the corresponding wavelength, and has been shown as ■ in Fig. 4.4. Through the LHS of Eq. (3.11), Fig. 4.4 could be identified as the dispersion of optical thickness, $d_{Op}(\lambda)$. The discrete data points (shown as ■) in Fig. 4.4 are experimental points, and have implicit measurement errors.

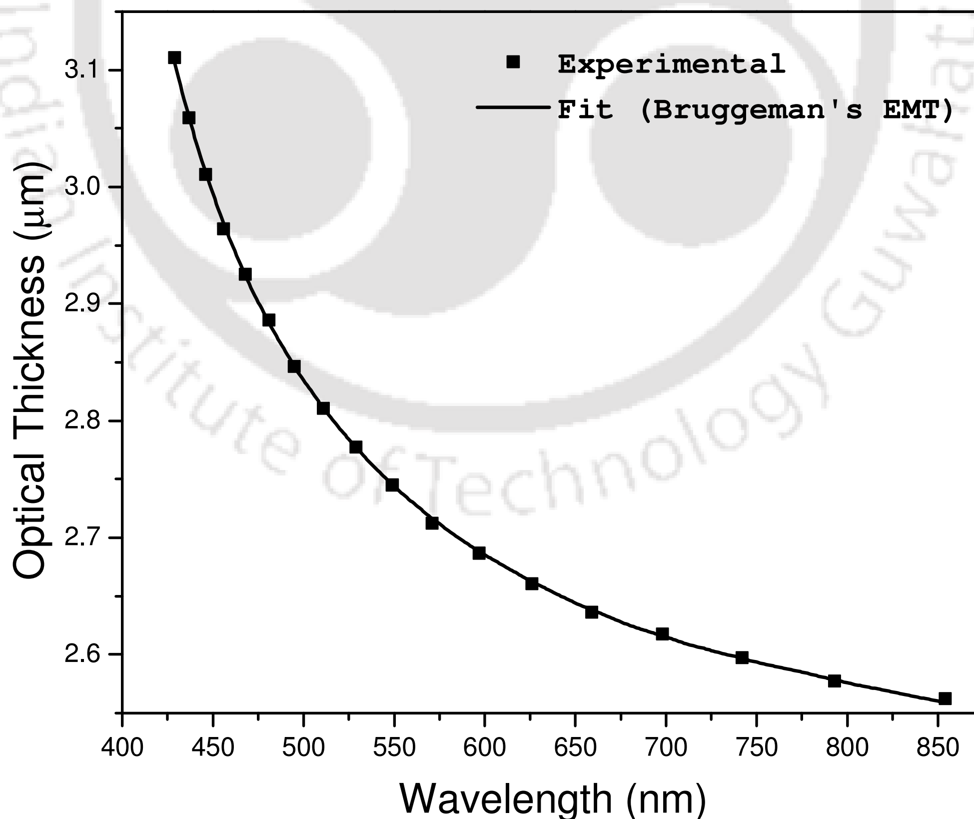

Figure 4.4 Measured and theoretically fitted $d_{Op}(\lambda)$ of PS prepared on c-Si wafer of resistivity 0.001–0.005 Ω cm using 50 mA/cm^2 current density for 45 sec.

To minimize the errors and to determine $d_{Op}(\lambda)$ for all intermediate values of λ, a curve fitting is performed through the LHS of Eq. (3.11). The fitting equation is given as

$$d_{Op} = d\,(n_{eff}^2 - \sin^2\theta)^{1/2} \tag{4.1}$$

where

$$n_{eff} = \left[\frac{-C + (C^2 + 8\,n_{Si}^2)^{1/2}}{4}\right]^{1/2} \tag{4.2a}$$

$$C = (1 - 2\,n_{Si}^2) - 3\,P\,(1 - n_{Si}^2) \tag{4.2b}$$

and P, n_{Si}, d and d_{Op} are porosity, real part of the refractive index of c-Si, physical thickness and optical thickness, respectively. The mathematical expression for n_{eff} as given by Eq. (4.2a) is from the Bruggeman's EMT. The fitting parameters of d_{Op} are again P and d. However, at this stage of the analysis, a good fit is desired. The fitting is done by Matlab using the command *fsolve* of optimization toolbox. The goodness of the fit to the discrete experimental points could be seen in Fig. 4.4.

With the above procedures, only the $d_{Op}(\lambda)$, which is roughly the product of $n(\lambda)$ and d, is determined with a minimal error; $n(\lambda)$ and d are still undetermined.

Determination of d requires specular reflectance measurements at two different angles of incidence. Figure 4.5 shows the measured specular reflectance spectra of the representative PS at 17.5° and 25° angles of incidence. The interference orders that label the interference fringes in Fig. 4.5 are obtained from *Method II* of Chapter 3 (Section 3.3.1.2). Let λ_3 (6638.16 cm^{-1}) and λ_1 (5533.65 cm^{-1}) of Fig. 4.5 denote λ_1 and λ_2 of *Method II* of Chapter 3, respectively. Substituting the values in Eq. (3.15), the interference order for λ_3 is estimated as 3.0036. As Eq. (3.15) overestimates the interference order, the actual interference order of λ_3 would be the nearest lower full integer, which is 3. If the interference order of λ_3 is 3, then the interference order of λ_1 and λ_2 would be 2.5.

Having determined the interference orders of λ_1, λ_2 and λ_3, the determination of d follows through the iterative procedure described in Chapter 3 (Section 3.3.2). The flow chart of the iteration has been shown in Chapter 3 in Fig. 3.5. The iteration for the determination of d is performed through a self-coded Matlab program with λ_1, λ_2 and λ_3, and their corresponding interference orders and angles of incidence as inputs. The summary of the iteration is shown in Table 4.1. The thickness d of the representative PS is found to be 1.3798 µm.

TH-1096_04612102

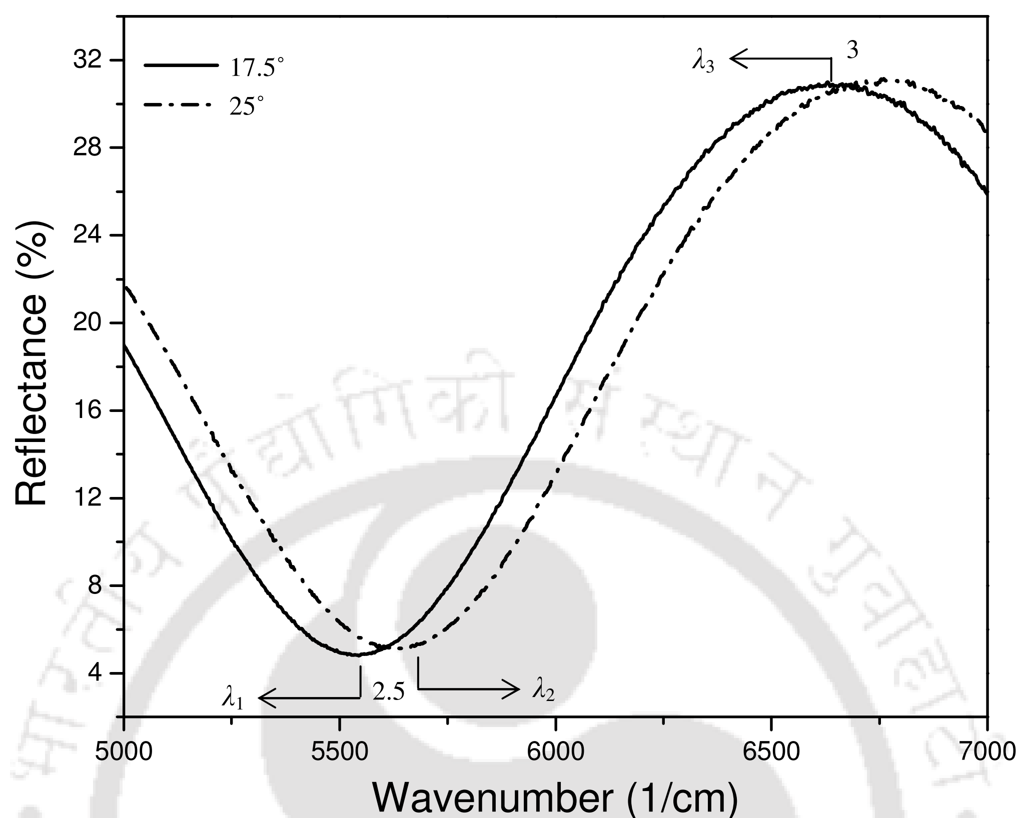

Figure 4.5 Measured FTIR specular reflectance spectra of PS prepared on c-Si wafer of resistivity 0.001–0.005 Ω cm using 50 mA/cm^2 current density for 45 sec at 17.5° and 25° angles of incidence in the spectral range 5000–7000 cm^{-1}. The interference pattern shifts with the change of angle of incidence. The interference fringes are labelled with the interference fringe order.

Table 4.1 Summary of the results of the iteration in the determination of d for PS prepared on c-Si wafer of resistivity 0.001–0.005 Ω cm using 50 mA/cm^2 current density for 45 sec.

Inputs			Outputs
Interference orders	Maxima/minima positions (cm^{-1})	Angle of incidence (°)	Resulting d after every iteration (μm)
2.5	λ_1 = 5533.65	17.5	d_0 = 1.3786 d_1 = 1.3798 d_2 = 1.3798
	λ_2 = 5626.83	25	
3	λ_3 = 6638.16	17.5	

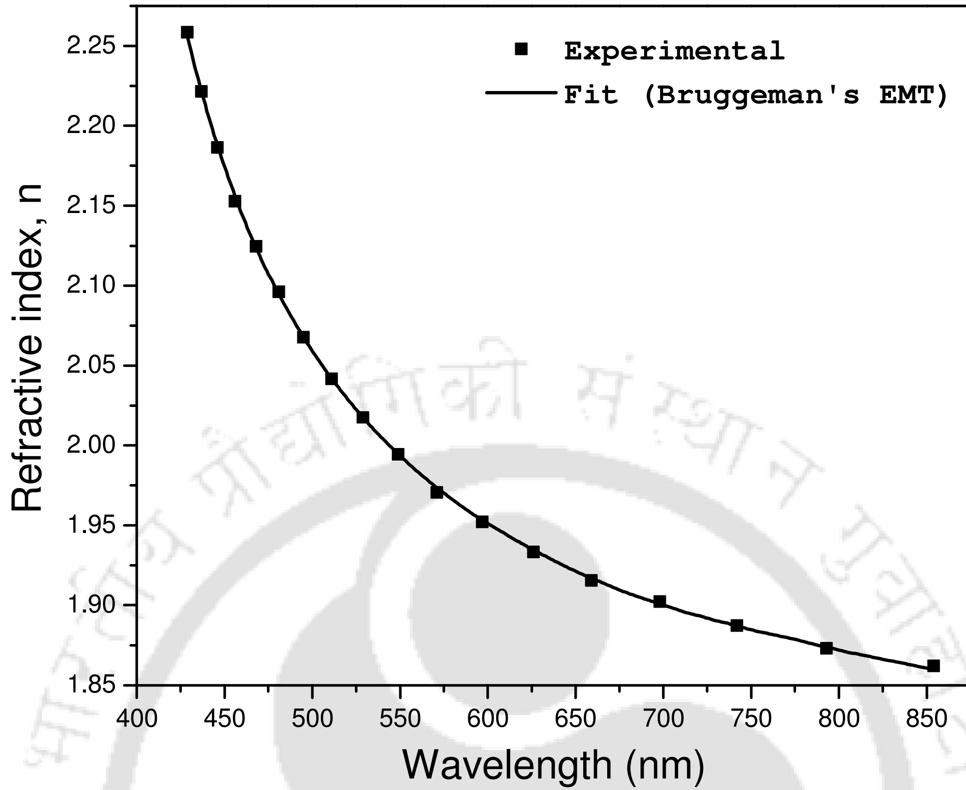

Figure 4.6 Measured and theoretically fitted dispersion of effective refractive index $n_{eff}(\lambda)$ of PS prepared on c-Si wafer of resistivity 0.001–0.005 Ω cm using 50 mA/cm^2 current density for 45 sec.

Following the determination of d, the theoretically fitted data points of d_{Op} are considered for the determination of $n_{eff}(\lambda)$ through the relation

$$n_{eff} = \left[\frac{d_{Op}^{\ 2}}{4\,d^2} + \sin^2\theta\right]^{1/2} \qquad (4.3)$$

The $n_{eff}(\lambda)$ as obtained through the measurement and the fit are shown in Fig. 4.6.

Similar procedures have been followed for the determination of d and $n_{eff}(\lambda)$ of all PS prepared on c-Si wafers of resistivities 0.001–0.005 and 0.01–0.05 Ω cm. Table 4.2 summarizes d and growth rate of PS prepared on c-Si wafers of resistivities 0.001–0.005 and 0.01–0.05 Ω cm under the variations of anodization current density and time. The effects of B-doping concentration and anodization current density on $n_{eff}(\lambda)$ on these high B-doping concentration wafers are shown in Fig. 4.7.

TH-1098_04612102

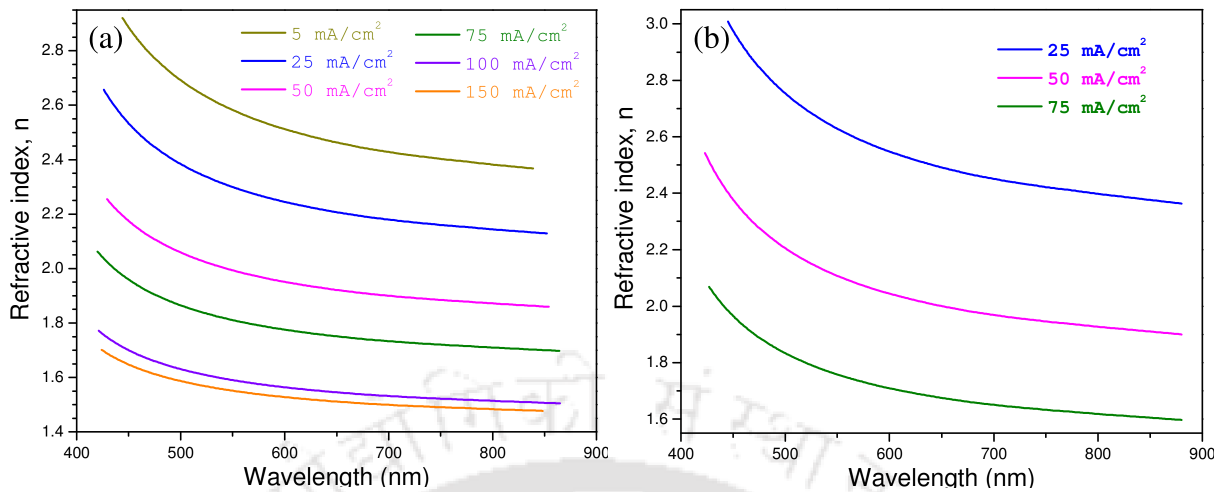

Figure 4.7 Dispersion of effective refractive index $n_{eff}(\lambda)$ of PS prepared under various anodization current densities on c-Si wafers of resistivities (a) 0.001–0.005 Ω cm and (b) 0.01–0.05 Ω cm.

Table 4.2 Summary of thickness and growth rate of PS prepared on c-Si wafers of resistivities 0.001–0.005 and 0.01–0.05 Ω cm under various anodization current densities for various times.

Resistivity (Ω cm)	Anodization current density (mA/cm^2)	Anodization time (min)	Thickness (µm)	Growth rate (nm/s)
0.001–0.005	05	3.00	0.7981	4.4
	25	1.00	1.0029	16.7
		1.50	1.5432	17.1
		2.00	2.0566	17.1
	50	0.75	1.3798	30.7
		1.00	1.8188	30.3
		1.50	2.8837	32.0
	75	0.50	1.2747	42.5
		0.75	1.9608	43.6
		1.00	2.6305	43.8

Resistivity (Ω cm)	Anodization current density (mA/cm^2)	Anodization time (min)	Thickness (μm)	Growth rate (nm/s)
0.001–0.005	100	0.75	2.4499	54.4
	150	0.50	2.3024	76.7
0.01–0.05	25	0.50	0.8305	27.7
	50	0.25	0.7656	51.0
	75	0.20	0.8283	69.0

4.1.2 Low B-doping concentration wafers (0.1–0.5, 1–10 and >50 Ω cm)

Figures 4.8, 4.9 and 4.10 show the measured specular reflectance spectra of PS prepared on low B-doping concentration c-Si wafers of resistivities 0.1–0.5, 1–10 and >50 Ω cm, respectively. The specular reflectance spectra in Figs. 4.8 and 4.9 are measured at 8° angle of incidence and the spectra in Fig. 4.10 are measured at 45° angle of incidence. The anodization current densities used for the preparation of these PS are 25, 50 and 75 mA/cm^2. All the spectra show multiple beam interference patterns similar to that of the specular reflectance spectra of PS prepared on high B-doping concentration wafers shown in Figs. 4.1 and 4.2. The interference patterns in Figs. 4.8 and 4.9 fade with the decrease of

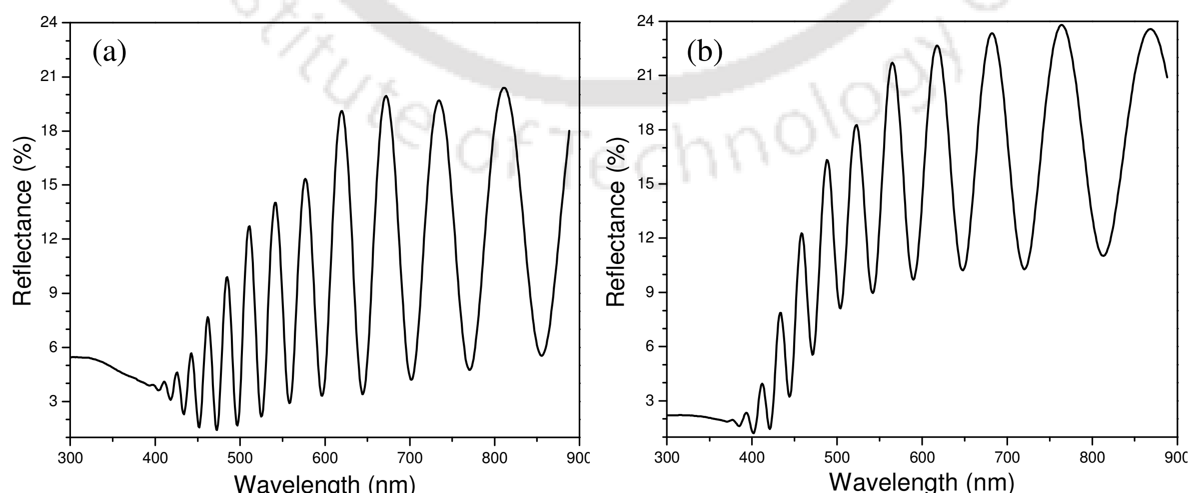

Figure 4.8 Measured specular reflectance of PS prepared on 0.1–0.5 Ω cm c-Si wafer using (a) 25 mA/cm^2 current density for 2 min and (b) 75 mA/cm^2 current density for 45 sec.

TH-1090_04612102

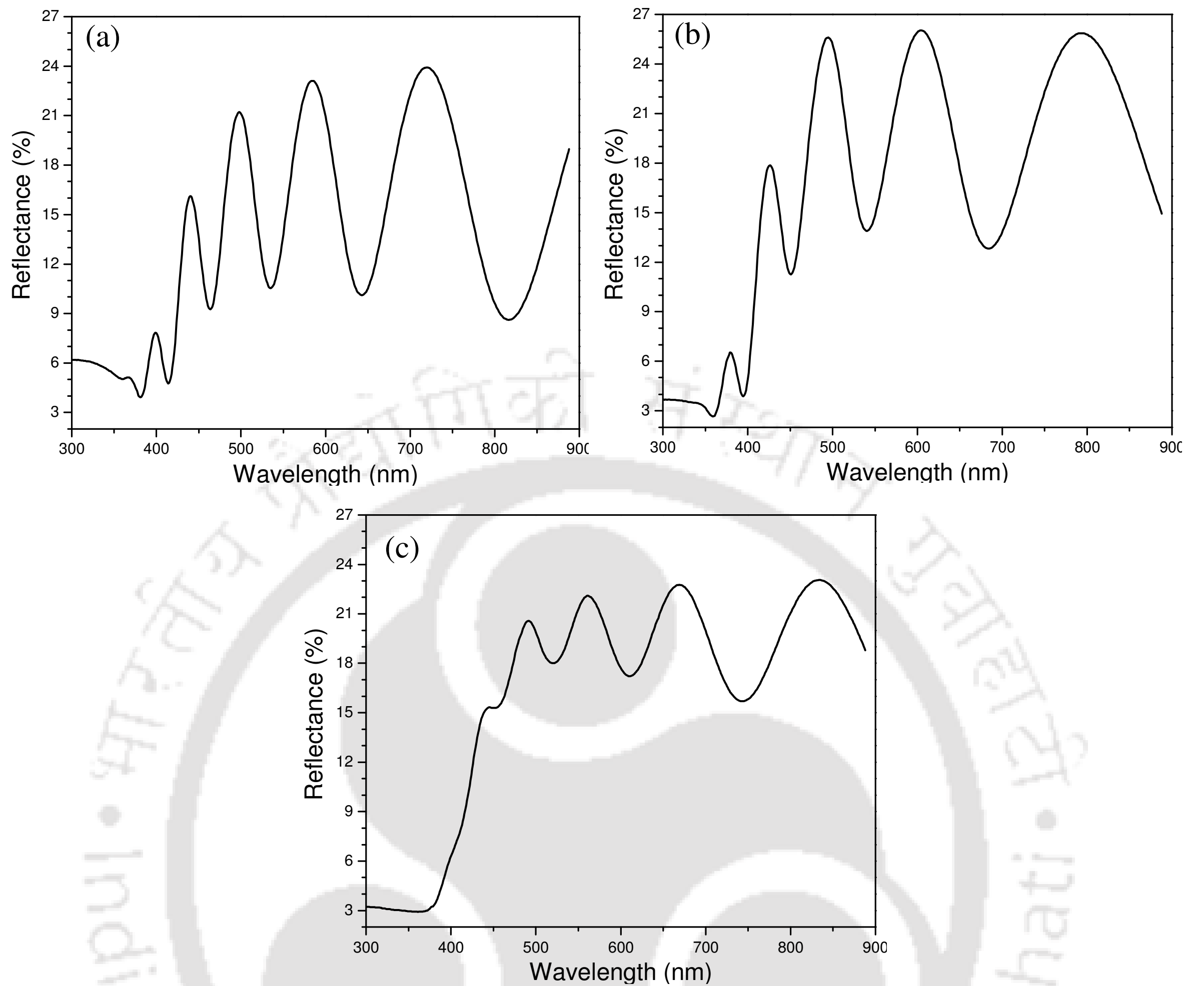

Figure 4.9 Measured specular reflectance of PS prepared on c-Si wafers of resistivity 1–10 Ω cm using (d) 25 mA/cm^2 current density for 1.5 min (e) 50 mA/cm^2 current density for 45 sec (f) 75 mA/cm^2 anodization current density for 45 sec.

wavelength, and completely disappear for shorter wavelengths. Also, the interference free reflectance in Figs. 4.8 and 4.9 decreases with the increase of anodization current density. These spectral features are very similar to the spectral features of PS prepared on high B-doping concentration wafers shown in Figs. 4.1 and 4.2. However, in Fig. 4.10, which shows the reflectance spectra of PS prepared on c-Si wafers of resistivity >50 Ω cm, the interference patterns show no signature of fading with the decrease of wavelength, and retain even for shorter wavelengths.

The spectral features of these PS are although nearly as same as that of the PS prepared on high B-doping concentration wafers, the measured interference patterns in these PS

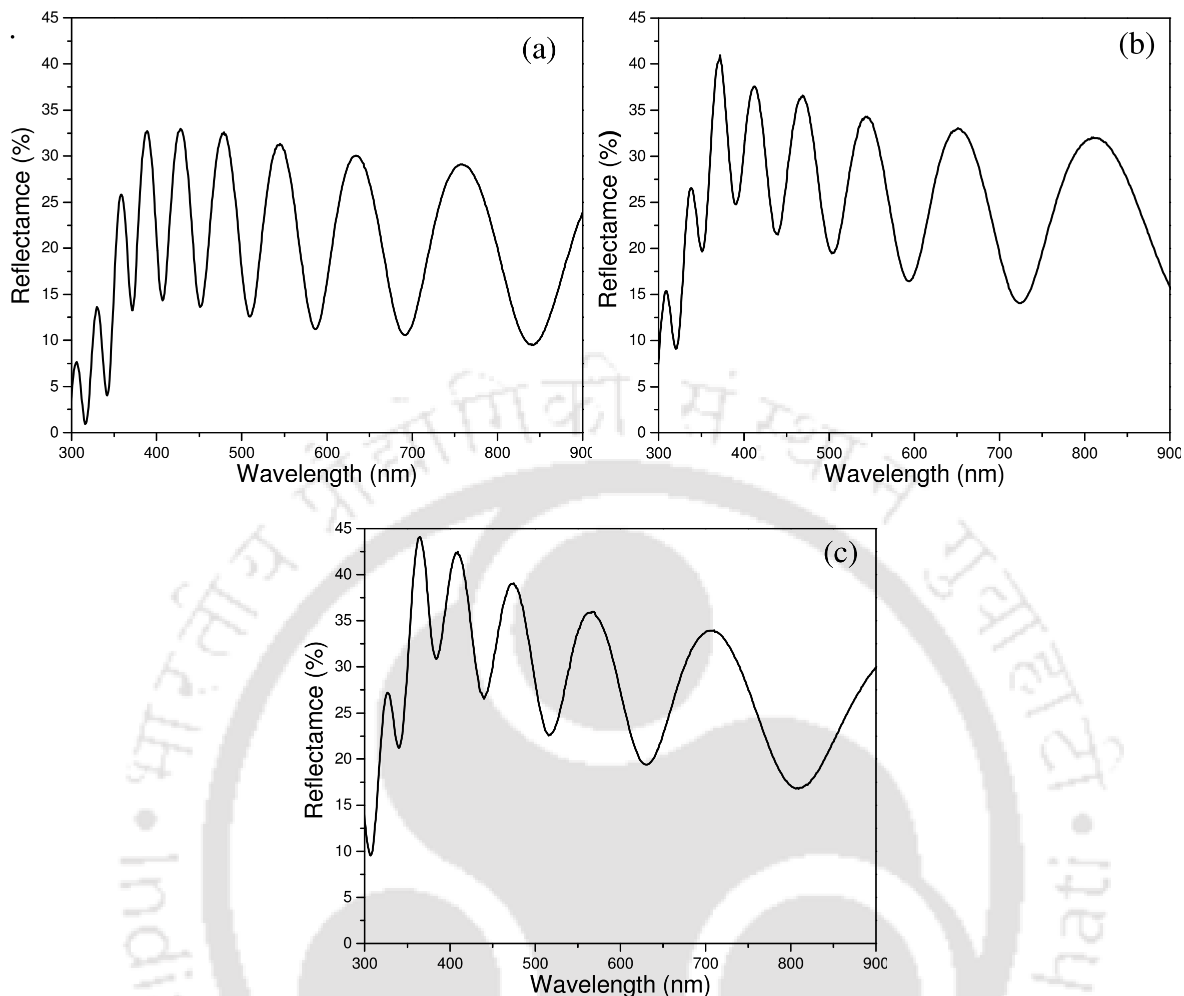

Figure 4.10 Measured specular reflectance of PS prepared on >50 Ω cm c-Si wafer using (a) 25 mA/cm^2 current density for 1.5 min (b) 50 mA/cm^2 current density for 45 sec (c) 75 mA/cm^2 current density for 30 sec.

could not be fitted with EMTs. An attempt to fit the measured interference pattern is shown in Fig. 4.11 to the specular reflectance of PS prepared on c-Si wafer of resistivity 0.1–0.5 Ω cm using 25 mA/cm^2 anodization current density for 2 min. The simulated spectrum could not be able to make a good fit to the measured interference pattern. This is not only the case of PS under consideration, but for all PS prepared on low B-doping concentration c-Si wafers (0.1–0.5, 1–10 and >50 Ω cm).

Due to the non-fitting of the measured interference pattern, the determination procedures of n_{eff} and d would be slightly different from the determination procedures of these parameters in PS prepared on high B-doping concentration wafers. To exemplify the

TH-1092_04612102

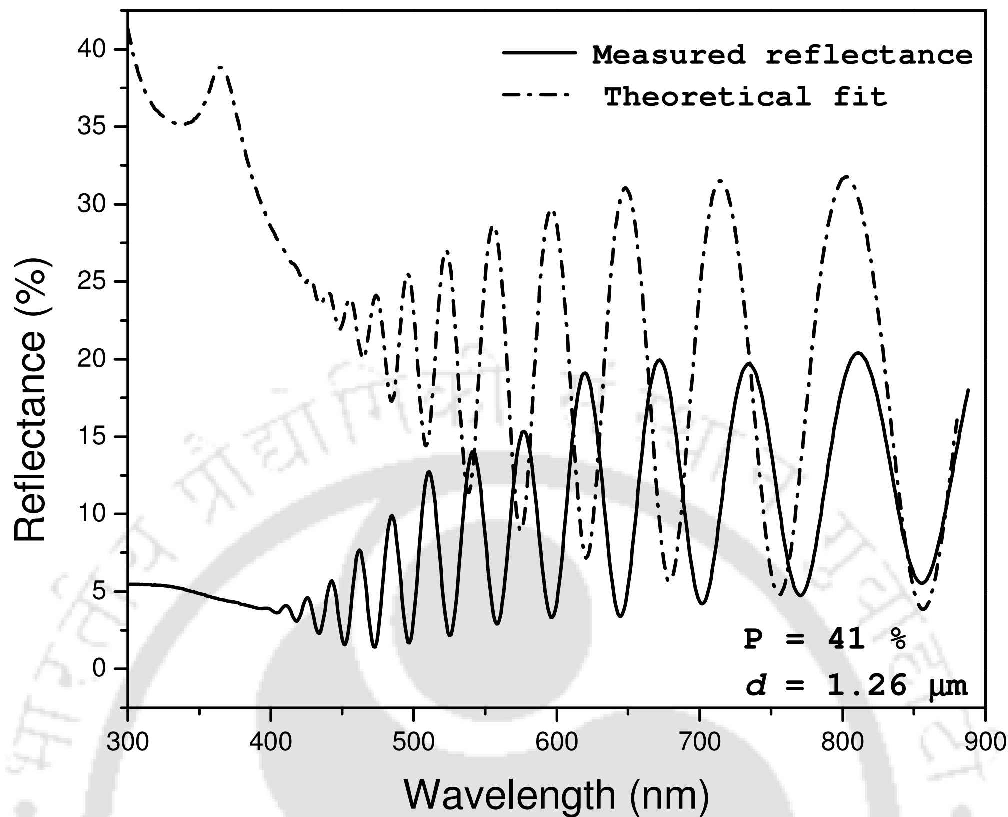

Figure 4.11 Theoretical fit to the interference pattern in the measured reflectance spectrum of PS prepared on 0.1–0.5 Ω cm resistivity c-Si wafer using 25 mA/cm^2 current density for 2 min. The theoretical fit is obtained through Eq. (3.31) using Bruggeman's EMT with porosity and thickness as the fitting parameters. The values of porosity and thickness used to fit the measured interference pattern are given at the inset.

determination procedures of n_{eff} and d of these films, PS prepared on c-Si wafer of resistivity 0.1–0.5 Ω cm using 25 mA/cm^2 current density for 2 min, whose specular reflectance is shown in Fig. 4.8(a), is considered as a representative.

As a first step in the determination of n_{eff} and d, the interference fringe order is determined for every interference fringe in the specular reflectance similar to the case of PS prepared on high B-doping concentration wafers. However, in the present case, the procedure for determination is *Method II* of Chapter 3 (Section 3.3.1.2) rather than through the simulation of interference pattern. The procedure necessitates considering two adjacent interference fringes in the specular reflectance of the material. It would be better if the two adjacent interference fringes are in the optically thin region of the spectrum, i.e., in the

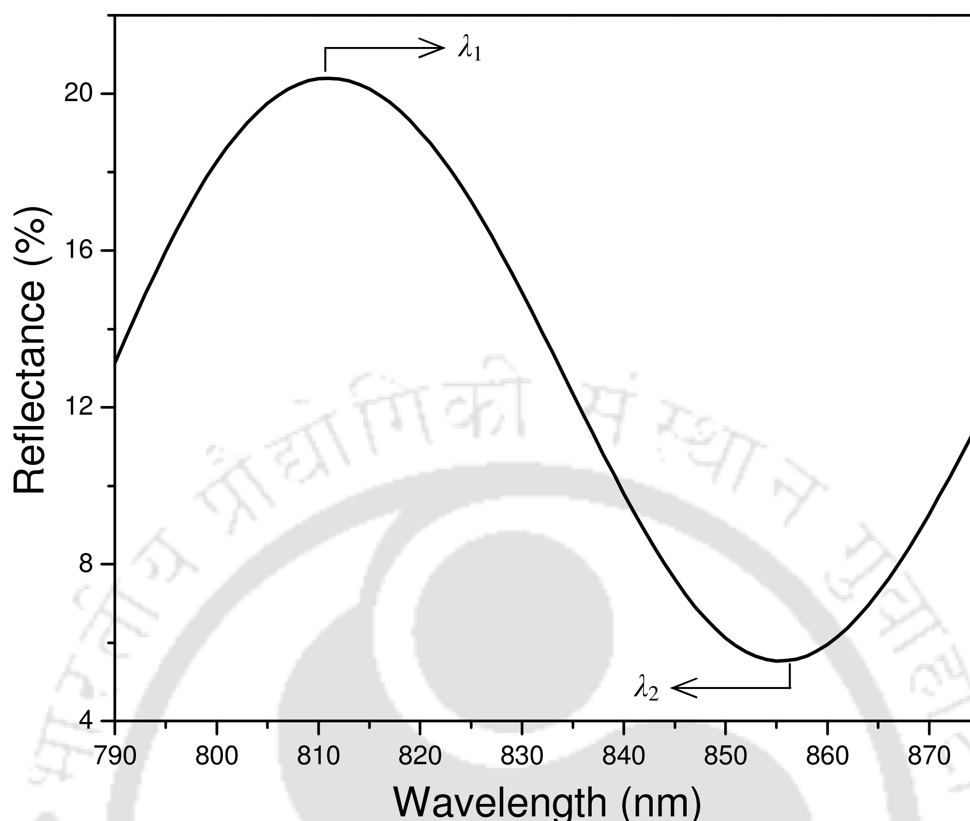

Figure 4.12 A closer view of the extreme interference fringes towards optically thin region in the measured specular reflectance of PS prepared on c-Si wafer of resistivity 0.1-0.5 Ω cm under 25 mA/cm^2 current density for 2 min. The spectral positions are marked for the purpose of the determination of interference orders.

longer wavelength region. A closer view of the interference fringes that are considered for the determination of interference orders is shown in Fig. 4.12. The wavelength positions of the interference fringes are denoted as λ_1 (811 nm) and λ_2 (855 nm). Let Ξ_0 be the interference fringe order at λ_1. Substituting the values of λ_1 and λ_2 in Eq. (3.15), Ξ_0 is estimated to be ~9.7. As it has already been mentioned in Section 3.3.1.2 that Eq. (3.15) overestimates the interference fringe order, the actual interference fringe order at λ_1 would be the nearest lower full integer, i.e., 9.

Once the interference fringe order for a particular interference fringe is obtained, the interference fringe orders of the entire interference pattern could readily be obtained as the neighbouring interference fringe orders differ only by 0.5. With that conception, the interference orders for the remaining interference fringes are obtained. In Fig. 4.13, the

TH-1094_04612102

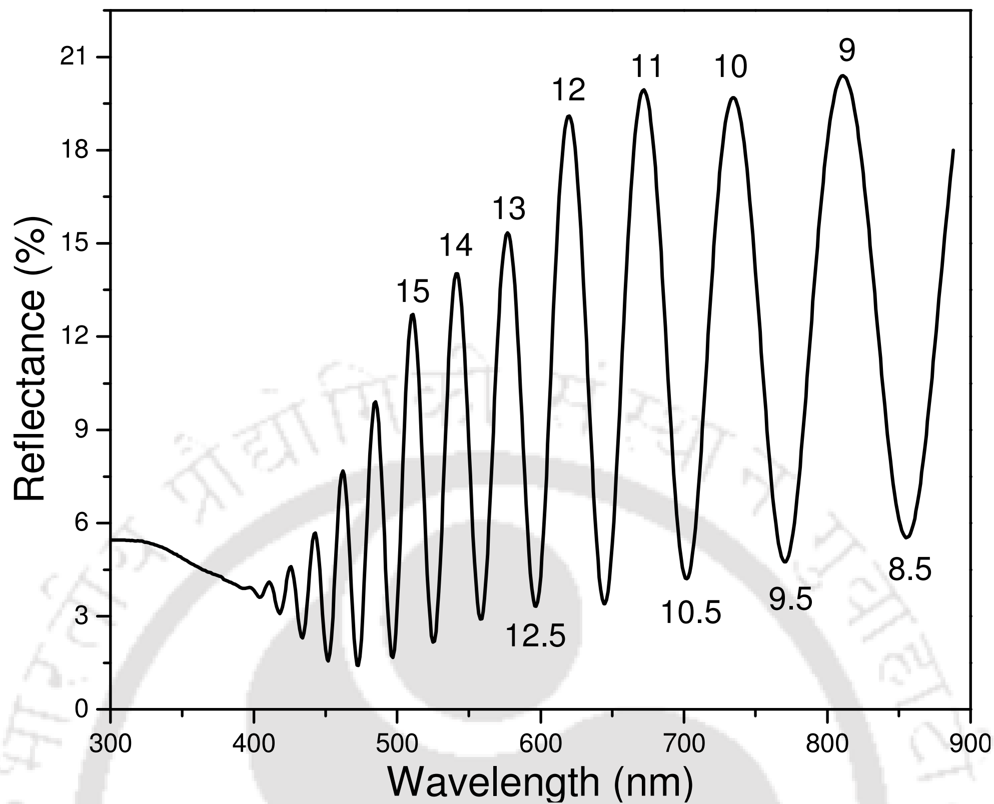

Figure 4.13 The interference fringe orders of the interference fringes in the measured specular reflectance of PS prepared on c-Si wafer of resistivity 0.1-0.5 Ω cm using 25 mA/cm^2 current density for 2 min. The interference orders are obtained from the conception that the interference orders of the neighbouring interference fringes differ only by 0.5.

interference orders as obtained by this procedure are shown by labelling the corresponding interference fringes in the reflectance spectrum of the representative PS.

The interference fringe order as obtained through *Method II* of Chapter 3 could sometimes be erroneous. The sources of error are the overestimation of the interference fringe order by Eq. (3.15) and the rounding off to the nearest lower full or half-integer depending on the interference condition for the system under consideration. Choosing the optically thin region of the spectrum is one possibility to avoid the erroneous estimate. However, it may not always be possible to record the spectrum until optically thin region for every film due to the practical limitations arising from the finite spectral range of commercial spectrometers. In the following, a procedure to check and to correct (if at all) for the error in the determination of interference order is presented.

It is from practical experience that in weak and medium absorption and in transparent regions of the spectrum, $n(\lambda)$ has normal dispersion. As the investigations in this chapter are also limited to those spectral regions, $n_{eff}(\lambda)$ of PS is expected to have normal dispersion. From the LHS of Eq. (3.11), it is evident that the functional form of $d_{Op}(\lambda)$ is same as that of $n(\lambda)$. So, $d_{Op}(\lambda)$ as obtained from the RHS of Eq. (3.11) i.e., the product of interference fringe order and the corresponding wavelength, would show the normal dispersion when the determined interference order is correct. Figure 4.14 shows the $d_{Op}(\lambda)$ through RHS of Eq. (3.11) for three different values of interference orders: with and without modifications in the determined interference orders. The dispersion of d_{Op} is very sensitive to the changes in the interference orders, which could be inferred from Fig. 4.14. For the

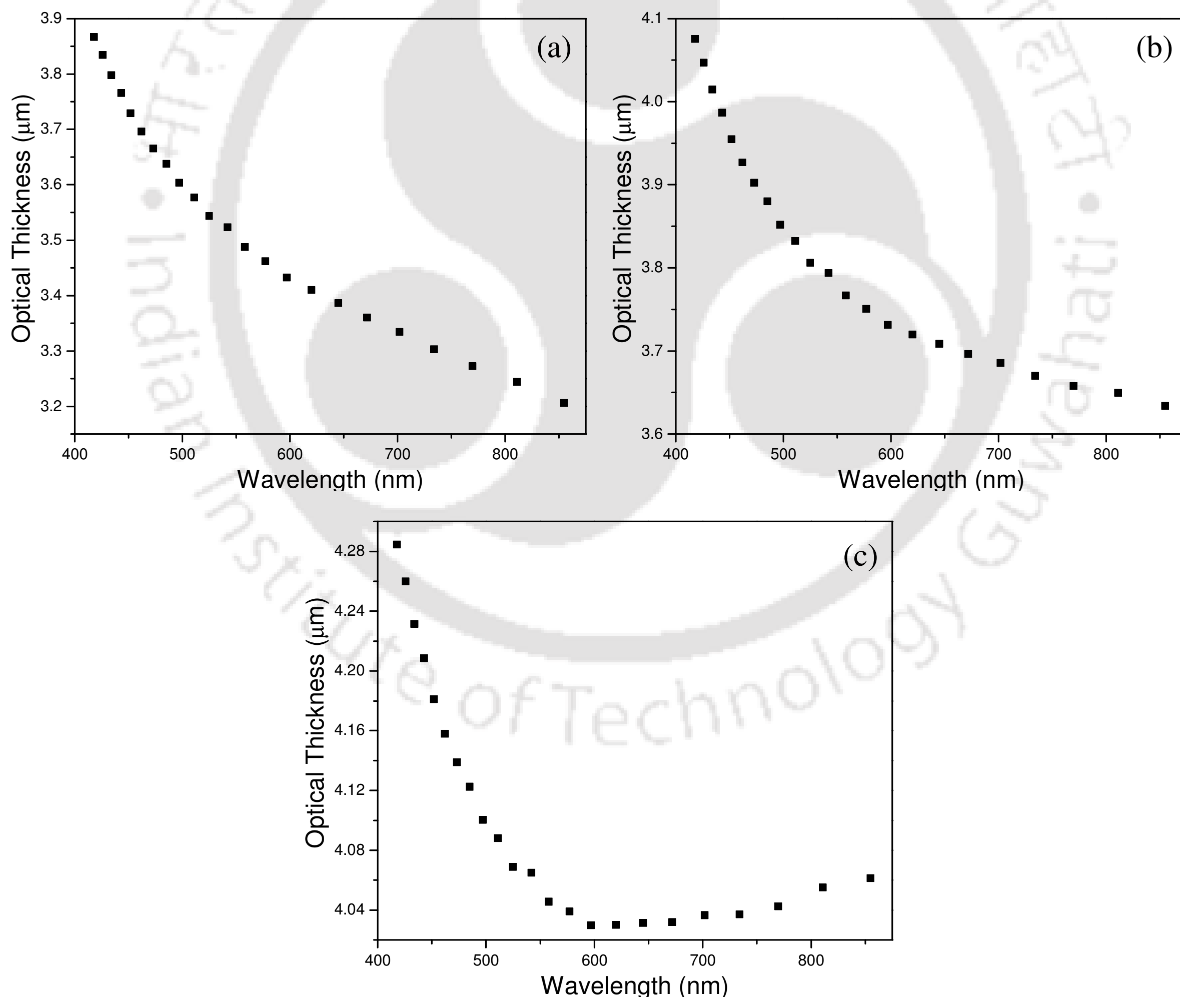

TH-1096_04612102

Figure 4.14 Dispersion of optical thickness $d_{Op}(\lambda)$ through the RHS of Eq. (3.11) with (a) one order lowered from the determined interference orders (b) no change in the determined interference orders and (c) one order raised from the determined interference orders.

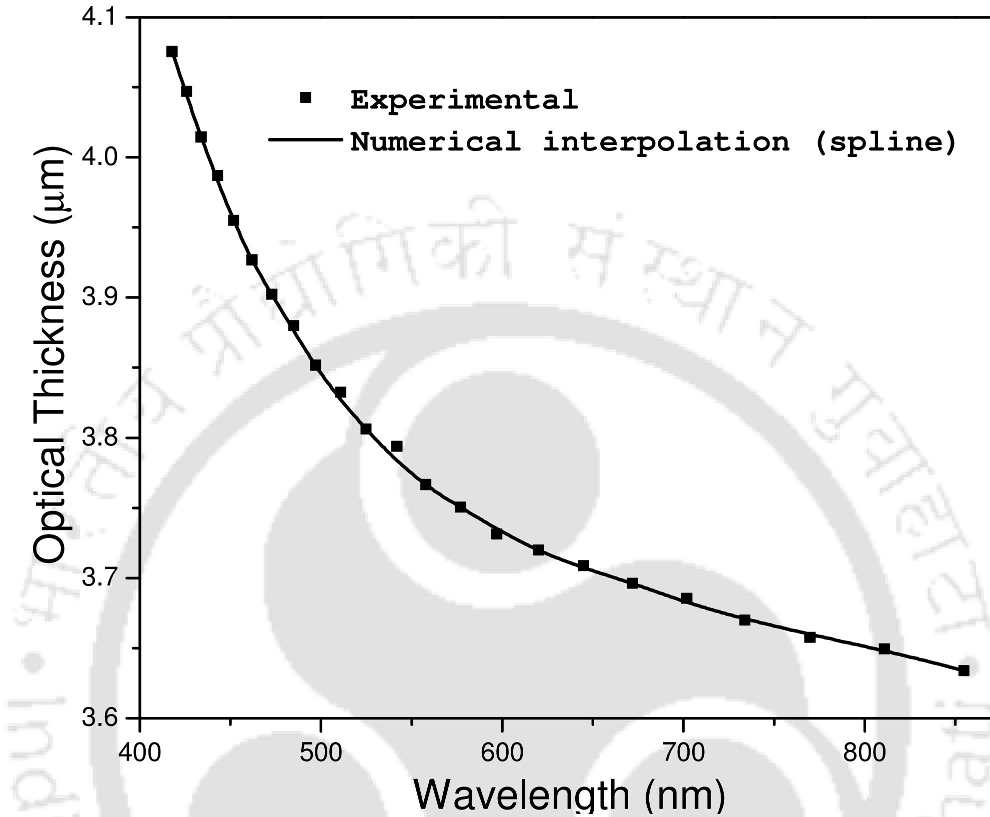

Figure 4.15 Experimentally determined and spline interpolated optical thickness dispersion $d_{Op}(\lambda)$ of PS prepared on c-Si wafer of resistivity 0.1–0.5 Ω cm using 25 mA/cm^2 current density for 2 min.

present case, the $d_{Op}(\lambda)$ as obtained with no change in the determined interference orders produces normal dispersion as can be seen in Fig. 4.14(b). So, the interference orders as determined are correct for the present case. The correctness of the determined interference order is checked by this procedure. If the $d_{Op}(\lambda)$ as obtained from the determined value of interference order has not shown the normal dispersion, then those values of m would have been discarded. In that case, the other values of m for which $d_{Op}(\lambda)$ shows normal dispersion would have been considered.

Experimentally, $d_{Op}(\lambda)$ is obtainable only at discrete values of λ. To determine the $d_{Op}(\lambda)$ for all intermediate values of λ, numerical interpolation (spline interpolation) is

performed. Figure 4.15 shows the spline interpolation for the discrete experimental $d_{\mathrm{Op}}(\lambda)$. The interpolation technique, in addition to provide the intermediate values of $d_{\mathrm{Op}}(\lambda)$, minimizes the error in the experimentally determined $d_{\mathrm{Op}}(\lambda)$.

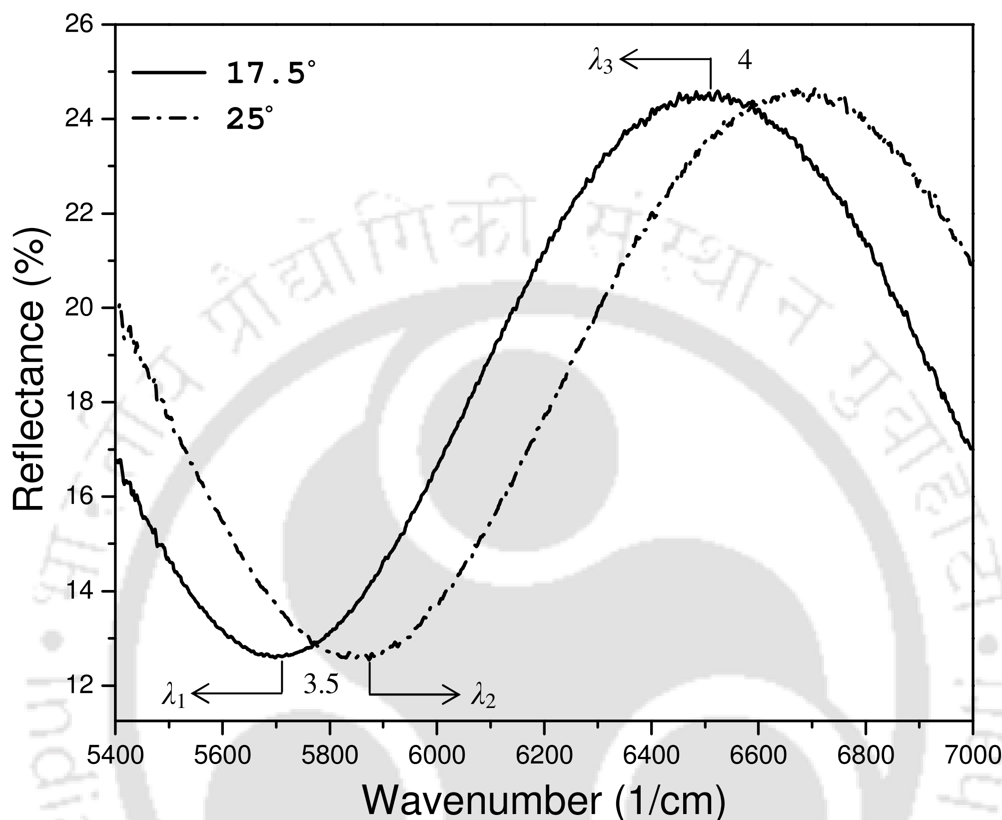

Figure 4.16 Measured FTIR specular reflectance spectra of PS prepared on c-Si wafer of resistivity 0.1–0.5 Ω cm using 25 mA/cm^2 current density for 2 min at 17.5° and 25° angles of incidence in the spectral range 5400–7000 cm^{-1}. The interference pattern shifts with the change of angle of incidence. The interference fringes are labelled with the interference fringe orders determined through *Method II* of Chapter 3.

Inputs			Outputs
Interference orders	Maxima/minima positions (cm^{-1})	Angle of incidence (°)	Resulting d after every iteration (μm)
3.5	λ_1 = 5706.74	17.5	d_0 = 2.2488 d_1 = 2.2718 d_2 = 2.2713
	λ_2 = 5847.07	25	
4	λ_3 = 6504.39	17.5	

TH-1098_04612102

Table 4.3 Summary of the results of the iteration in the determination of d for PS prepared on 0.1–0.5 Ω cm resistivity c-Si wafer using 25 mA/cm^2 current density for 2 min.

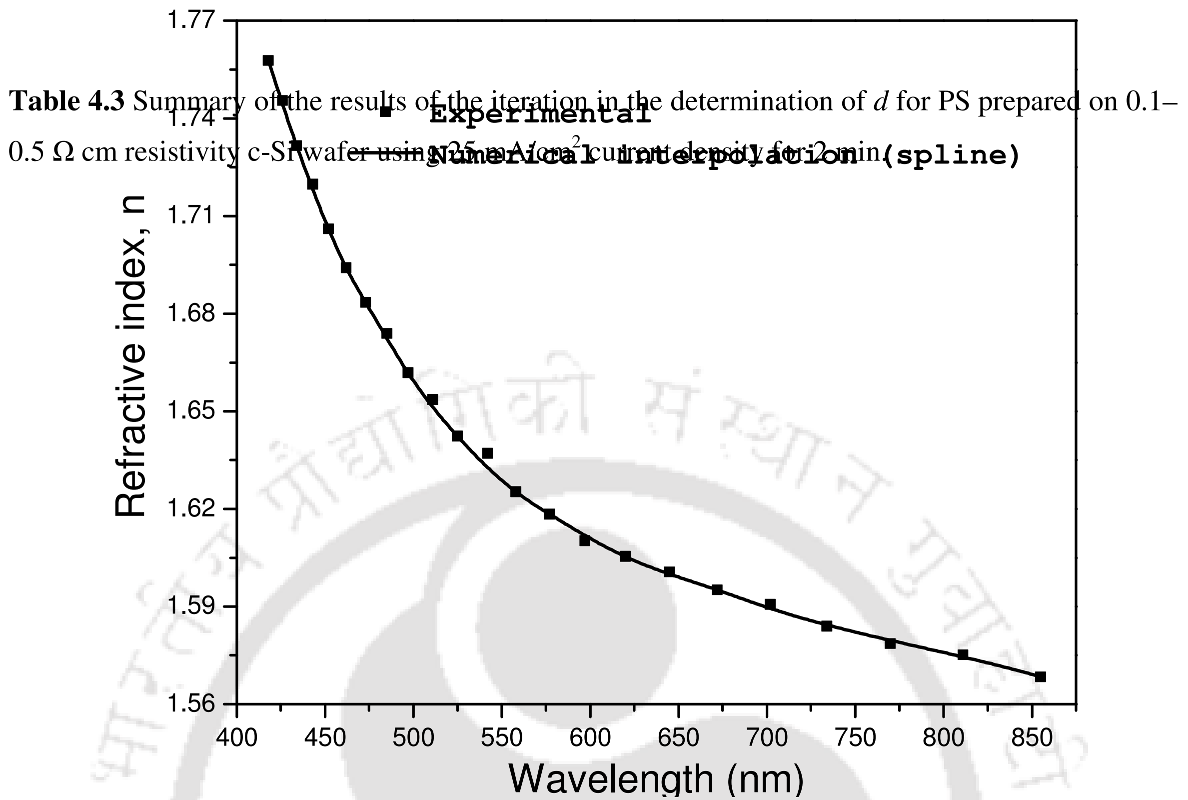

Figure 4.17 Experimentally determined and spline interpolated effective refractive index dispersion $n_{\rm eff}(\lambda)$ of PS prepared on c-Si wafer of resistivity 0.1–0.5 Ω cm using 25 mA/cm^2 current density for 2 min.

Determination procedures of d and $n_{\rm eff}(\lambda)$ are same as discussed for PS prepared on high B-doping concentration wafers. However, for the sake of completion, the determination procedures have been discussed also here. Figure 4.16 shows the measured specular reflectance spectra of PS at 17.5° and 25° angles of incidence. The interference orders that label the interference fringes in Fig. 4.16 are obtained from *Method II* of Chapter 3. Then, the determination of d follows through the iterative procedure. The summary of the iteration with inputs and outputs is shown in Table 4.3.

With the determination of d, the spline interpolated data of $d_{\rm Op}$, shown in Fig. 4.15, have been used in Eq. (4.3) for the determination of $n_{\rm eff}(\lambda)$. Figure 4.17 shows both the

experimentally determined (discrete) and spline interpolated (continuous) $n_{eff}(\lambda)$ of PS prepared on c-Si wafer of resistivity 0.1–0.5 Ω cm using 25 mA/cm^2 current density for 2 min.

Similar procedures have been followed for the determination of d and $n_{eff}(\lambda)$ of all PS prepared on c-Si wafers of resistivities 0.1–0.5, 1–10 and >50 Ω cm. Table 4.4 summarizes d and growth rate of PS prepared on c-Si wafers of resistivities 0.1–0.5, 1–10 and >50 Ω cm under the variations of anodization current density and time. The effects of B-doping concentration and anodization current density on $n_{eff}(\lambda)$ on these low B-doping concentration wafers are shown in Fig. 4.18.

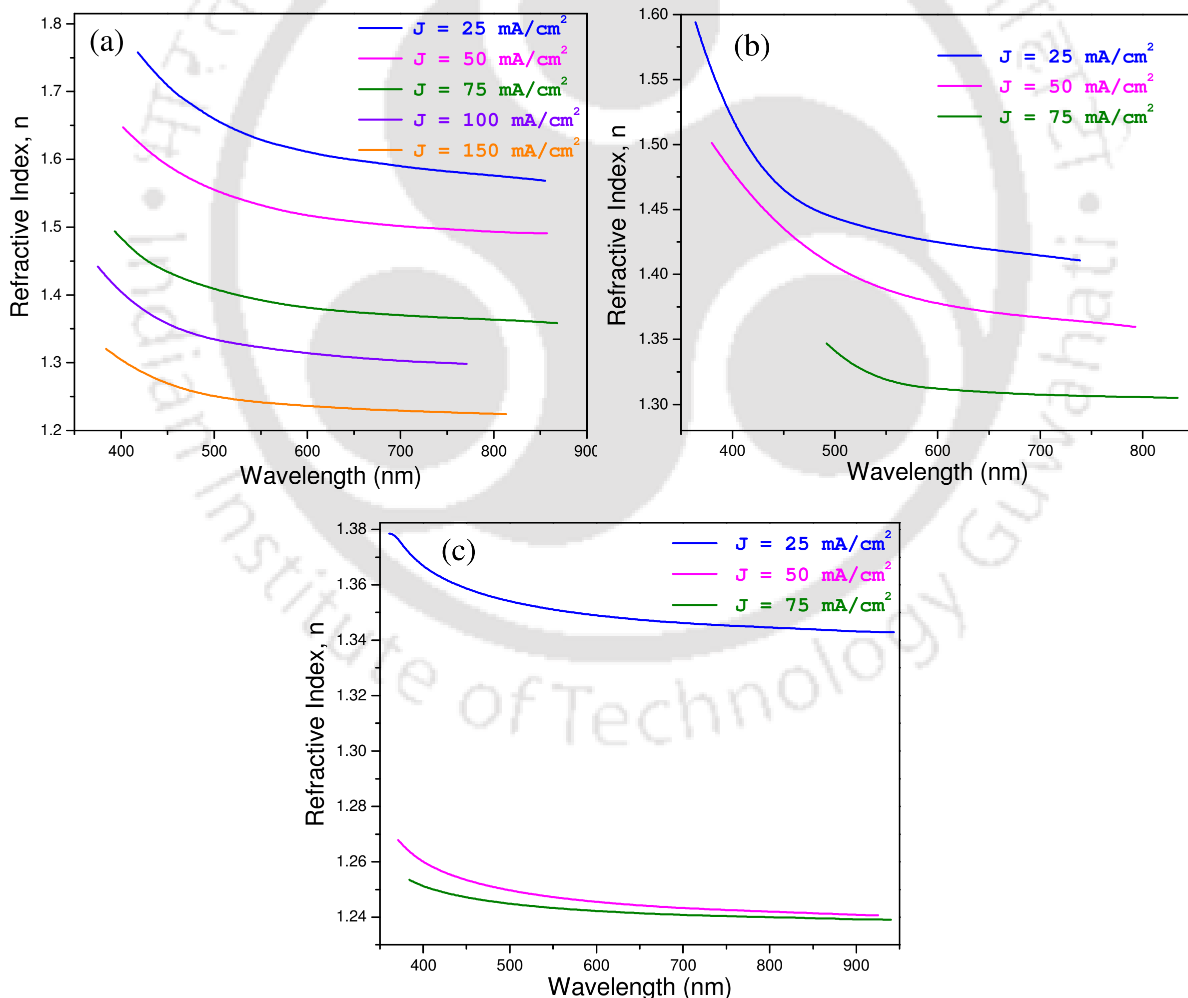

TH-1090_04612102

Figure 4.18 Dispersion of effective refractive index $n_{eff}(\lambda)$ of PS prepared under various anodization current densities on c-Si wafer of resistivities (a) 0.1-0.5 Ω cm (b) 1-10 Ω cm and (c) > 50 Ω cm.

Resistivity (Ω cm)	Anodization current density (mA/cm^2)	Anodization time (min)	Thickness (μm)	Growth rate (nm/s)
0.1–0.5	25	1.00	1.1785	19.6
		1.50	1.8344	20.4
		2.00	2.2713	18.9
	50	1.00	2.1254	35.4
		0.50	0.9837	32.8
		0.75	1.5991	35.5
	75	0.75	2.1699	48.2
		0.50	1.4861	49.5
		0.25	0.7327	48.8
	100	0.25	1.0452	69.7
	150	0.20	1.1699	97.5
1–10	25	1.50	1.0235	11.4
	50	1.00	1.2353	20.6
	75	0.75	1.2854	28.6
>50	25	1.50	1.6554	18.4
	50	0.75	1.5898	35.3
	75	0.50	1.3899	46.3

Table 4.4 Thickness and growth rate of PS prepared on c-Si wafers of resistivities 0.1–0.5, 1–10 and >50 Ω cm under various anodization current densities for various times.

TH-1099_04612102

4.2 EFFECTS OF ANODIZATION CONDITIONS ON GROWTH RATE AND EFFECTIVE REFRACTIVE INDEX OF PS

So far in this chapter, the effective refractive index n_{eff}, thickness d and growth rate of PS prepared under many different anodization conditions have been determined. In the following, the effects of anodization conditions on the growth rate and n_{eff} are discussed and provide details of the formation kinetics and microstructure of PS.

4.2.1 Effects of anodization time on growth rate and effective refractive index of PS

Growth rate and refractive index of PS have not shown significant dependence on the anodization time as shown in Table 4.5 for PS prepared on 0.001-0.005 Ω cm resistivity c-Si wafer. This signifies that the formation kinetics of PS is unaffected during the course of the anodization process and the microstructure of PS is same throughout the material. Any change in formation kinetics and microstructure of PS would clearly have affected the growth rate and refractive index of PS, respectively.

Table 4.5 Summary of growth rate and effective refractive index of PS prepared on c-Si wafers of resistivity 0.001-0.005 Ω cm using 25, 50 and 75 mA/cm^2 anodization current densities for various times.

Anodization current density (mA/cm^2)	Anodization time (min)	Growth rate (nm/s)	Effective refractive index n_{eff} at 700 nm
25	1.00	16.7	2.1799
	1.50	17.1	2.1791
	2.00	17.1	2.1793
50	0.75	30.7	1.9002
	1.00	30.3	1.8997
	1.50	32.0	1.8997
75	0.50	42.5	1.7334
	0.75	43.6	1.7324
	1.00	43.8	1.7335

TH-1090_04612102

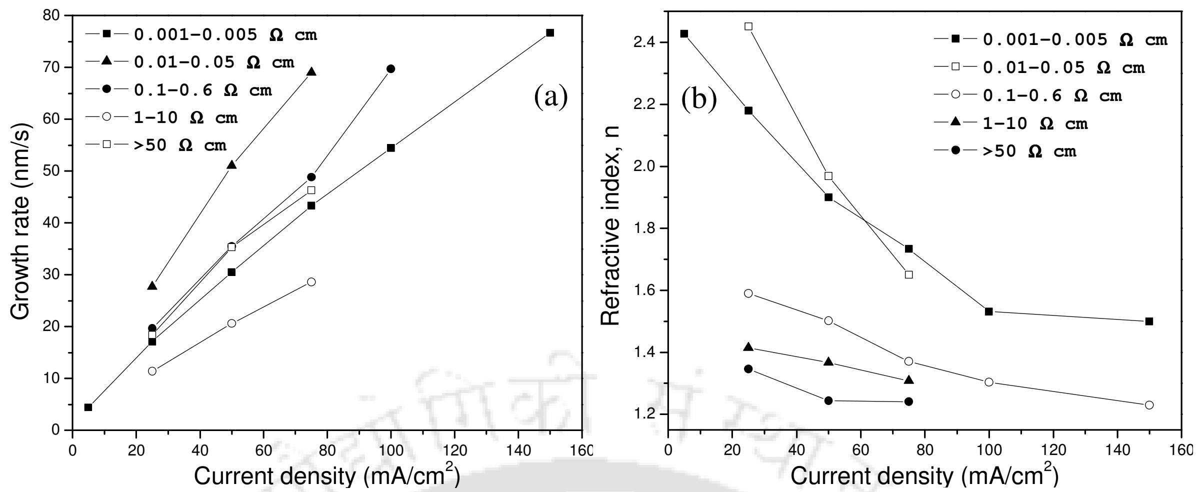

Figure 4.19 Effect of anodization current density on (a) growth rate and (b) effective refractive index of PS prepared on various c-Si wafer resistivities.

4.2.2 Effects of anodization current density on growth rate and effective refractive index of PS

Figure 4.19(a) shows the variation of growth rate with anodization current density for PS prepared on many different c-Si wafer resistivities. With increasing anodization current density, the growth rate increases, and is nearly linear for all resistivities at least in the range of attainable anodization current density values. On the other hand, n_{eff} of PS decreases with the increasing anodization current density as shown in Fig. 4.19(b). For relatively small anodization current densities, the decreasing n_{eff} is nearly linear. However, as the anodization current density increases to higher values, the decrease in n_{eff} tends to saturate.

Based on these observations, the following inferences on the formation kinetics and microstructure of PS are made: (i) anodization current density affects both the formation kinetics and the microstructure of PS (ii) formation kinetics of PS is constantly being changed for all anodization current densities (iii) relative changes in the microstructure of PS are significant only at low anodization current densities (iv) at higher anodization current densities, the relative changes in the microstructure of PS are minimal.

The effect of anodization current density being different for the formation kinetics and the microstructure of PS is intriguing. Anodization current density has a direct effect only

on the formation kinetics of PS, as the transport of the carriers (holes and F^- ions) is governed by the anodization current density. The effect on the microstructure is merely a consequence of the effect of anodization current density on the formation kinetics of PS.

In the formation of PS, hole transport is vital. Anodization current density affects both the velocity and the density of holes that involve in the formation of PS. At small anodization current densities, the microstructure of PS is not completely depleted of holes. The energy gained from the anodization potential may not be sufficient for the holes to overcome the resistance at certain regions of the microstructure. As a result, holes are trapped at those sites. When the anodization is performed with higher anodization current densities, holes gain more energy, and would move through the structure with ease. This change in the hole transport affects the microstructure of PS. But, still there would be some regions in the microstructure where the holes could get trapped. At some higher anodization current density called critical anodization current density, holes reach a state where the anodization potential may not provide enough energy to overcome the resistance offered by the microstructure of PS. Any further increase in the anodization current density, does not affect the microstructure of PS. However, to keep up the hole transfer rate with the anodization current density, the removal of Si atoms would be predominant at the pore depths or PS/c-Si wafer interface. This results in the increase of growth rate without any significant alteration in n_{eff} of PS. Hence, with the increasing anodization current density, there is a linear increase in the growth rate and a near saturation in n_{eff}.

4.2.3 Effects of resistivity on growth rate and effective refractive index of PS

Resistivity of c-Si wafer strongly affects both the growth rate and refractive index of PS. Figure 4.20 shows the variation of growth rate with wafer resistivity for 25, 50 and 75 mA/cm^2 current densities. The variation of growth rate with wafer resistivity, unlike the variation with anodization current density, is non-monotonic. A similar variation has been observed for the refractive index of aged PS with wafer resistivity as shown in Fig. 4.21(a). Although these PS layers have significant fractions of oxides and hydrides as constituents, the refractive index still provides details of the microstructure formed by Si and void regions. To substantiate the claim, Fig. 4.21(b) shows the effect of resistivity on the refractive index of freshly prepared PS. Based on these observations it is clear that when there is a change in the growth rate, there will be a corresponding change in n_{eff}.

TH-1094_04612102

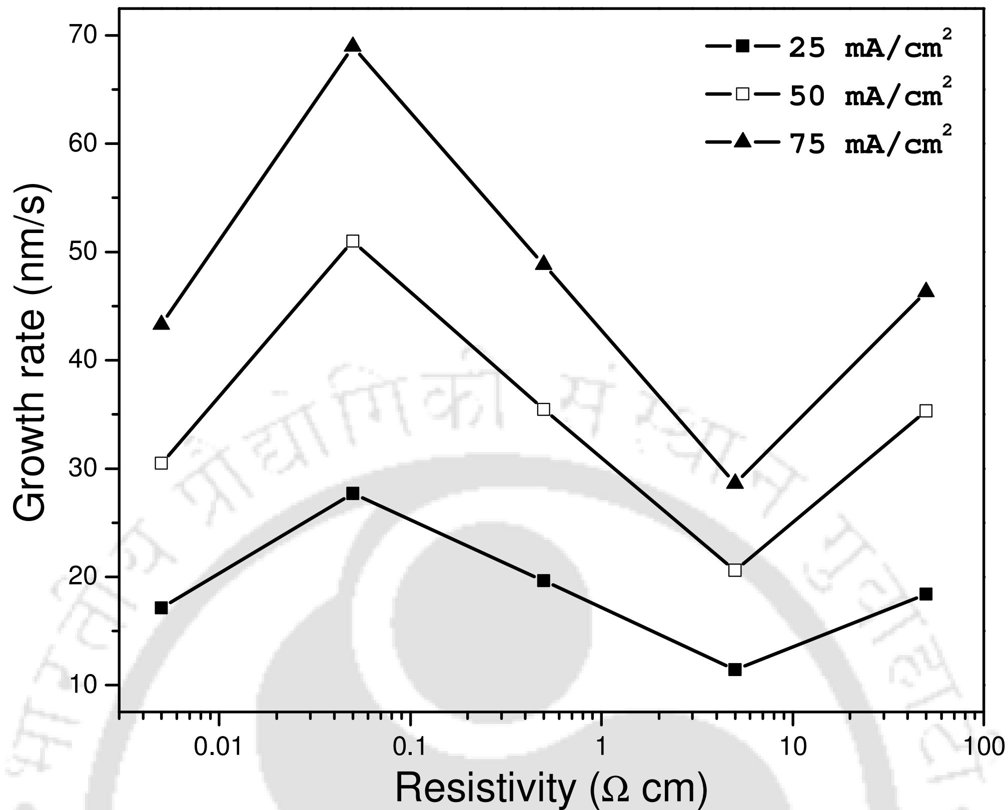

Figure 4.20 Effect of wafer resistivity on the growth of PS for various anodization current densities.

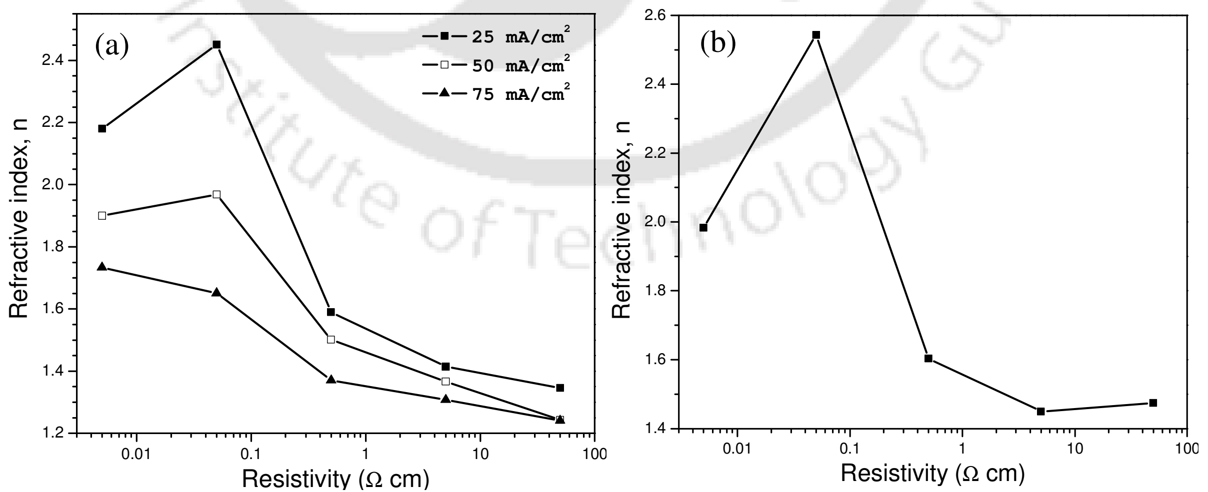

Figure 4.21 Effect of wafer resistivity on the effective refractive index n_{eff} of (a) aged and (b) as-prepared PS for various anodization current densities. n_{eff} of PS prepared on different resistive c-Si wafers are compared at 700 nm radiation.

4.3 SUMMARY

A systematic study on the growth rate and refractive index of PS under the variations of anodization current density and c-Si wafer resistivity is presented. The steps involved in the determination of thickness and refractive index are explicitly shown by considering two representative PS for the two cases – fitting and non-fitting of the interference pattern in the measured reflectance spectrum with EMT. With the determination of these parameters, the effects of anodization current density and wafer resistivity on growth rate and refractive index are understood based on the modulations in microstructure and the growth kinetics.

TH-1096_04612102

CHAPTER

5

STUDIES ON PHOTOLUMINESCENCE IN POROUS SILICON

Photoluminescence (PL) is one of the most extensively studied phenomena in porous Si (PS). Yet the mechanism [1-11] and certain features in the PL of PS like the blue-shift of the PL peak centre with the excitation energy [12, 13], the spectral features of photoluminescence excitation spectrum [14-16], etc. are not clearly understood. This chapter presents the studies on PL in PS towards an understanding of the basic mechanism and certain common spectral features in PL of PS.

5.1 EXPERIMENTAL RESULTS ON PHOTOLUMINESCENCE OF PS

Efficient visible PL is not commonly observed on all PS prepared on many different c-Si wafer resistivities. Amongst the PS considered for the present thesis work, the efficient visible PL is limited to PS prepared on high resistivity c-Si wafers. So, in this chapter, PS prepared from c-Si wafers of resistivities 1–10 Ω cm and above are only considered for the investigation. It is an observed fact that the spectral features of PL on many PS layers are very similar. So, in this chapter, the discussions are limited to five (05) PS samples, which are considered to be the representatives of different sets. Table 5.1 details the preparation conditions of the representative PS for a quick reference.

TH-1099_04612102

Table 5.1 The details of the anodization process, electrolyte concentration, wafer resistivity, anodization current density, anodization time and sample conditioning of the representative PS.

Anodization process	Electrolyte HF: Ethanol	Resistivity (Ω cm)	Anodization Current density (mA/cm^2)	Anodization time (min)	Sample conditioning
Constant current	1 : 1	1–10	50	15	Aged (5 months in ambient)
			80	5	
Pulsed current (20 Hz and 40% duty cycle)	1 : 1	1–10	80	5	As-prepared
					Aged (5 months in ambient)
Pulsed current (10 Hz and 60% duty cycle)	2 : 3	1–10	25	0.75	Aged (5 months in ambient)
		5K–12K	25	2	

5.1.1 Photoluminescence spectra

Figures 5.1 and 5.2 show the PL spectra of the representative PS prepared under different anodization conditions at various excitations. The dependent parameters of the PL spectra in Figs. 5.1 and 5.2 can be given as [17]

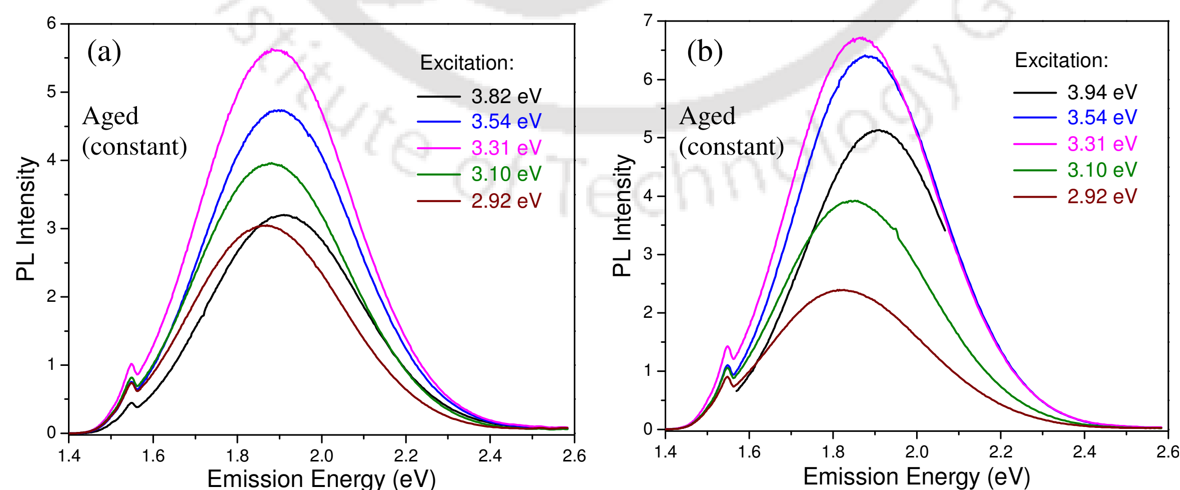

Figure 5.1 Measured PL spectra of aged PS prepared on c-Si wafers of resistivity 1–10 Ω cm under constant current anodization process using (a) 50 mA/cm^2 anodization current density for 15 min and (b) 80 mA/cm^2 anodization current density for 5 min.

TH-1098_04612102

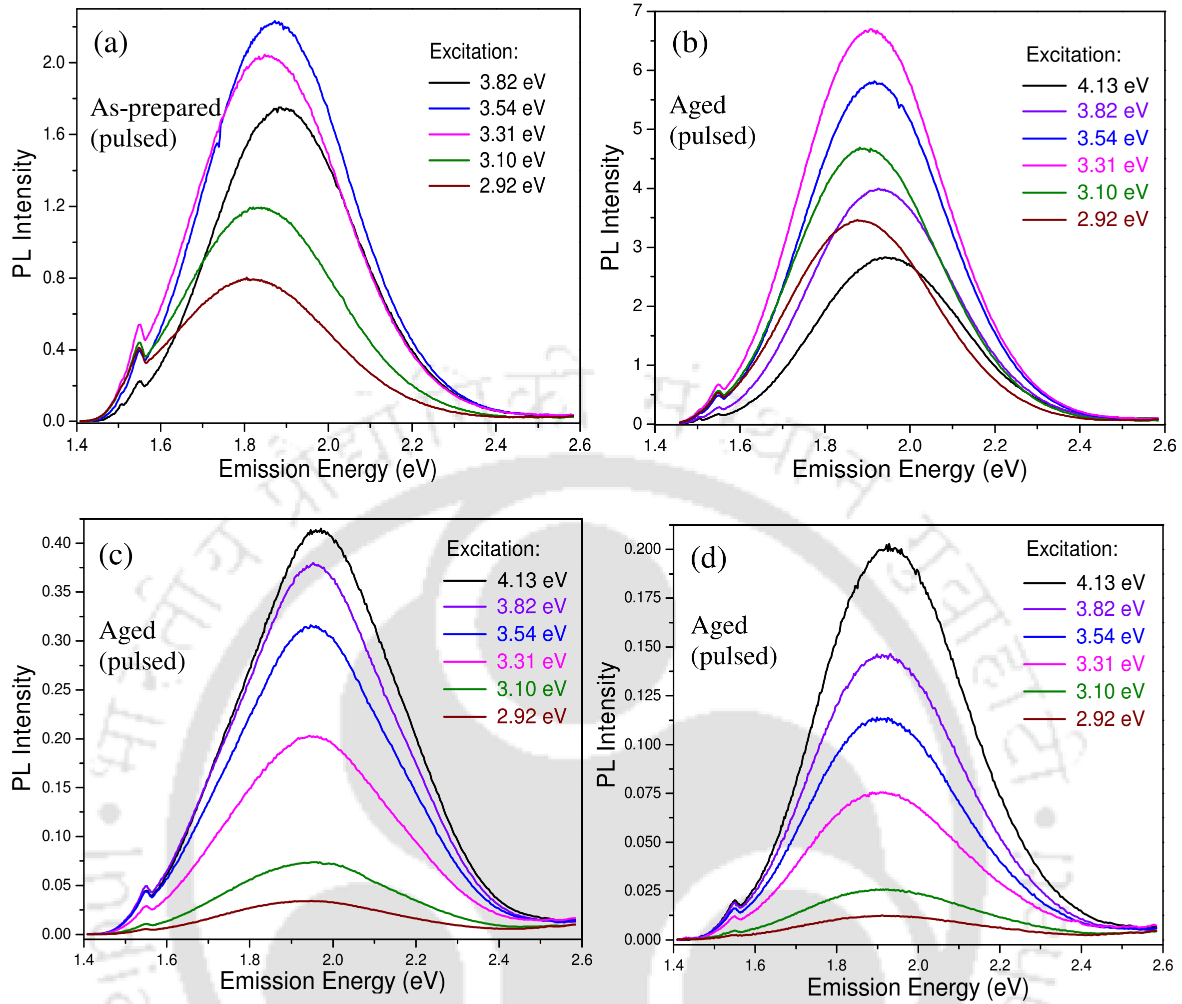

Figure 5.2 Measured PL spectra of (a) as-prepared and (b) aged PS prepared under pulsed current (Freq = 20 Hz and Duty cycle = 40 %) anodization process on 1–10 Ω cm using 80 mA/cm^2 anodization current density for 5 min. Also, the PL spectra of PS prepared under pulsed current (Freq = 10 Hz and Duty cycle = 60 %) anodization process using 25 mA/cm^2 anodization current density on c-Si wafers of resistivities (c) 1–10 Ω cm and (d) 5K–12K Ω cm for 45 and 160 sec, respectively.

$$I_{Em}(\omega,\omega') = A(\omega)\, P_{ES}(\omega,\omega')\, P_{Em}(\omega')\, \eta(\omega'), \quad (5.1)$$

where I_{Em}, A, P_{ES}, P_{Em}, η, ω and ω' are the emission intensity, the exciton creation (absorption) probability, the probability that an exciton traps at an emission state, the probability that an exciton in the emission state returns back to the ground state by the emission of a photon, the instrument spectral response, excitation photon frequency and emission photon frequency, respectively.

As the PL spectra have already been corrected for the excitation photon flux, Eq (5.1) is independent of the excitation flux. On the lines of Eq. (5.1), the spectra in Fig. 5.1 and 5.2 are functions of ω'. A small peak, near around 1.55 eV, is identified to be the spectral response of the instrument, and is believed not to affect the features of the spectra as a whole.

A few observations in Figs. 5.1 and 5.2, which are also repeatedly reported in the literatures related to PL of PS, are as follows:

PL from PS is a broad spectrum of nearly 1 eV spectral width between the onset and offset of the luminescence signal. The peak intensity of PL is strongly dependent on the excitation photon frequency ω. In Figs. 5.1(a), 5.1(b), 5.2(a) and 5.2(b), the PL peak intensity is greater neither for high nor for low ω. However, in Figs. 5.2(c) and 5.2(d), the peak intensity increases monotonically with increasing ω. It is observed from Figs. 5.1(a) and 5.1(b) that the anodization current density also affect the PL peak intensity. This would mean that the microstructure of PS would influence the PL signal. With Figs. 5.2(a) and 5.2(b), it would be clear that not only the microstructure of PS, but mere storage in the ambient would also affect the PL signal. Apart from the variations in PL peak intensity, it is also observed in Figs. 5.1 and 5.2 that the PL peak centre blue-shifts with ω.

5.1.2 Photoluminescence excitation spectra

Photoluminescence excitation (PLE) spectroscopy is an alternative to absorption

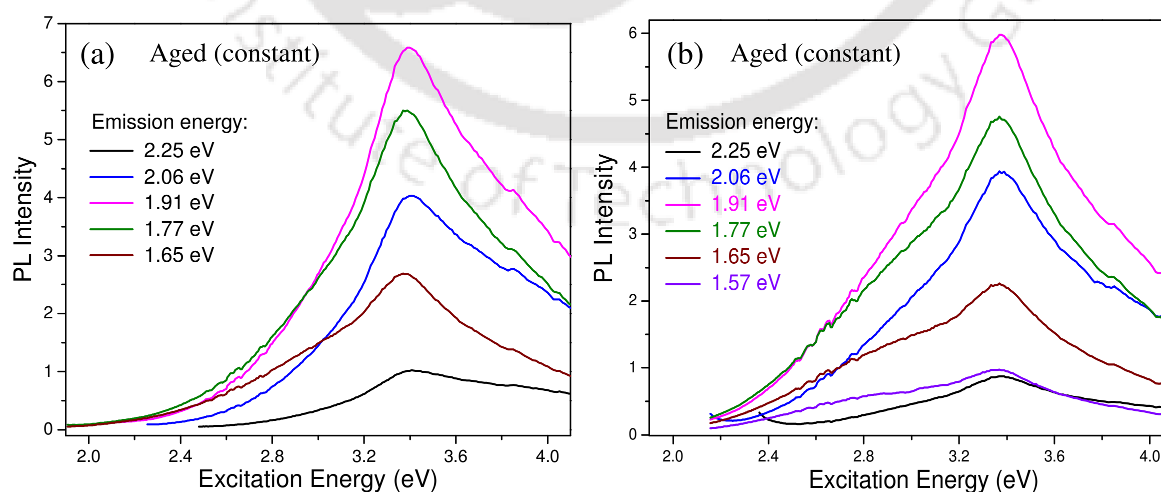

Figure 5.3 Measured PLE spectra of aged PS prepared on c-Si wafers of resistivity 1–10 Ω cm under constant current anodization process using (a) 50 mA/cm^2 anodization current density for 15 min and (b) 80 mA/cm^2 anodization current density for 5 min.

TH-1099_04612102

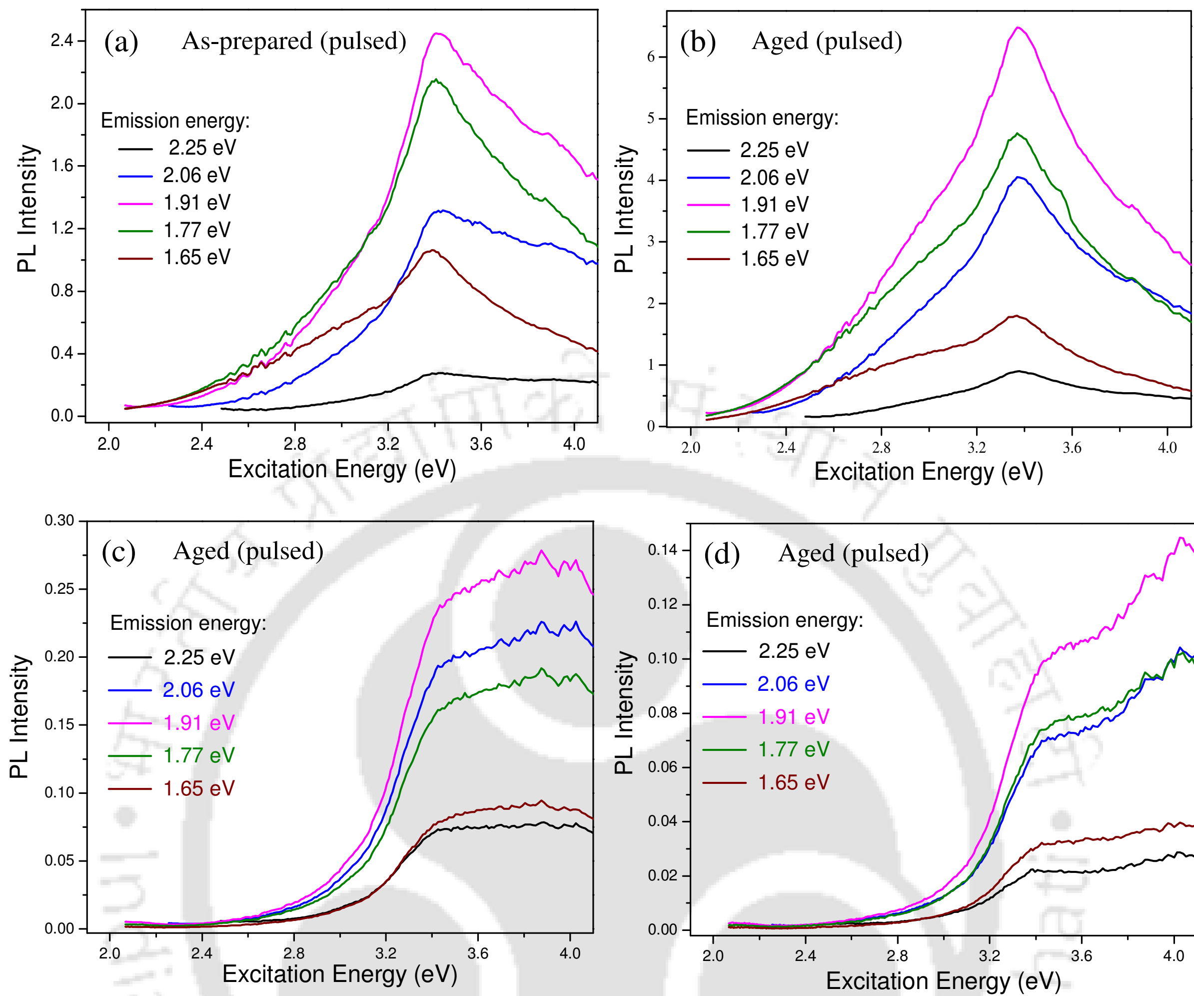

Figure 5.4 Measured PLE spectra of (a) as-prepared and (b) aged PS prepared under pulsed current (Freq = 20 Hz and Duty cycle = 40 %) anodization process on 1–10 Ω cm using 80 mA/cm^2 anodization current density for 5 min. Also, the PLE spectra of PS prepared under pulsed current (Freq = 10 Hz and Duty cycle = 60 %) anodization process using 25 mA/cm^2 anodization current density on c-Si wafers of resistivities (c) 1–10 Ω cm and (d) 5K–12K Ω cm for 45 and 160 sec, respectively.

spectroscopy in opaque samples [18]. For PL studies, PLE spectroscopy is much more powerful tool than the absorption spectroscopy as it is only sensitive to the absorption that causes the luminescence. The broad spectral feature of PL of PS is exploited in PLE spectroscopy to record the spectra at various emission energies without much overlap. Figures 5.3 and 5.4 show the PLE spectra of the representative PS at various emission energies. The dependent parameters of the PLE spectra are same as that of the PL spectra, and can be given by Eq. (5.1). The only difference being that the PLE spectra are functions

of ω rather than ω'.

The spectra in Figs. 5.3(a), 5.3(b), 5.4(a) and 5.4(b) show very similar spectral features including a peak near around 3.4 eV. However, no such features are observed in the spectra in Figs. 5.4(c) and 5.4(d). The spectra in Figs. 5.4(c) and 5.4(d) are although very different, there is a distinct change in their spectral feature at 3.4 eV. The significance of 3.4 eV in the PLE spectra would be discussed later in this chapter with its correspondence to the absorption spectra.

It is observed that the PLE spectra recorded at different emission energies on a particular PS show quite similar spectral features in spite of the large difference in their intensities. As PLE is related to the optical absorption of the material, this observation signifies that there could be perhaps only one underlying optical absorption mechanism for the broad PL from PS.

5.2 THEORETICAL SIMULATION OF OPTICAL ABSORPTION

From Eq. (5.1), it is inferred that the PLE spectrum is only related, but not identical, to an absorption spectrum. The parameter P_{ES} being functions of both ω and ω', the spectral features of PLE are also affected by P_{ES}. To proceed any further in the understanding of the mechanism of PL of PS, the optical absorption of PS must be found separately. But, as due to the inhomogeneity of PS, experimental determination of optical absorption merely through spectral reflectance measurements is not possible. Theoretical simulation of optical absorption of PS is also not possible, since the imaginary part of the refractive index of PS is still undetermined.

However, the PLE spectra in Figs. 5.3 and 5.4 have a clue. The 3.4 eV, where the PLE spectral features change considerably, corresponds to the E_1 transition of bulk c-Si [19]. It is nothing but the least of all direct bandgaps of bulk c-Si, and lies at the *L* point of the Brillouin zone. This observation has prompted to simulate the optical absorption through bulk c-Si optical constants.

For the purpose of simulating the optical absorption spectrum, the following equations have been used

$$A(\omega) = (1 - R(\omega))\,(1 - e^{-\alpha(\omega)d}), \tag{5.2}$$

TH-1099_04612102

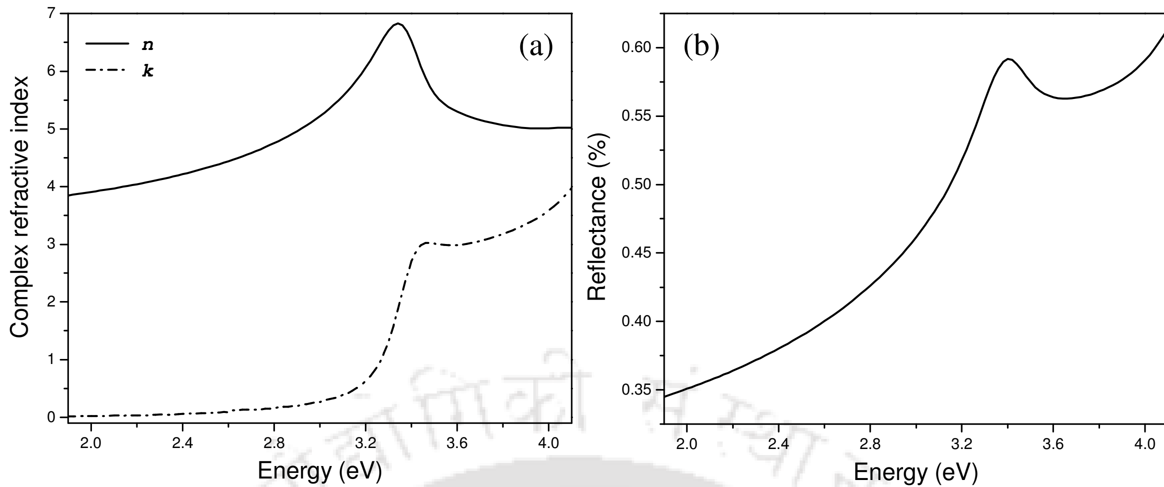

Figure 5.5 Dispersions of (a) complex refractive index and (b) normal incidence reflectivity of bulk c-Si

$$R = \frac{(n-1)^2 + k^2}{(n+1)^2 + k^2} \tag{5.3a}$$

$$\alpha = 4\pi k\omega/c \tag{5.3b}$$

where n and k are the real and imaginary parts of the complex refractive index of bulk c-Si, respectively, R is the normal incidence reflectivity, d is the thickness, ω is the frequency of radiation and c is the speed of light. Figures 5.5(a) and 5.5(b) show the dispersions of complex refractive index and normal incidence spectral reflectivity simulated through Eq. (5.3a) of bulk c-Si, respectively.

Equation (5.2) is although for normal incidence condition, the spectral features of optical absorption are not significantly affected even when it is averaged over all oblique angles of incidence (say, 0 to π/2) with equal proportions of s- and p- polarizations. So, Eq. (5.2) suffices in its simplest form for the simulation of optical absorption spectrum. However, in the literature, for the analysis of PLE spectrum, the absorption is taken to be $(1–e^{-\alpha d})$ [14, 15]. The (1–R) factor is generally omitted. It is evident from Eq. (5.2) that it is possible to omit (1–R) only if R=0 or at least show a weak spectral dependence. In the case of c-Si, at least in the spectral region of interest, R is strongly spectral dependent as can be in Fig. 5.5(b). So, in general, the reflectance with all possible oblique angles of incidence or at least the normal incidence reflectance as in Eq. (5.2) must be used for the simulation of optical absorption spectrum in the analysis of PLE spectrum for any solids.

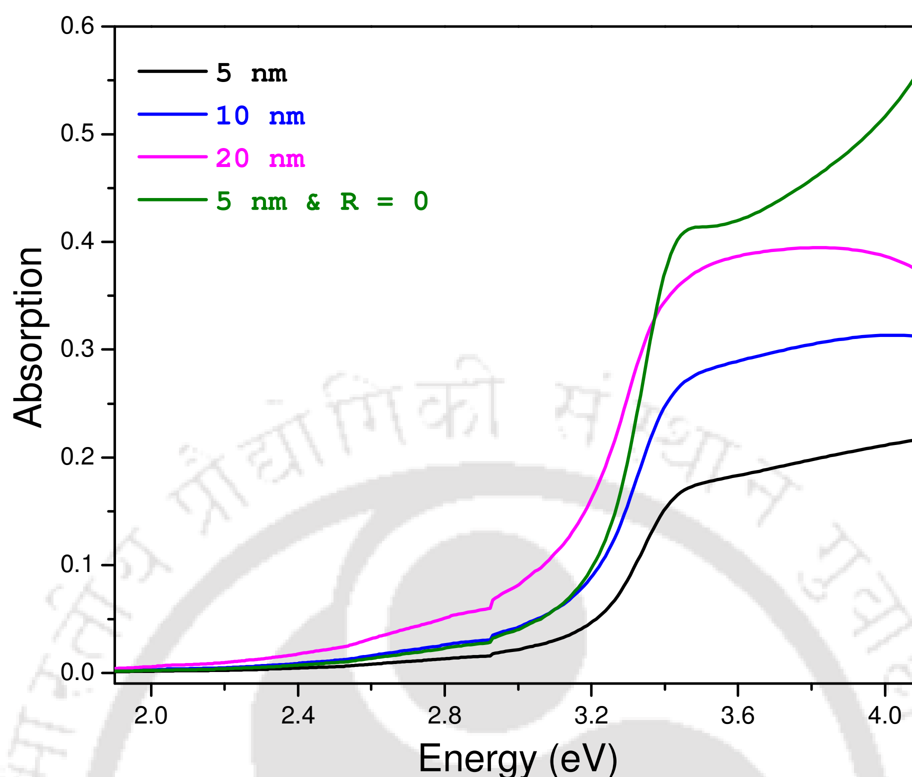

Figure 5.6 Theoretical simulations of normal incidence optical absorption of thin films with bulk c-Si optical constants for various thicknesses and zero reflectance condition through Eq. (5.2).

Theoretical simulations of optical absorption spectra through bulk c-Si optical constants for various thicknesses and zero reflectance condition are shown in Fig. 5.6. The spectral features of all the spectra are very similar below 3.4 eV. However, above 3.4 eV, which is the onset of strong absorption, the spectra show clear dependence on the thickness and reflectance of the film.

5.3 COMPARISON OF SIMULATED OPTICAL ABSORPTION WITH PLE

A comparison of simulated optical absorption with the measured PLE reveals that though the simulations have been with bulk optical constants of c-Si, the spectral features are very similar to that of the measured PLE of PS. It is from the close correspondence of these spectra, it is identified that the effect of physical quantum confinement is insignificant in PS. Moreover, if there were a significant quantum confinement effect, the *L* point absorption would be at much higher energies or at least different from the observed position in PLE spectra.

TH-1099_04612102

5.4 STRUCTURE OF PS

So far in the discussion, the microstructure of PS is not considered. The intriguing observation that the PLE spectra of PS show similar spectral features as that of the absorption of bulk c-Si necessitates considering the microstructure of PS. In the following, two possible descriptions on the microstructure of PS are given for elucidation.

Ever since the discovery of efficient visible PL, PS is believed to comprise quasi-isolated small Si crystallites (since it is widely been prepared from c-Si wafer) of different shapes and sizes. This description of PS urges to believe that the outcome of the measurements like optical absorption, Raman scattering and photoluminescence spectroscopy is due to the sum of the independent contributions of the individual crystallites. An alternative description, which is guided by the formation kinetics of PS, would be as a c-Si structure with impregnated pores of different shapes and sizes that would make labyrinth permeation in crystalline matrix. Failing to convince the existence of isolated nanocrystallites in PS with the latter description, the outcome of the measurements is perceived as interdependent, and contributed by the entire structure.

The latter description is supported by the present observations in PLE of PS. Further insight on the microstructure of PS is provided by infrared vibrational spectroscopic studies. Figure 5.7 shows the infrared vibrational spectra of a typical PS and bulk c-Si for

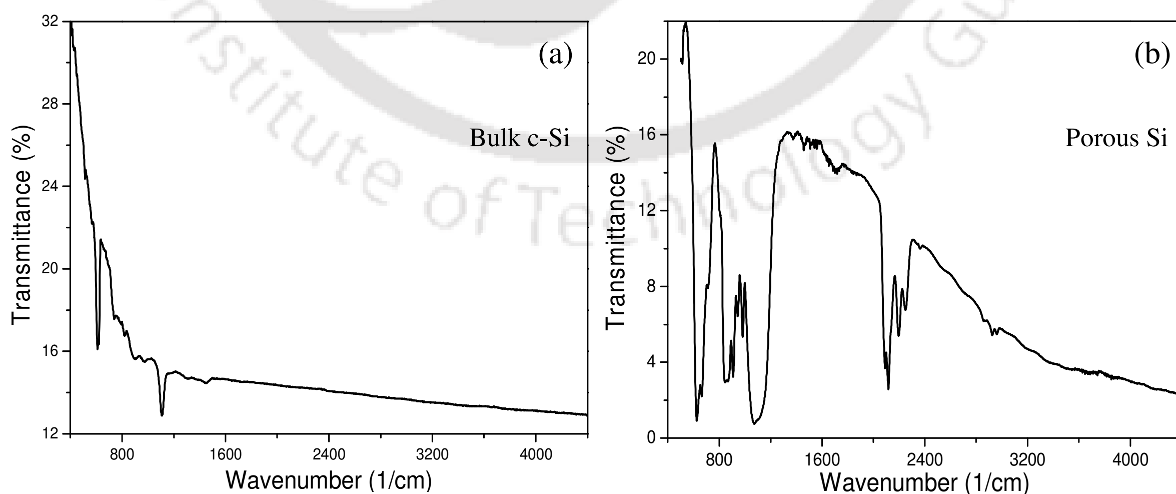

Figure 5.7 Measured normal incidence transmittance spectra of (a) c-Si of resistivity 1–10 Ω cm and (b) PS prepared by pulsed current electrochemical etching process on c-Si wafer of resistivity 1–10 Ω cm using 80 mA/cm^2 anodization current density for 5 min.

comparison. The vibrational spectrum of PS is very different from the bulk c-Si. The study reveals that PS not only contains Si with labyrinthine network of pores, but also contains some forms of hydrides and oxides as its constituents. The core of Si, the region in between the pores, in PS is defect free and also protected by the surrounding covalently bonded Si atoms from the attack of chemical species. However, the surfaces of Si, or pore walls, are vulnerable to the attack of chemical species. So the hydrides and oxides, which are found from vibrational spectroscopic studies, could presumably chemisorb to the vulnerable Si surfaces or the pore walls.

To summarize, PS is described as c-Si structure with impregnated pores of different shapes and sizes that would make labyrinth permeation in crystalline matrix. The Si atoms at the pore walls are exposed to the ambient and are vulnerable to the attack of reactive chemical species like oxygen, hydrogen, etc. Hence, PS is not merely a composite of Si and voids, but also composed of certain chemical compounds such as hydrides and oxides of Si. Depending on the available Si surfaces, which is controlled by the anodization conditions, and the reactive chemical species present in the ambient, the fractional presence of the chemical compounds at the pore walls varies.

5.5 MECHANISM OF PL IN PS

Physical quantum confinement of excitons in PS is almost believed to be a fact for nearly two decades. Although there are numerous controversial proposals for the mechanism of PL in PS – for and against the quantum confinement model, the effect of physical quantum confinement is generally believed to exist in the creation of excitons (i.e., optical absorption). The present observations in PLE of PS contradict the usual belief on the existence of the effect of quantum confinement in the creation of excitons. So, a new proposal is necessary indeed for the mechanism of PL in PS.

The optical absorption that causes efficient visible PL in PS is identified to be same as in the bulk c-Si. So, the refractive index of Si in PS must also be the same as in the bulk counterpart. At this point, it is necessary to note that the calculated refractive index of PS in Chapter 4 is the effective refractive index, or in other words, a parameter that merely denotes the phase modulation of a propagating electromagnetic wave in the medium. Whereas, the refractive index, in the present context, is the refractive index of Si regions in PS with no interference from the composite nature of the material.

TH-1096_04612102

Since the refractive index of Si in PS is same as in the bulk c-Si, the optical properties of Si in PS must also be the same as in its bulk counterpart. So, the efficient visible PL, which is absent in bulk c-Si, certainly cannot be a property of Si in PS. However, as the PLE spectra reveal the absorption characteristics of bulk c-Si, the Si in PS would probably mediate the process.

In the discussions on the structure of PS (Section 5.4), it has been remarked that the Si dangling bonds at the pore walls are passivated by reactive chemical species like oxygen, hydrogen, etc. The passivation may introduce some electronic energy states that are not present in the bulk c-Si. Some of those electronic energy states could presumably the emission states for PL.

Although the electronic energy states formed by oxides and hydrides could be the emission states for PL, unless the effect of oxides and hydrides on PL is shown explicitly, this would remain as a conjecture. A possible study to show explicitly the effect of oxides and hydrides on PL would be to compare the PL and the infrared vibrational spectral features of freshly prepared and aged PS.

Figure 5.8 depicts the effect of aging on PL of PS. The PL intensity has enhanced by several folds and the PL peak has slightly blueshifted with aging. If the emission states are formed by chemisorbed species, there would certainly be some changes in the fractional

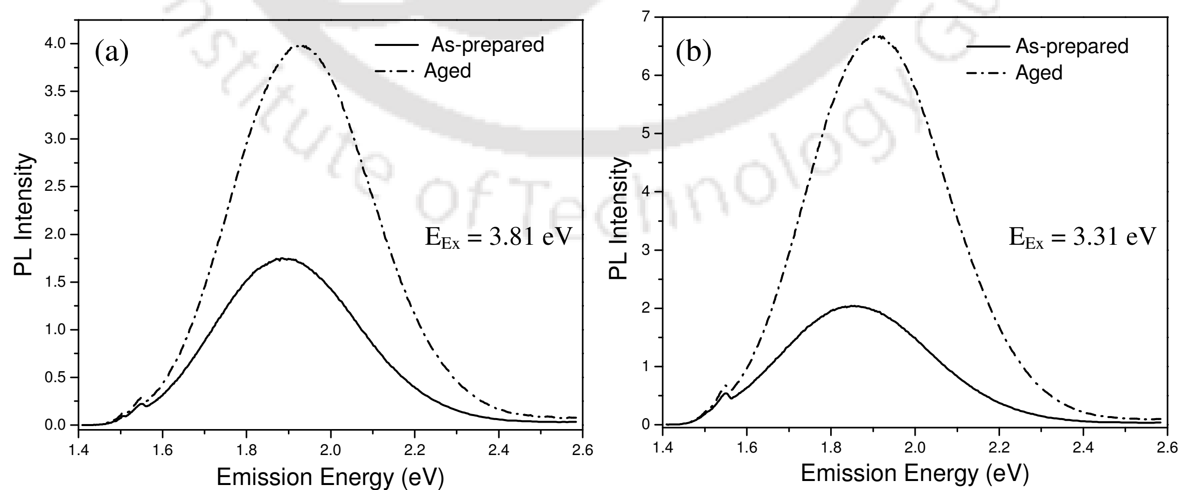

Figure 5.8 The effect of aging on the PL of PS recorded at (a) 3.81 eV and (b) 3.31 eV excitations. The PS is prepared by pulsed current electrochemical process on c-Si wafer of resistivity 1–10 Ω cm using 80 mA/cm^2 anodization current density for 5 mins.

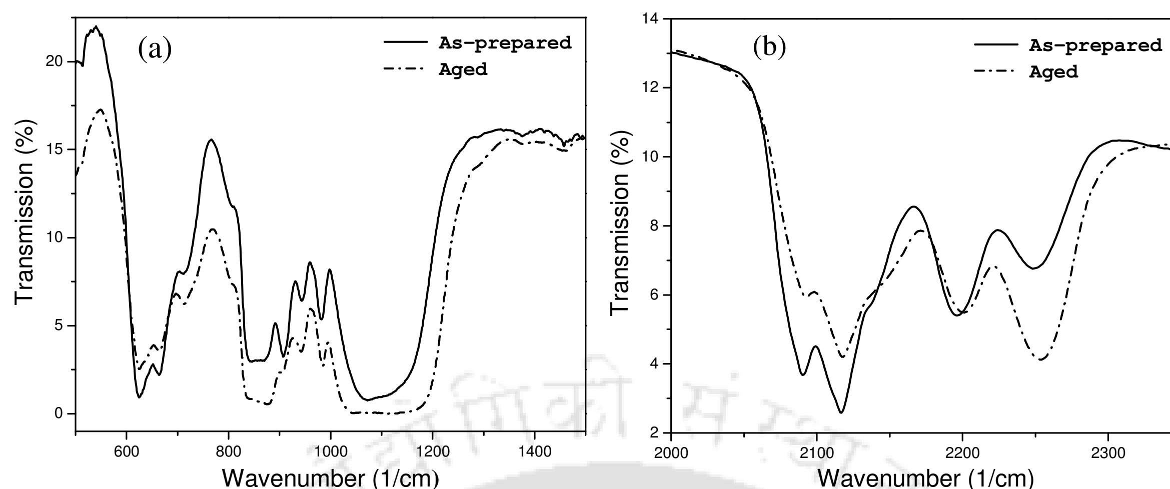

Figure 5.9 Measured normal incidence FTIR transmittance spectra of both as-prepared and stored in ambient conditions for 5 months prepared by pulsed current electrochemical etching of 1–10 Ω cm resistivity c-Si wafer with a current density of 80 mA/cm^2 for 5 mins in the spectral range (a) 500–1500 cm^{-1} and (b) 2000–2350 cm^{-1}. The vibrational absorption modes are attributed as follows: 624 cm^{-1} to Si–H bending in Si_3–SiH, 663 cm^{-1} to Si–H wagging, 827 cm^{-1} to SiO bending in O–Si–O, 856 cm^{-1} to SiH_2 wagging, 906 cm^{-1} to SiH_2 scissor, 948 cm^{-1} to SiH bending in Si_2–H–SiH, 979 cm^{-1} to SiH bending in Si_2–H–SiH, 1034–1182 cm^{-1} to SiO stretching in O–SiO and C–SiO, 2090 cm^{-1} to SiH stretching in Si_3–SiH, 2116 cm^{-1} to SiH stretching in Si_2–H–SiH, 2197 cm^{-1} to SiH stretching in SiO_2–SiH, and 2248 cm^{-1} to SiH stretching in O_3–SiH.

presence of different chemical species with aging. The infrared vibrational spectra, which are recorded near about the same time the PL measurements, are shown in Fig. 5.9. The strengths of absorption of Si_3–SiH, Si–H and Si_2H–SiH show considerable decrease, and whereas, O–Si–O, SiH_2, O–SiO, C–SiO and O_3–SiH show considerable increase in their strengths.

Based on these observations, the mechanism of PL of PS would be given, in relation to the parameters of Eq. (5.1), as follows:

The exciting photons, say, of frequency ω, are strongly absorbed by Si in PS, although the chemisorbed species at the pore walls would also absorb the photons. The absorption of photons creates excitons (i.e., electron–hole pairs) of energy ħω with a probability A. The excitons, with their kinetic energy supplied by the exciting photons, move through the solid, and, with a probability P_{ES}, reach the emission energy states ω' formed by the

TH-1099_04612102

chemisorbed species at pore walls. The excitons at the emission states, with a probability P_{EM}, transit to the ground state by the emission of a photon ω'.

5.6 UNDERSTANDING THE EXPERIMENTAL DATA

Having proposed a mechanism for the PL of PS, in the following, the spectral features in the luminescence of PS are explained.

5.6.1 Broad PL spectrum of PS

The PL of PS is a broad spectrum, which encompasses approximately 1 eV, as can be inferred from Figs. 5.1 and 5.2. Since the PL is ascribed to the electronic energy states formed by the reactive chemical species at pore walls, the broad spectral feature is understood on the basis of the chemical environment at the pore walls. The FTIR transmittance spectrum of PS in Fig. 5.7(b) is considered for reference. The infrared absorption of the chemical species in PS is found to be relatively broad. The broadening of infrared absorption spectrum, in general, is affected by the bond angle, bond length and the surrounding chemical environment of the chemical species. If the deviations from the mean values of bond angle and bond length are more, then the width of the absorption peak would also be more. The width of the absorption peak would also increase when the absorbing chemical species are in many different chemical environments. The observed widened absorption peaks in PS are due to the above mentioned causes: bond angle, bond length and chemical environment differences.

The bond angle, bond length and chemical environment differences not only affect the vibrational energy levels, but also the electronic energy levels of the chemical species. Due to these reasons, the PL of PS is spectrally broad.

5.6.2 Excitation energy dependent peak position

Photoluminescence peak position is one of the characteristics of a chemical species. In general, the PL peak position is unaffected with the change of excitation energy, although the intensity of luminescence is strongly affected. This is often considered to be one of the features that distinguish PL from scattering phenomena [20]. However, in PS, the PL peak position blue-shifts with the increase of excitation energy as can be seen clearly in Figs. 5.1(a), 5.1(b), 5.2(a) and 5.2(b). This may cause some doubt whether the observed

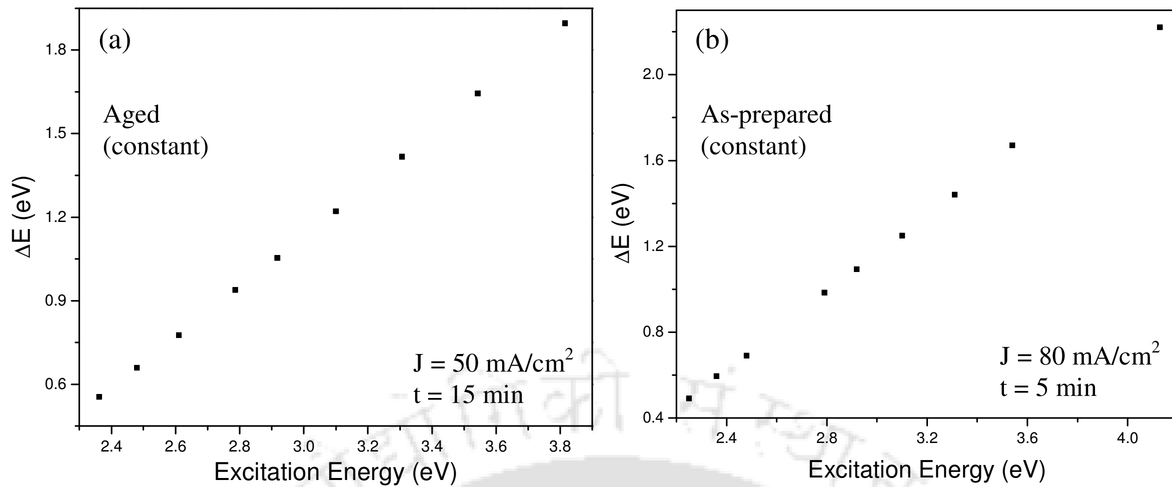

Figure 5.10 Plot of energy difference between the excitation and PL peak position to the energy of excitation of PS prepared on c-Si wafers of resistivity 1–10 Ω cm.

phenomenon is really PL. To clarify the point, in Fig. 5.10, the energy difference between the excitation and the PL peak position is plotted against the energy of excitation for two representative PS layers. The plots have a positive slope. If the phenomenon were scattering, the difference between the excitation and the PL peak centre would be a constant, and the plots would just be parallel to the excitation energy axis.

The phenomenon, without doubt, is PL. Now, it is to understand the blue-shift of the PL peak position with the excitation energy. In literature, this feature has already been explained on the lines of quantum confinement model [21]. Until now, although there are several proposals for the mechanism of PL in PS, quantum confinement model is the only model that could able to explain the blueshift of the PL peak position with excitation energy. Since the present observations stand against the quantum confinement model, in the following, a new explanation, without contradicting the proposed mechanism of PL in PS, is presented.

In Eq. (5.1), of the dependent parameters of PL intensity, P_{ES} is functions of both excitation ω and emission ω' frequencies. It is due to the fact that P_{ES} is itself proportional to the product of two other functions, which can be given as

$$P_{ES}(\omega,\omega') = g(\omega')\, f(\omega,\omega') \tag{5.4}$$

where g is the density of states per unit energy interval at the pore walls and f is the

TH-1090_04612102

probability distribution function, which gives the probability of occupation of carriers at those states. Once again f is a function of both ω and ω'; it is f that is relevant to the present discussion. The functional form of f could be considered similar to Maxwell-Boltzmann distribution function, since the carriers occupy the emission states from the conduction band. For the following qualitative discussion, Maxwell-Boltzmann distribution function itself would suffice, which can be written as

$$f(\omega,\omega') = N \exp[-E(\omega')/k_B T(\omega)] \quad (5.5)$$

where E is the energy of the state corresponding to ω', T is the temperature, k_B is the Boltzmann constant, N is the normalization constant and the terms in the parenthesis signify the functional dependences of the parameters. The temperature, in the present context, is not the lattice temperature, but, the excitonic temperature, which is the average kinetic energy of the excitons.

The excitons, after being created, do thermalise, and reach a state of thermodynamic equilibrium. In this case, they reach a quasi-thermal equilibrium, where the excitons are in thermal equilibrium among themselves, but, not with the lattice [22]. So, the excitons carry the knowledge of excitation until they reach the emission states. This is the very reason, in Eq. (5.5), the temperature is explicitly shown as a function of ω, the energy of excitation. As the excitation energy is increased, the excitonic temperature is increased, and thereby, the occupation probability of higher energetic states is favoured. This results in the blue-shift of the PL peak position with the increase of excitation energy.

5.6.3 Dissimilarities between PLE and absorption

Although PLE is only related to the absorption, and also it is not expected for PLE to bear every minute detail of an absorption spectrum, the pronounced dissimilarities only on efficient luminescent PS (see Figs. 5.3(a), 5.3(b), 5.4(a) and 5.4(b) for PLE and Figs. 5.1(a), 5.1(b), 5.2(a) and 5.2(b) for PL) have intrigued to devote a discussion on the issue.

The PLE spectra in Figs. 5.3(a), 5.3(b), 5.4(a) and 5.4(b) are very similar and show a peak near around 3.4 eV. However, no such feature is observed in the simulation of absorption spectra with bulk optical constants of c-Si through Eq. (5.2) shown in Fig. 5.6. It is noteworthy that for the purpose of simulation only the specular reflectance at the interface is considered. So the simulation results are valid only if PS interface is smooth, or the diffused reflectance or incoherent scattering at the interface is negligibly small.

However, it is observed that the specular reflectance of efficient luminescent PS is weak. No multiple beam interference pattern is observed for these PS. On the other hand, the specular reflectance of weak luminescent PS (see Figs. 5.2(c) and 5.2(d) for PL and Figs. 5.4(c) and 5.4(d) for PLE) is much appreciable, which is evident from the multiple beam interference patterns. Based on these observations, it is inferred that the dissimilarities between the PLE of efficient luminescent PS and the simulated absorption spectra is due to poor consideration of the reflectance at the PS interface. To substantiate the claim, in the following, the incoherent spectral scattering is shown to have the spectral features of the PLE of efficient luminescent PS, qualitatively.

Figure 5.11(a) shows the specular reflectance of a typical PS showing multiple beam interference pattern. The interference pattern is fitted through Eq. (3.8) with refractive index and thickness as determined through the procedures described in Chapter 3. The refractive index as determined in the spectral region of interference is extrapolated to the interference free reflectance through Bruggeman's effective medium theory with the appropriate porosity as the input. The mismatch in the magnitudes between the measured and the fit is due to incoherent scattering, which is not considered in the fit. The measured reflectance R can be related to the simulated reflectance R_0 through the following relation

$$R = \zeta R_0 \tag{5.6}$$

where ζ is the fraction of the coherent radiation in the direction of regular propagation.

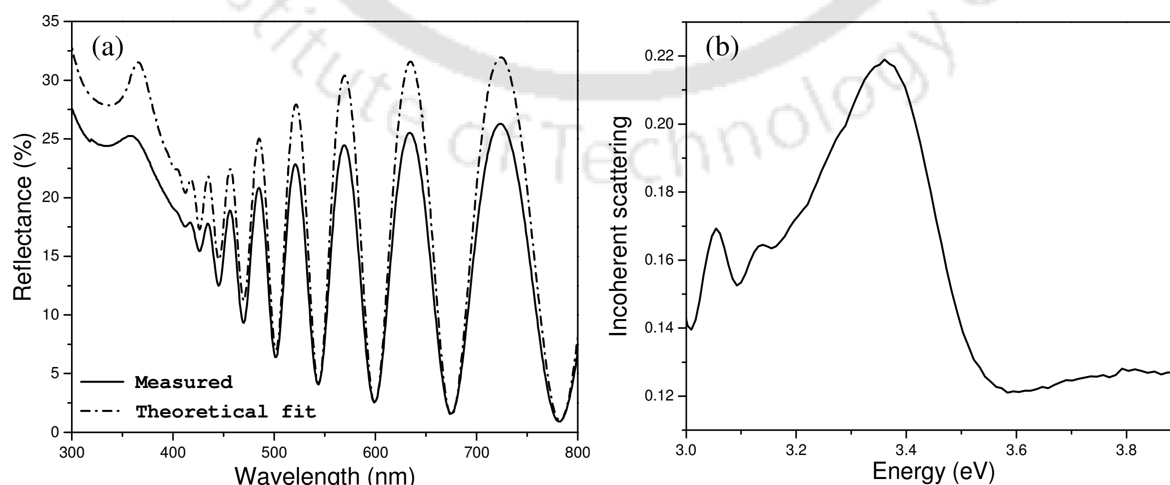

Figure 5.11 (a) specular reflectance and (b) incoherent spectral scattering of PS prepared on c-Si wafer of resistivity 0.001–0.005 Ω cm using 25 mA/cm^2 anodization current density for 1 min.

TH-1092_04612102

Then, (1–ζ) is the incoherent scattering fraction. Since, R and R_0 are known, it is a simple task to identify (1–ζ) for the system under consideration. Figure 5.11(b) shows the spectral dependence of (1–ζ) in the interference free region. The incoherent spectral scattering show a peak near around 3.4 eV similar to that of the PLE spectra of efficient luminescent PS. The incoherent spectral scattering is itself the spectral absorption of the material. Thus, the absence of a peak at 3.4 eV in the simulation of absorption spectrum is only due to poor consideration of reflectance at the interface.

There is another feature in the PLE of efficient luminescent PS – the down steep of the spectra above 3.4 eV gradually flattens as the emission energy increases. This could be understood from P_{ES}, which is the only parameter that affects the spectral features of PLE, apart from the absorption. From Eq. (5.4), it is *f*, the probability distribution function, that is relevant to the present discussion. So, once again I would like to draw the attention on Eq. (5.5). As clearly pointed out in the discussion on the blueshift of the PL peak centre (Section 5.6.2), the occupation probability for higher energetic states is favoured at higher energetic excitations. So, as the emission energy increases, the intensity for higher energetic excitations also increases. Thus, the down steep of the PLE spectra above 3.4 eV is affected.

5.6.4 Luminescence enhancement with anodization current density

Figure 5.12 shows the effect of anodization current density on the PL of PS. The

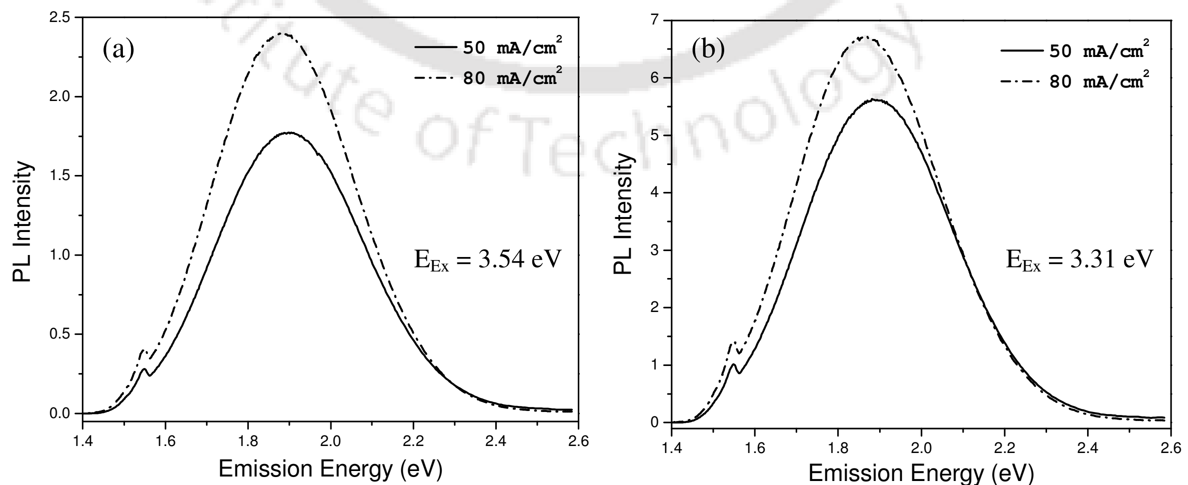

Figure 5.12 Measured PL of aged PS prepared by constant current anodization of c-Si wafers of resistivity 1–10 Ω cm using 50 and 80 mA/cm^2 anodization current densities.

intensity of luminescence increases with anodization current density. In the earlier discussions, I have introduced one of the many parameters on which the intensity of luminescence is related – the electronic density of states of the chemisorbed species at pore walls. Although the knowledge of electronic density of emission states is crucial, it is merely useful for the intensity of luminescence inside the material. In practice, the intensity of luminescence is measured with the detector kept outside the material. So, it is necessary to consider a few more parameters in order to understand the effect of anodization current density on the intensity of luminescence.

In Chapter 4, it has been shown that when the electrolyte concentration and the wafer doping are fixed, an increase in anodization current density decreases the effective refractive index n_{eff}. In the same chapter, the decrease in n_{eff} with anodization current density is interpreted as due to the increase in porosity. The increase in porosity is basically, from the microstructure viewpoint, due to the widening of pore diameter. In the following, the effect of these changes on the intensity of luminescence is elucidated.

The widening of pore diameter increases the internal surface area of the material. This provides room for the chemisorption of more chemical species on the exposed Si surfaces. On these lines, the enhancement of luminescence with anodization current density seems obvious, but yet the enhancement is only internal. The argument is still lacking to convince, the increase in current density increases the luminescence outside the material.

The Si in PS bears the bulk optical properties of c-Si. As the bandgap of c-Si is 1.12 eV, although indirect, it does significantly absorb the radiations below the bandgap energy. Surprisingly, the PL of PS is also in the region of medium absorption of Si. The measured luminescence is only those radiations that have overcome the absorption of Si in PS. With the increase in anodization current density, the Si volume fraction is decreased and thereby, the absorption of the emitted radiation is also reduced. Hence, the intensity of luminescence has enhanced with anodization current density.

5.7 SUMMARY

In summary, an extensive study on the PL of PS towards an understanding of the basic mechanism of the phenomenon is presented. The basic mathematical relation for the analysis of PLE spectrum is corrected to incorporate the spectral dependence of the

TH-1094_04612102

reflectance of the material. With the corrected mathematical relation, it is found that the PLE spectrum of PS has very similar spectral features as that of the absorption of bulk c-Si. From the similarity between the spectra, it is identified that the efficient visible PL in PS is not due to the quantum confinement of excitons. Following, the microstructure of PS with an explicit show up of different chemical species in PS matrix is presented. Then, from the changes in luminescence intensity and peak centre with aging and the corresponding changes in the chemisorbed species in PS matrix, the PL in PS is ascribed to the electronic energy states formed by the chemisorbed species.

After the proposal of the mechanism for the PL, a few common observations in the PL of PS like broad spectral feature, blue-shift of the PL peak centre with excitation energy, luminescence enhancement with anodization current density, etc. are explained on the lines of the proposed mechanism.

5.8 REFEREBCES

[1] V. Lehmann, and U. Gösele, Appl. Phys. Lett. **58**, 856 (1991)

[2] X. L. Zheng, W. Wang, and H. C. Cheng, Appl. Phys. Lett. **60**, 986 (1992)

[3] Z. Y. Xu, M. Gal, and M. Gross, Appl. Phys. Lett. **60**, 1375 (1992)

[4] W. Zhou, H. Shen, J. F. Harvey, R. A. Lux, M. Dutta, F. Lu, C. H. Perry, R. Tsu, N. M. Kalkhoran, and F. Namavar, Appl. Phys. Lett. **61**, 1435 (1992)

[5] M. S. Brandt, H. D. Fuchs, M. Stutzmann, J. Weber, and M. Cardona, Solid State Commun. **81**, 307 (1992)

[6] S. M. Prokes, W. E. Carlos, and V. M. Bermudez, Appl. Phys. Lett. **61**, 1447 (1992)

[7] R. T. Collins, M. A. Tischler, and J. H. Stathis, Appl. Phys. Lett. **61**, 1649 (1992)

[8] S. M. Prokes, O. J. Glembocki, V. M. Bermudez, R. Kaplan, L. E. Friedersdorf, and P.C. Searson, Phys. Rev. B **45**, 13788 (1992)

[9] R. P. Vasquez, R. W. Fathauer, T. George, A. Ksendzov, and T. L. Lin, Appl. Phys. Lett. **60**, 1004 (1992)

[10] J. M. Perez, J. Villalobos, P. McNeill, J. Prasad, R. Cheek, J. Kelber, J. P. Estrera, P. D. Stevens, and R. Glosser, Appl. Phys. Lett. **61**, 563 (1992)

[11] P. Deák, M. Rosenbauer, M. Stutzmann, J. Weber, and M. S. Brandt, Phys. Rev. Lett. **69**, 2531 (1992)

[12] M. S. Brandt, H. D. Fuchs, M. Stutzmann, J. Weber, and M. Cardona, Solid State Commun. **81**, 307 (1992)

[13] O. K. Andersen, and E. Veje, Phys. Rev. B **53**, 15643 (1996)

[14] L. Wang, M. T. Wilson, and N. M. Haegel, Appl. Phys. Lett. **62**, 1113 (1993)

[15] V. B. Pikulev, S. N. Kuznetsov, Y. E. Gardin, and V. A. Gurtov, J. Porous Mater. **7**, 253 (2000)

[16] X. H. Fang, M. X. Liao, Y. Gu, and X. L. Wu, phys. stat. sol. (a) **202**, 1818 (2005)

[17] P. Y. Yu and M. Cardona, Fundamentals of Semiconductors, 3rd ed. (Springer, Berlin, 1996) p. 370

[18] P. Y. Yu and M. Cardona, Fundamentals of Semiconductors, 3rd ed. (Springer, Berlin, 1996) p. 369

[19] U. Schmid, N. E. Christensen, and M. Cardona, Phys. Rev. B **41**, 5919 (1990)

[20] P. Y. Yu and M. Cardona, Fundamentals of Semiconductors, 3rd ed. (Springer, Berlin, 1996) p. 349

[21] H. Yorikawa and S. Muramatsu, Appl. Phys. Lett. **71**, 644 (1997)

[22] P. Y. Yu and M. Cardona, Fundamentals of Semiconductors, 3rd ed. (Springer, Berlin, 1996) p. 225

TH-1096_04612102

CHAPTER

6

STUDIES ON RAMAN SCATTERING IN POROUS SILICON

In Chapter 5, the optical absorption of Si in PS is identified to be same as that of the bulk c-Si. This is a strong evidence that the size of Si regions in PS is large enough for any observable quantum confinement effects. However, although less probable, when the electronic wavefunctions overlap with the neighbouring Si regions, the tunnelling of electrons through the pores could also suppress the effects of quantum confinement, and the optical absorption of Si in PS would be same as that of the bulk c-Si. To identify whether or not the size of Si regions is in the realm of realization of quantum confinement effects, the technique must be sensitive only to the size of Si regions and not to the overlapping of electronic wavefunctions. Raman scattering (RS) is one such technique that could provide a direct evidence on the size of Si regions for the realization of quantum confinement effects [1-3].

Raman scattering (RS) in PS has extensively been investigated ever since the discovery of PL from the material [4-10]. For nearly two decades, despite several controversial interpretations for PL of PS, the interpretation of RS is essentially the same – optical phonon confinement in small Si crystallites [4, 10-12]. Often in the literature, the results of RS are presented to substantiate the quantum confinement model of PL of PS [13-16].

TH-1099_04612102

However, the spectral features of RS are not only sensitive to the crystallinity, but also to the temperature [17-19]. When there is a temperature gradient in the sampling spot, the collected RS spectrum [20] would have very similar features as that of the quantum confinement of phonons. The temperature gradient in the sampling spot is unintentional with the use of high power lasers to record the RS. With the advent of micro-Raman technique, even at moderate laser powers, due to very high fluence, there could be laser heating of the focus spot [4].

This chapter presents a systematic study on the variation of RS of PS with B-doping concentration and anodization current density with less or no laser heating of the focus spot. The Fano effect, which is an interference phenomenon between the processes from discrete and continuum quantum eigenstates, is so far addressed only in bulk c-Si. In this chapter, the Fano effect is shown to exist even in PS. The variation of Fano pattern with B-doping concentration and anodization current density is discussed in detail in this chapter.

6.1 ONE-PHONON RAMAN SCATTERING IN PS

A typical RS spectrum of an undoped bulk c-Si is shown in Fig. 6.1. The intense, narrow and nearly a Lorentzian profile at around 521 cm^{-1} is the only one-phonon RS of bulk c-Si [21-24]. The symmetry components of the one-phonon RS of c-Si are Γ_1, Γ_{12} and

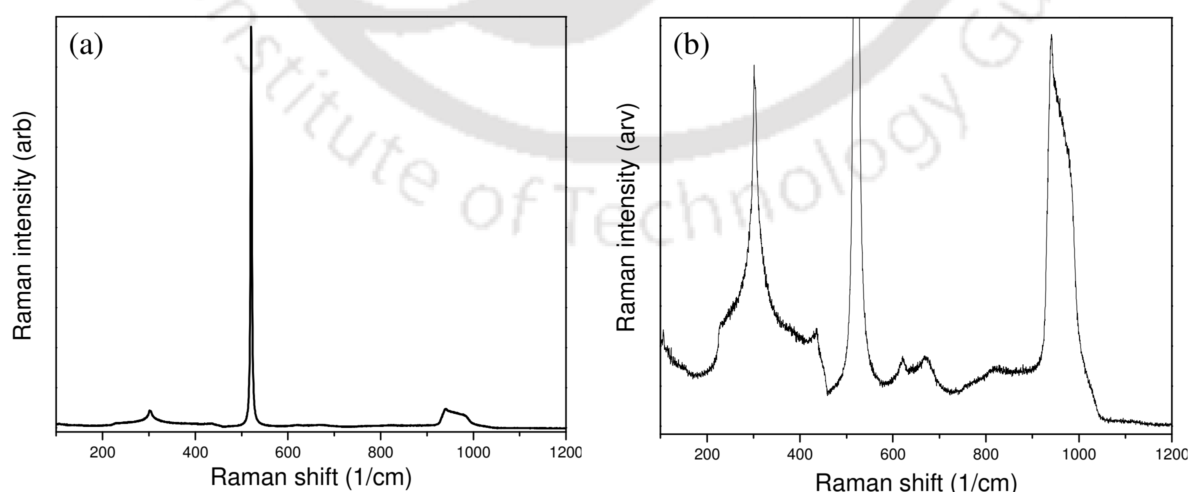

Figure 6.1 Measured Raman scattering spectrum of a bulk c-Si of resistivity >50 Ω cm recorded under 632.8 nm laser excitation (a) the complete spectrum and (b) closer view of the multiphonon RS.

TH-1098_04612102

$\Gamma_{25'}$ [24]. Of these symmetry components, $\Gamma_{25'}$ is the dominant contributor to the one-phonon RS intensity [24]. For this reason, in the literature, the one-phonon Raman scattering is sometimes denoted as $\Gamma_{25'}$ component of the one-phonon RS even though no polarization optics is used to select the desired component [25, 26]. However, in the present thesis, the denotation of one-phonon RS does not accompany the symmetry components as no polarization optics is used in the measurement.

Only in bulk c-Si, the one-phonon RS is narrow, symmetric and centred at 521 cm^{-1}. The spectral features are strongly affected with the changes in the crystalline structure of the material [1-3, 26]. A red shift accompanied with a spectral asymmetry in the broadening of one-phonon RS, in the absence of non-uniform heating, is a clear indication of the presence of low dimensional c-Si structures [1-3]. A typical one-phonon RS of low dimensional c-Si structure and bulk c-Si are shown in Fig. 6.2.

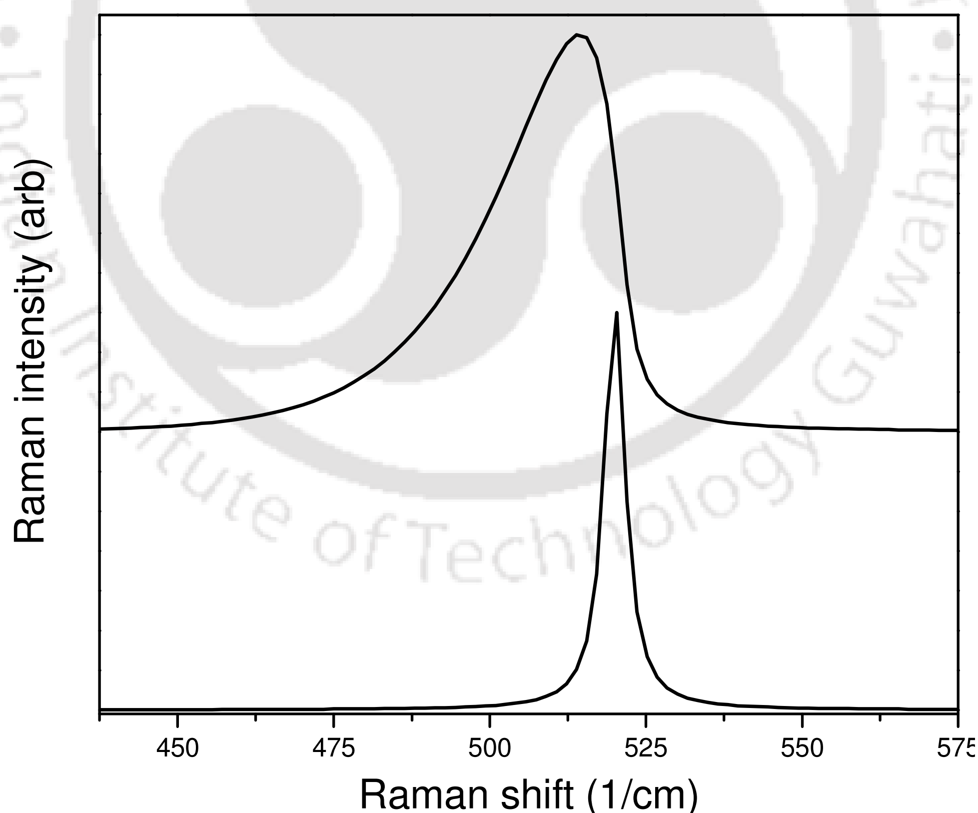

Figure 6.2 A comparison of one-phonon RS spectral features of a nano-crystalline Si (top) with the bulk c-Si (bottom). The RS of nano-crystalline Si is simulated for 2.75 nm crystallite using the relation given in Ref [2].

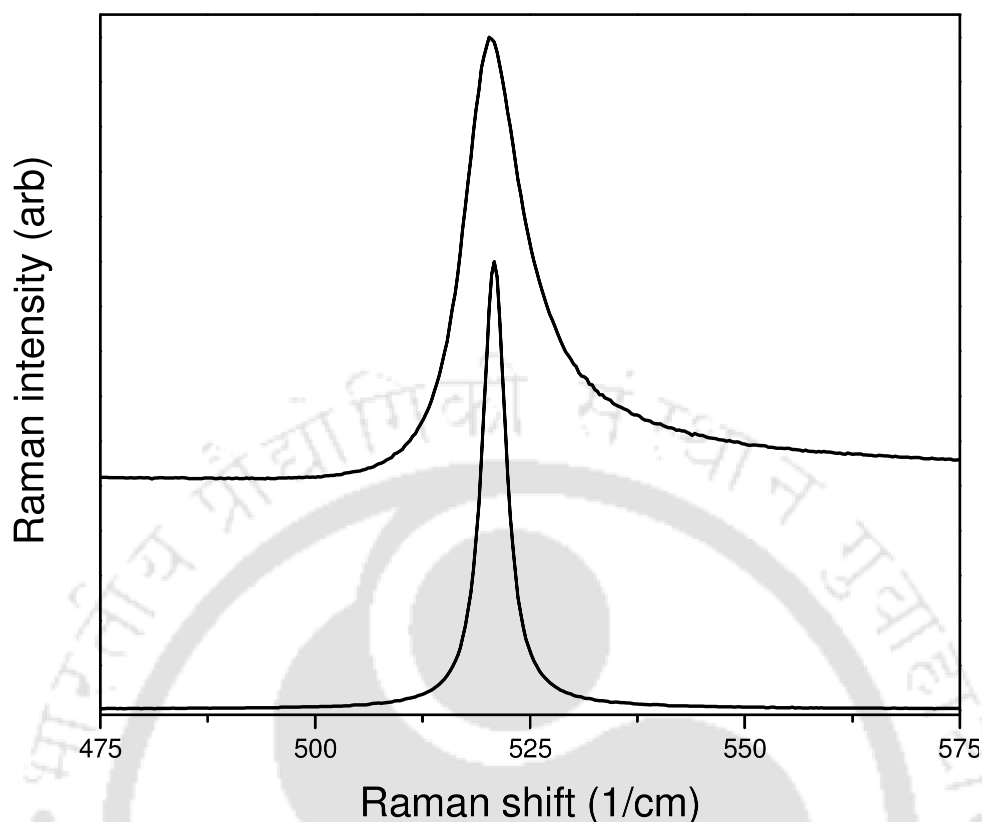

Figure 6.3 A comparison of the spectral features of RS in high (top) and low (bottom) B-doped c-Si wafers. The resistivities of high and low B-doped c-Si wafers are 0.001–0.005 and >50 Ω cm, respectively. The spectra are recorded under 632.8 nm laser excitation.

The spectral features of one-phonon RS are also affected by the B-doping concentration [27-29]. Figure 6.3 shows the effect of B-doping concentration on one-phonon RS of bulk c-Si. The asymmetric line-shape of heavily doped c-Si is due to Fano effect [27-31]. The analysis of the asymmetry would be complicated when both Fano and quantum confinement effects coexist.

In the following, the discussions on the RS of PS are presented separately for PS prepared on low and high B-doping concentration wafers as the spectral features of RS are affected differently between low and high B-doped c-Si.

6.1.1 Low B-doping concentration wafers (ρ >0.1 Ω cm)

Figures 6.4 and 6.5 show the measured one-phonon RS of PS prepared on low B-doping concentration wafers using various anodization current densities and their

TH-1099_04612102

respective bulk c-Si wafers. All the spectra are normalized to unity for easy comparison of the spectral features. Also, the spectra on any particular B-doping concentration wafer are vertically displaced for the clear visibility of the spectral features in the one-phonon RS.

The one-phonon RS on c-Si wafers of different resistivities are all identical, which would mean that the Fano effect is completely negligible on these wafers, at least under 632.8 nm laser excitation. It is also observed that the normalized spectra in Figs. 6.4(b), 6.4(d), 6.5(b) and 6.5(d) fall on each other irrespective of the anodization current density. This would indicate that the one-phonon RS of Si in PS is identical to the respective bulk

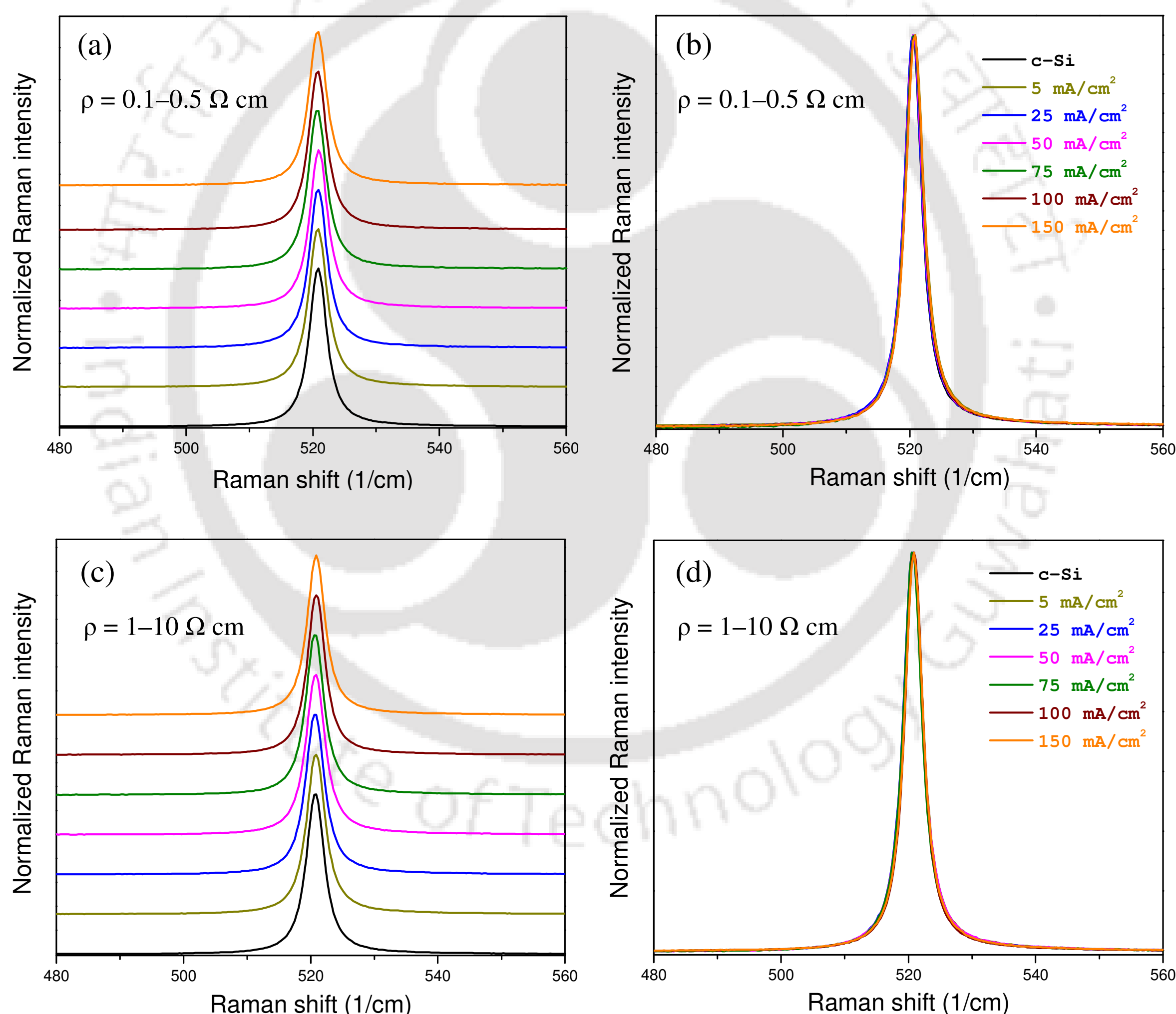

Figure 6.4 Measured one-phonon RS of both PS prepared using many different anodization current densities and the respective bulk c-Si wafer of resistivities 0.1–0.5 and 1–10 Ω cm with (a) and (c) vertically shifted and (b) and (d) no vertical shift. The spectra are recorded under 632.8 nm laser excitation, and are normalized to unity.

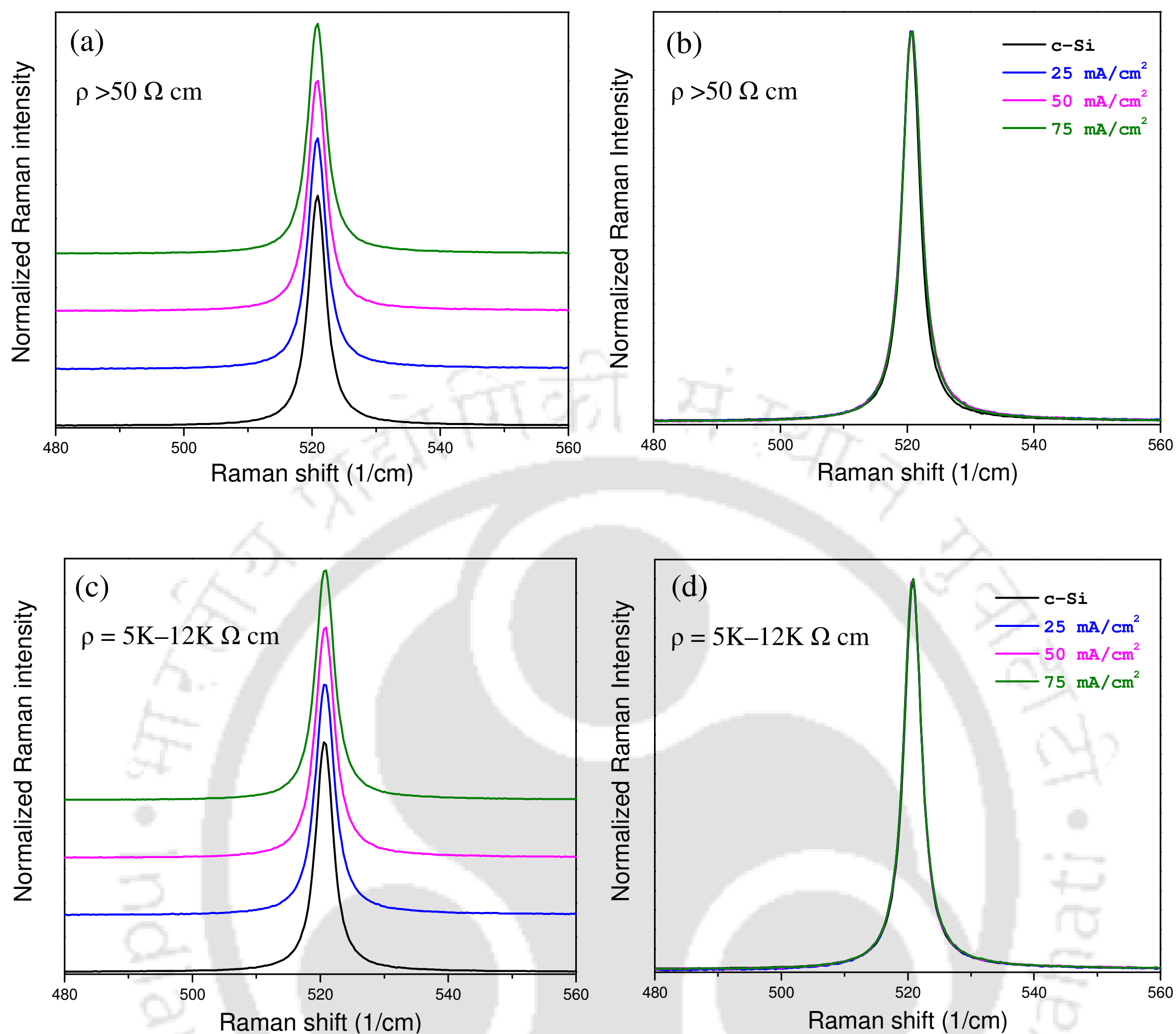

Figure 6.5 Measured one-phonon RS of both PS prepared using many different anodization current densities and the respective bulk c-Si wafer of resistivities >50 and 5K–12K Ω cm with (a) and (c) vertically shifted and (b) and (d) no vertical shift. The spectra are recorded under 632.8 nm laser excitation, and are normalized to unity.

c-Si and is not affected by the changes in the microstructure introduced by the anodization current density. The latter observation provides a direct evidence that the size of Si regions in PS must be sufficiently large for any observable quantum confinement effect. This observation, although contradicts the existing scenario [4-16], corroborates the inference from PLE measurements presented in Chapter 5. However, as the PS layers under investigation are very thin (< 3 μm), there is a possibility for a suspicion that the recorded spectra are probably not from PS, but, from the underneath bulk c-Si.

TH-1099_04612102

Figure 6.6 shows the variation of RS intensity of PS with anodization current density for low B-doping concentration wafers. It is observed in Fig. 6.6 that the RS intensity in PS is several times greater than the bulk c-Si and has a decreasing trend with the increasing anodization current density for all B-doping concentration wafers. These features in RS intensity ensure that the recorded spectra are at least not from the underneath bulk c-Si. If spectra had been from the underneath bulk c-Si, the RS intensity would have lowered due to the intensity losses in PS medium, and with increasing anodization current density, the trend would have been opposite as the effective refractive index decreases. Yet these arguments do not bear evidence that the recorded spectra are

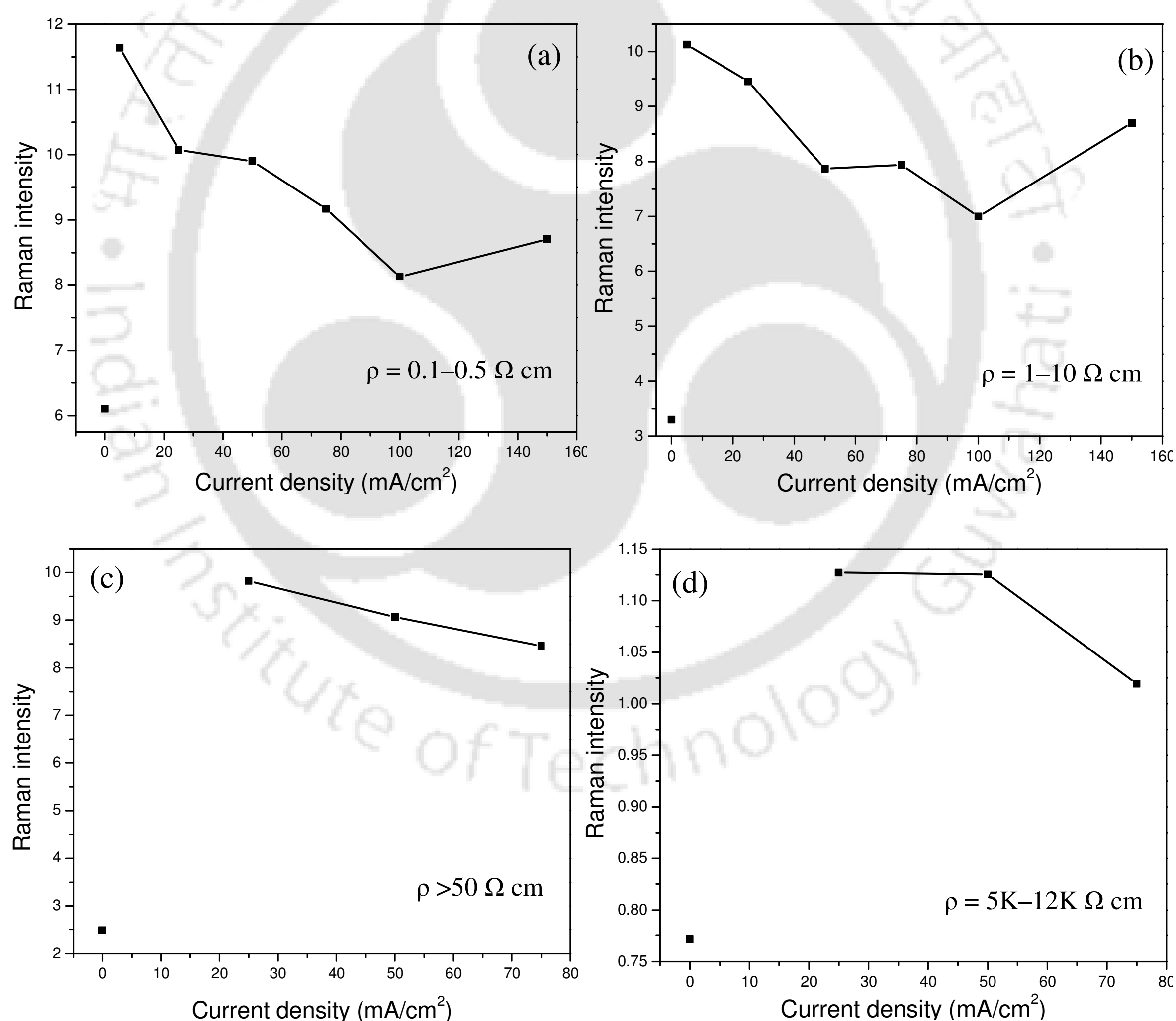

Figure 6.6 Variations of the peak intensity of one-phonon RS of PS with anodization current density for different wafer resistivities. The 0 mA/cm^2 corresponds to the respective bulk c-Si wafers.

from PS layers only. In order to affirm that the recorded spectra in PS are predominantly from PS layers, the features in Fig. 6.6 are to be understood through the physical properties of PS.

The decrease of RS intensity with the increasing anodization current density can be understood as due to the decrease of number of Si atoms per unit volume. Although RS is phenomenally the result of the interaction of photons with phonons, the process is mediated by electrons when visible photons are used [32]. The incident photons are at first absorbed by electrons which in turn interact with phonons resulting in RS. The initial photon-electron interaction improves with the strength of optical absorption. In Chapter 5, it has only been shown that the spectral features of the optical absorption of Si regions in PS are same as that of the bulk c-Si for all anodization current densities and not the strength of optical absorption. The strength of optical absorption is influenced by anodization current density. An increase of anodization current density decreases the number volume density of Si atoms, and thus decreases the strength of optical absorption. Hence, the RS intensity has decreased with the anodization current density as shown in Fig. 6.6.

The other feature in Fig. 6.6 is the large enhancement of RS intensity of PS relative to bulk c-Si wafer despite the decrease of number volume density of Si atoms in PS. This seems counteracts the decreasing trend of RS intensity with the anodization current density. In actual, the large enhancement of RS intensity is only because of effective RS of incident photons in PS due to its composite nature. In bulk c-Si wafer, nearly 35 % of the incident photons are lost in the specular reflectance for 633 nm wavelength [33], and only the remaining fraction of the photons enters into the medium. However, in PS, as the (effective) refractive index is much lower than the bulk c-Si, a larger fraction of the incident photons enters into the PS medium. Also, in c-Si wafer, although the absorption is stronger, it is spatially extended, whereas, in PS, due to multiple reflections at the boundaries of the Si regions and also within the interfaces of the film, the absorption is spatially confined. Hence there is a large enhancement of RS intensity in PS.

6.1.2 High B-doping concentration wafers ($\rho < 0.05\ \Omega$ cm)

Figure 6.7 shows the measured one-phonon RS of PS prepared under various anodization current densities on high B-doping concentration wafers together the

TH-1099_04612102

respective bulk c-Si wafers. The spectra are normalized to unity to compare the changes in spectral features with the anodization current density relative to the respective bulk c-Si wafers.

The spectral line-shape of the bulk c-Si of high B-doping concentration wafers is itself asymmetric, and the asymmetry increases in PS with the increasing anodization current density. The changes in the asymmetric line-shape with anodization current density are more pronounced with the increasing B-doping concentrations. Also, the asymmetric line-shape and the peak position have very strong dependence on the wavelength of the

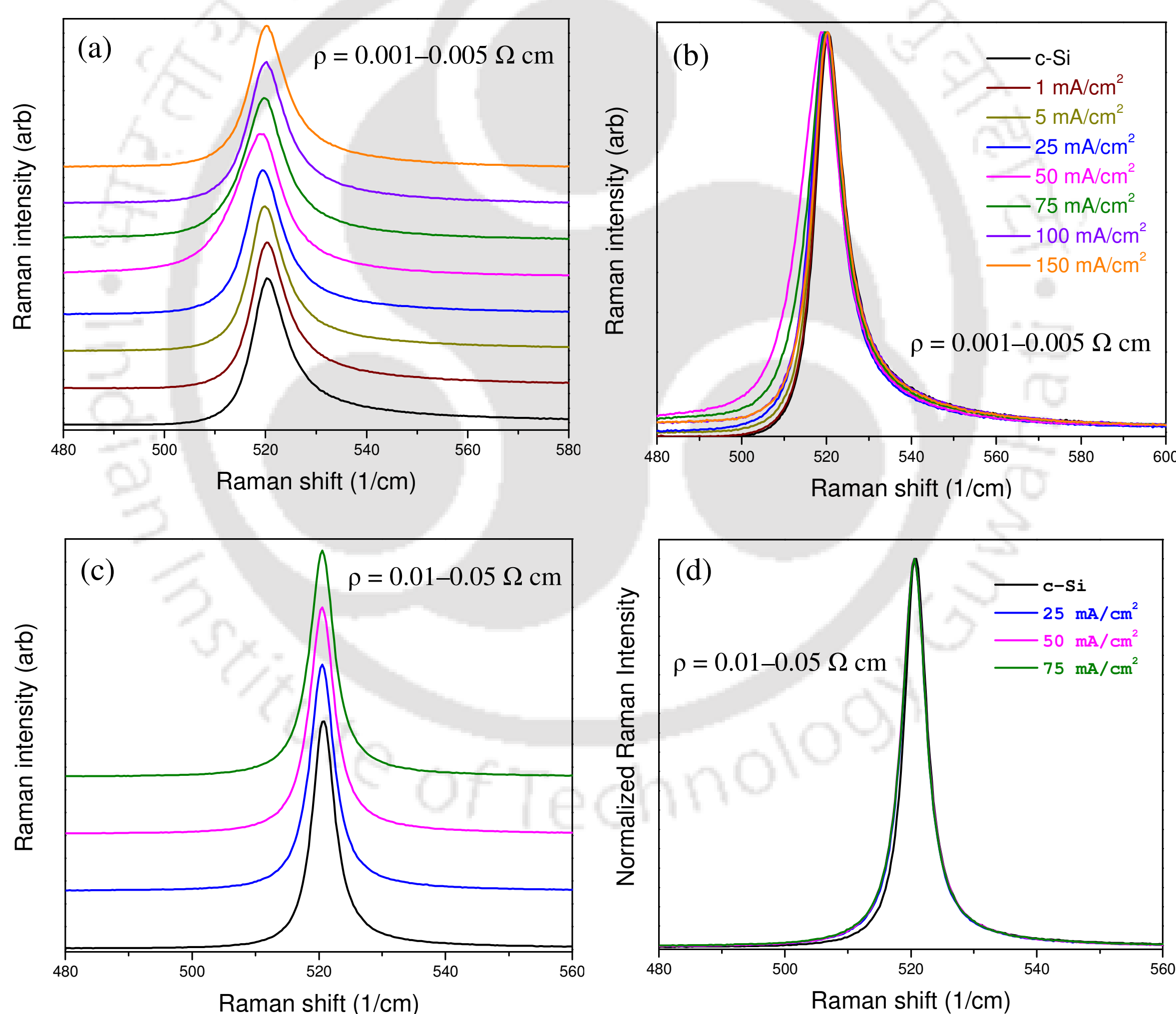

Figure 6.7 Measured one-phonon RS of both PS under many different anodization current densities and the respective bulk c-Si wafer of resistivities 0.001–0.005 and 0.01–0.05 Ω cm with 632.8 nm laser excitation, and are normalized to unity.

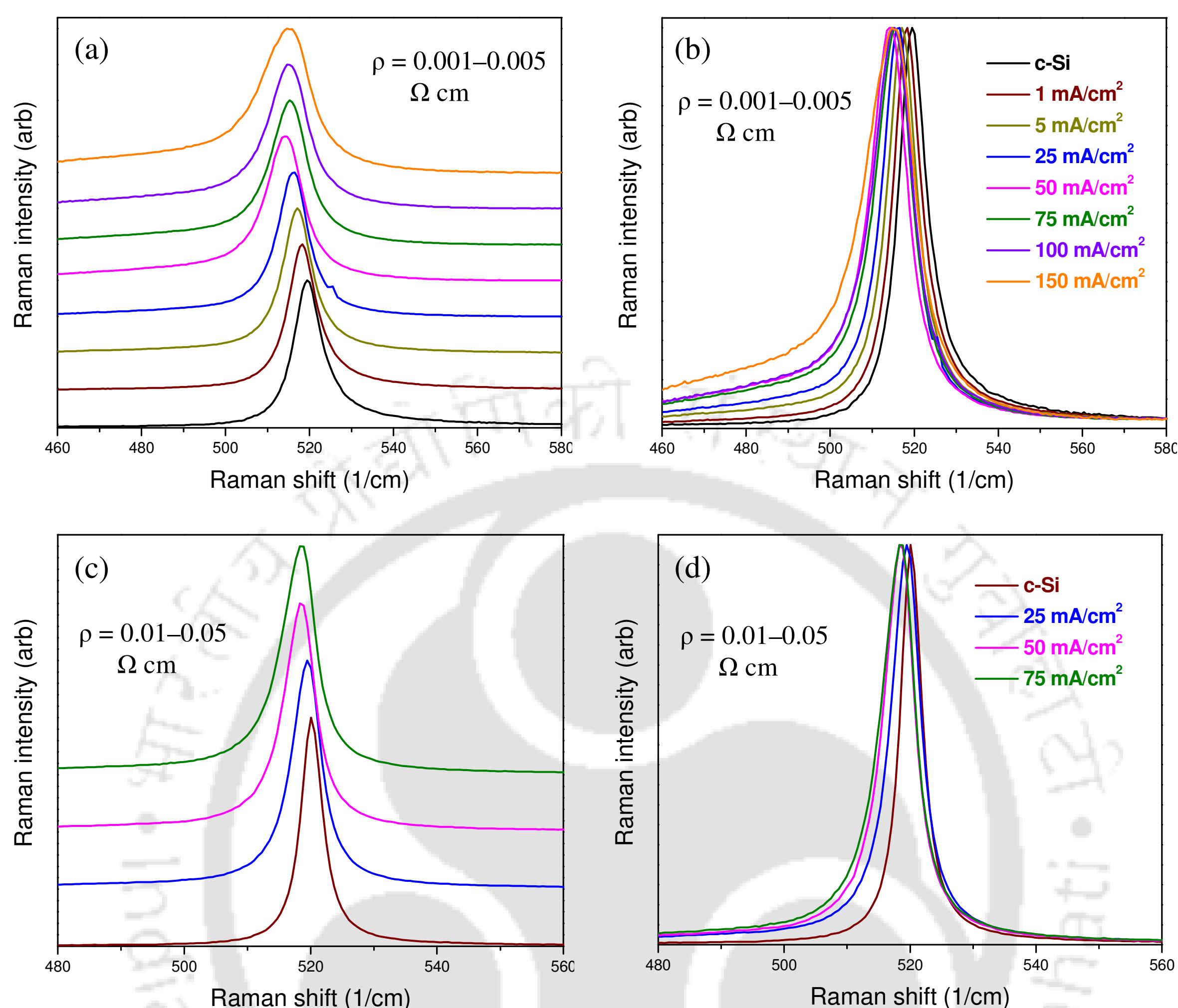

Figure 6.8 Measured one-phonon RS of both PS under many different anodization current densities and the respective bulk c-Si wafer of resistivities 0.001–0.005 and 0.01–0.05 Ω cm with (a) and (c) vertically shifted and (b) and (d) no vertical shift. The spectra are recorded under 488 nm laser excitation, and are normalized to unity.

exciting laser as can be seen on comparison of Fig. 6.7 with Fig. 6.8.

Based on these observations, it is inferred that the asymmetric spectral line-shape of PS is at least not because of the phonon confinement. If the asymmetry had been only due to phonon confinement, the wavelength of the exciting laser would not have affected the spectral line-shape. The asymmetry in the RS line-shape of PS only on high B-doping concentration wafers could possibly due to the Fano effect as in the respective bulk c-Si wafers. It is although possible that the Si regions in PS could have the optical properties of the respective bulk c-Si wafer, it has yet not been shown explicitly.

TH-1099_04612102

6.1.3 One-phonon RS peak intensity with B-doping concentration

It is an experimental fact that the peak intensity of the one-phonon RS varies with B-doping concentration. Figure 6.9(a) shows the variation of RS intensity with B-doping concentrations (resistivity) for the bulk c-Si wafer. Figure 6.9(b) shows the corresponding variations in PS prepared under 25, 50 and 75 mA/cm^2 anodization current densities. For all three anodization current densities, PS layers have shown similar variation in RS intensity. On comparison with bulk c-Si, there are some slight differences in the variations of RS intensity, in particular, at 50 Ω cm. At 50 Ω cm, the RS intensity of bulk c-Si is weaker than that of the neighbouring resistivities. However, in PS this feature is observed for 1–10 Ω cm resistivity. This is because the RS intensity in PS is influenced, in addition to the Si regions, by the microstructure and effective refractive index of the material. Despite of other influences, the general trend in the variation of peak intensity is still preserved in PS. This observation supports that the Si in PS retains the optical properties of the respective bulk c-Si wafer.

Prior to this work, as there is no report on the effect of B-doping concentration in the RS of PS, a detailed discussion of the line-shape asymmetry, in relation to the Fano effect, is presented in the following section.

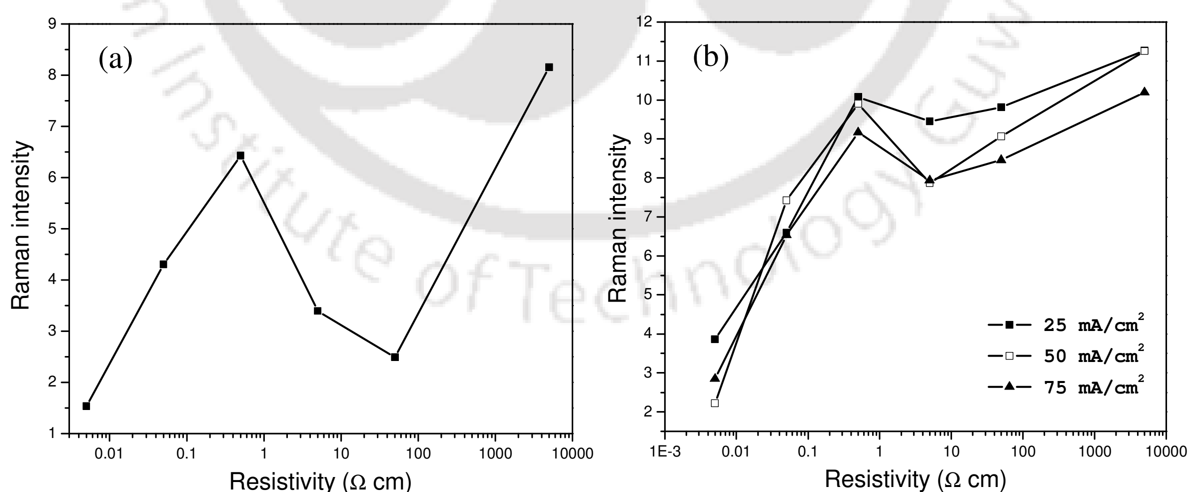

Figure 6.9 The variation of peak intensity of one-phonon RS of (a) bulk c-Si and (b) PS prepared using 25, 50 and 75 mA/cm^2 anodization current densities with wafer resistivity. The RS for both bulk c-Si and PS are recorded under 632.8 nm laser excitation.

6.2 FANO EFFECT

Fano effect, in general, is a quantum interference phenomenon between the processes from discrete and continuum quantum eigenstates [34]. The spectral line-shape of the discrete process is symmetric. The interference of the continuum process would result in the line-shape asymmetry of the discrete process. A simple mathematical relation for the line-shape asymmetry due to Fano effect can be given as [30, 31]

$$I = \frac{(q + \varepsilon)^2}{(1 + \varepsilon^2)} \tag{6.1}$$

where $\varepsilon = (\omega - \Omega)/\Gamma$, in which, ω and Ω, are the measured and critical frequency, respectively. The parameters q^2 and Γ have their physical meanings as the ratio of scattering probability of discrete to continuum and the square matrix element of the coupling between discrete and continuum eigenstates, respectively. In the analysis of line-shape asymmetry through Eq. (6.1), q and Γ are generally the fitting parameters.

Extensive studies on the Fano effect in the RS of bulk c-Si already exist in the literature [30, 31]. In this section, prior to discuss the line-shape asymmetry of PS, the Fano patterns in the respective bulk c-Si wafers are discussed.

6.2.1 Fano effect in RS of bulk c-Si

In the RS of c-Si, the Fano effect is due to the interference of electronic (continuum) and phononic (discrete) RS processes [27-31, 35].

The valance band of p-type bulk c-Si consists of heavy, light and spin-orbit-split hole bands. Figure 6.10 shows a typical one dimensional or isotropic band structure of a p-type semiconductor. The electronic RS is due to the transition of an electron from the light hole band to the heavy hole band via an intermediate conduction band state [31, 35]. This electronic RS produces a continuum that extends between the energies $\hbar\Omega_m$ and $\hbar\Omega_M$. For the bulk c-Si, the lower cut-off energy $\hbar\Omega_m$ is the smallest separation between the light and heavy hole bands at the Fermi wavevector k_F, which is $\leq \frac{2}{3}\Delta_0$, where Δ_0 = 44 meV is the spin-orbit splitting. The true band structure of c-Si is anisotropic. Owing to the anisotropy, the continuum extends to very high energies due to the flatness of the heavy-hole band in certain directions in the ***k*** space. The phononic RS, on the other hand, is the creation or annihilation of a phonon at the centre of the Brillouin zone with a virtual intermediate state

TH-1098_04612102

of an electron with its initial and final state unaltered [36]. That is to say the phononic RS is the discrete one-phonon RS which is about 65 meV for the bulk c-Si.

As the electronic RS continuum overlaps in energy with the phononic RS, there is an interference between the two RS processes which is the Fano effect. Due to this interference effect, the symmetric one phonon RS, which is observed in low B-doping concentration bulk c-Si, is asymmetrised.

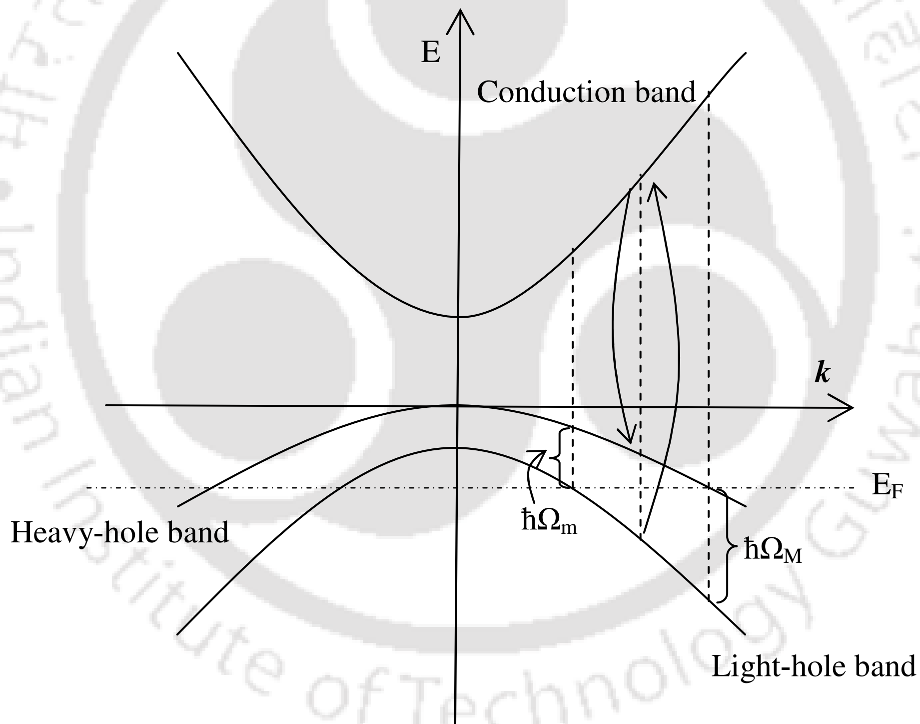

Figure 6.10 A typical one-dimensional or isotropic band structure of a p-type semiconductor close to Brillouin zone centre. The Fermi energy E_F is in the valance band. The incident photon of frequency ω excites an electron from the light-hole band to the conduction band. The excited electron into the conduction band de-excites to heavy-hole band by the emission of a scattered photon ω′. These intervanlance band electronic transitions give Raman spectrum with low and high frequency cut-offs denoted as Ω_m and Ω_M, respectively.

Figure 6.11 show the measured RS of bulk c-Si for various B-doping concentrations under 632.8 and 488 nm excitation wavelengths. All the spectra are normalized to unity for easy comparison of spectral features. The background signal in the spectra, as can be seen in Figs. 6.11(b) and (c), is mainly due to inter-valance band electronic RS [37], and increases with the B-doping concentration. The Fano line-shape of bulk c-Si is affected by both B-doping concentration and the wavelength of exciting laser as can be seen Figs. 6.11(a) and (c).

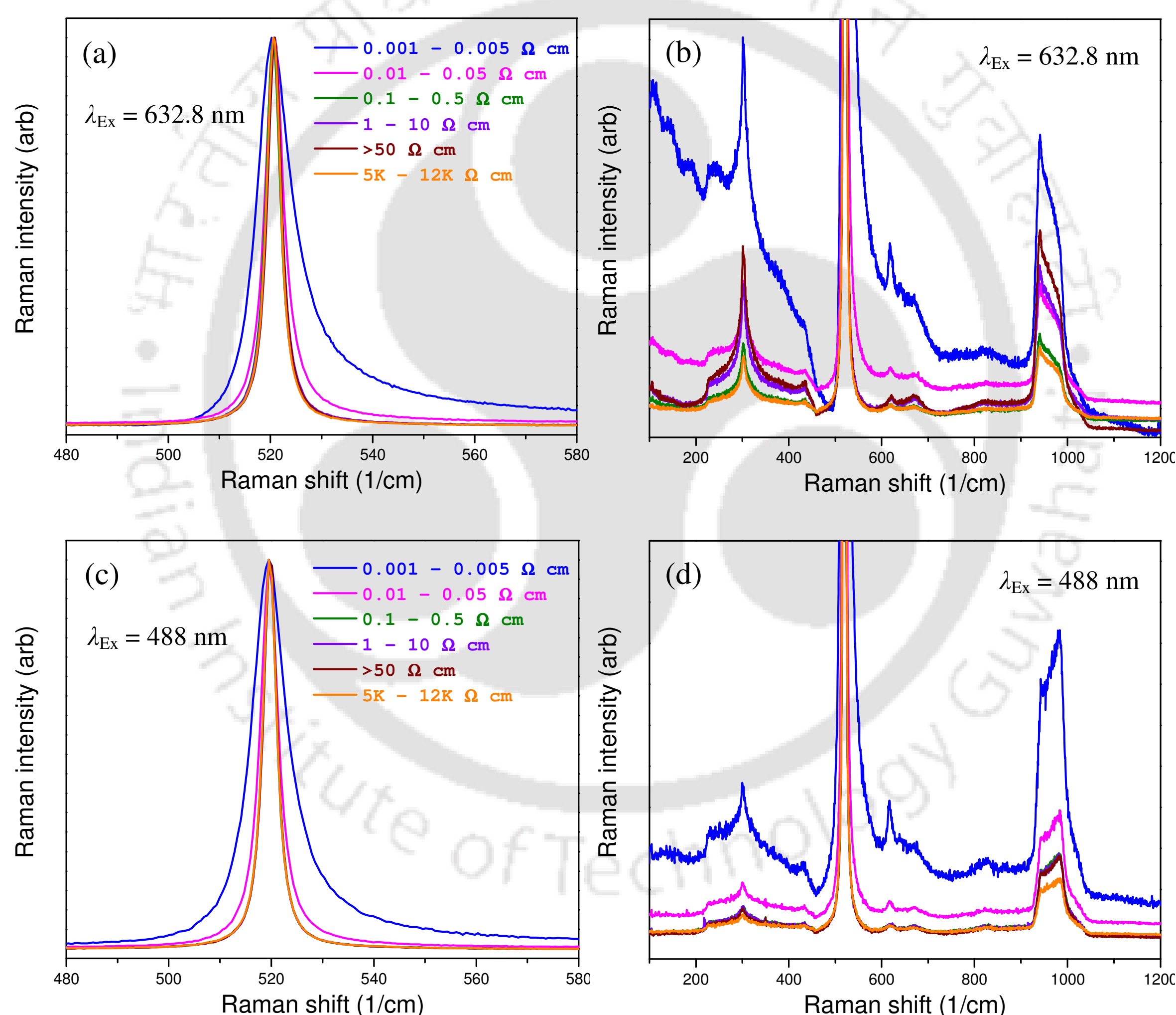

Figure 6.11 Measured RS of bulk c-Si wafers for several B-doping concentrations under the laser excitations 632.8 nm (a) closer view of the line-shape asymmetry of one-phonon RS and (b) closer view of the background inter-valance band electronic RS and the mulitphonon RS and 488 nm (c) closer view of the line-shape asymmetry of one-phonon RS and (b) closer view of the background inter-valance band electronic RS and the mulitphonon RS.

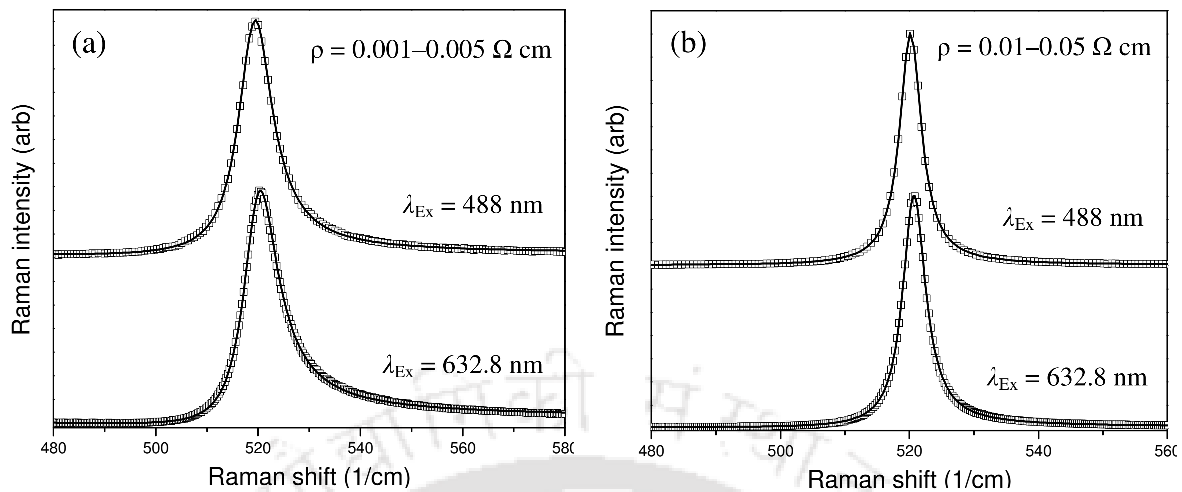

Figure 6.12 Measured (discrete) and fit (continuous) of the Fano pattern of c-Si wafers of resistivities (a) 0.001–0.005 Ω cm and (b) 0.01–0.05 Ω cm for 488 nm (top) and 632.8 nm (bottom) laser excitations.

Table 6.1 Values of q and Γ that fit the Fano line-shape of the measured RS of bulk c-Si wafer of resistivities 0.001–0.005 and 0.01–0.05 Ω cm for 488 and 632.8 nm excitations shown in Fig. 6.12.

Resistivity (Ω cm)	q		Γ	
	488 nm	632.8 nm	488 nm	632.8 nm
0.01–0.05	76.75	29.14	2.05	2.15
0.001–0.005	15.17	6.77	4.08	4.13

For a quantitative understanding of the effects of B-doping concentration and exciting laser wavelength, the Fano line-shapes of bulk c-Si wafers are fitted with the Eq. (6.1). The goodness of the fit can be seen in Fig. 6.12, and the corresponding fitting parameters for the spectra are given in Table 6.1. The variations of q and Γ with B-doping concentrations and excitation wavelength are similar to that reported in the literature [30, 31]. The increase of Γ with the increasing B-doping concentration signifies that the coupling of

electronic RS with phononic RS increases with the increasing B-doping concentration. However, with the excitation wavelength no significant changes in Γ are observed. Based on this observation, it is inferred that the coupling of the processes could be an inherent material property. The parameter q, as it signifies the ratio of scattering probability of phononic RS to electronic RS, is decreasing with increasing B-doping concentration. Also, q decreases with the increasing excitation wavelength. This is because when the scattering frequency is farther from the energy bandgap of the material, the probability of phononic RS decreases relative to the electronic RS.

6.2.2 Fano effect in RS of PS

From the variation in Raman intensity with the wafer resistivity, as shown in Fig. 6.9, it is inferred that the Si in PS retain the RS properties of the respective bulk c-Si wafer. Also, with the line-shape asymmetry in the RS of PS observed only in PS prepared on high B-doping concentration c-Si wafers, it is believed that the line-shape asymmetry in the RS of PS is due to the Fano effect.

Figure 6.13 shows the measured RS of PS prepared on various B-doping concentration c-Si wafers with many different anodization current densities under 488 nm laser excitation wavelength. Under this excitation wavelength, the line-shape asymmetry is observed even for PS prepared on moderately B-doped (0.1–0.5 and 1–10 Ω cm) c-Si wafers, in which, the respective bulk c-Si wafers itself show no asymmetry. The line-shape asymmetry in the RS of PS gradually decreases with the decrease of B-doping concentration, and is completely absent in PS prepared on very low B-doping concentration wafer (>50 Ω cm). These variations in the line-shape asymmetry with the B-doping concentrations are similar to that observed in bulk c-Si wafers. This observation further supports the claim that the line-shape asymmetry in the RS of PS is due to the Fano effect.

However, the line-shape asymmetries of RS of PS as shown in Figs. 6.7 and 6.13 are different from the respective bulk c-Si wafer and strongly influenced with the anodization current density. There could possibly two reasons for these observations: (i) the electromagnetic radiations are strongly absorbed by the Si regions in PS due to its composite nature and (ii) the changes in the B-doping concentration as the Si regions in PS are nearly depleted of holes in the process of anodization.

TH-1099_04612102

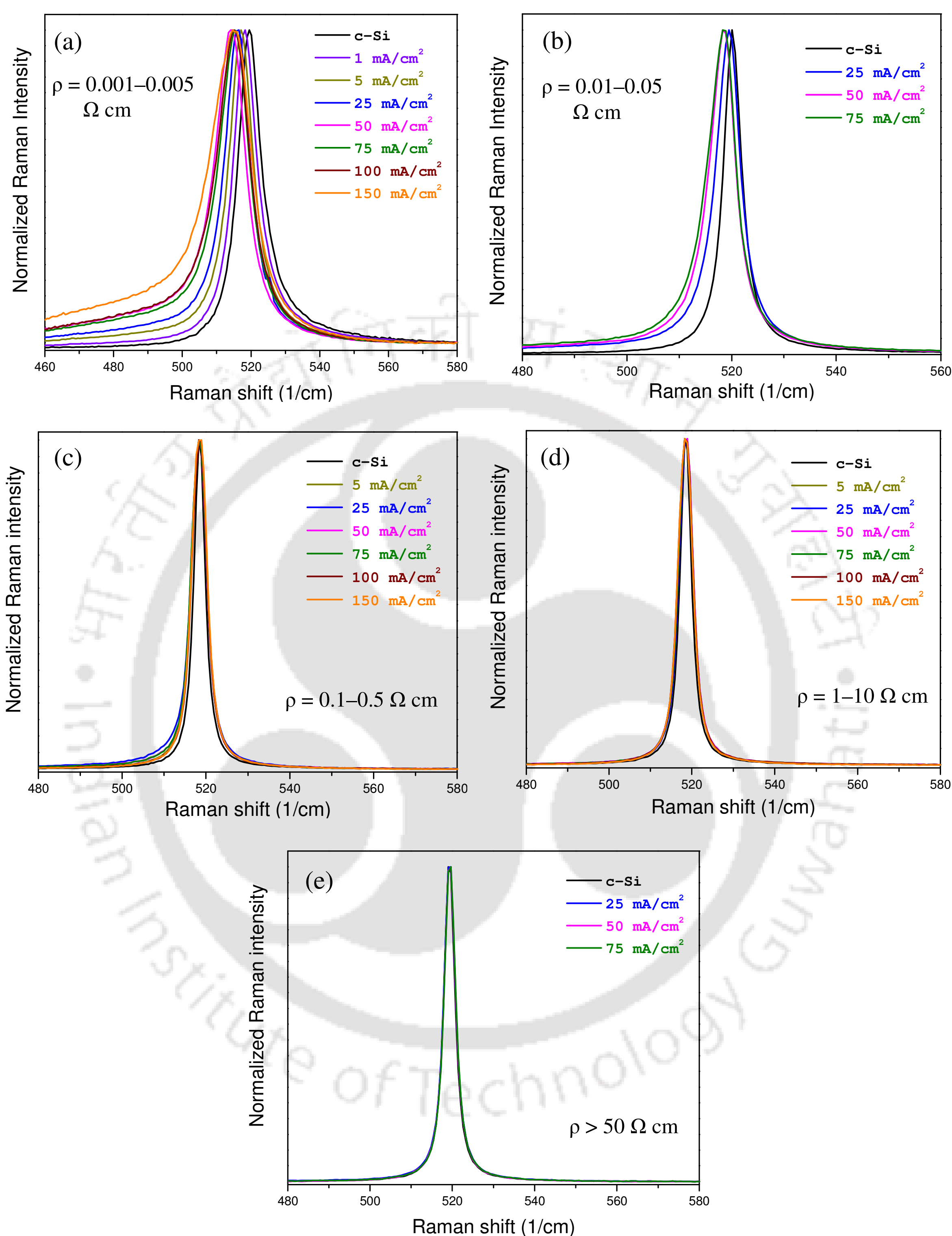

Figure 6.13 Measured one-phonon RS of both PS under many different anodization current densities and the respective bulk c-Si wafer of resistivities (a) 0.001-0.005 Ω cm (b) 0.01-0.05 Ω cm (c) 0.1-0.5 Ω cm (d) 1-10 Ω cm and (e) >50 Ω cm. The spectra are recorded under 488 nm laser excitation, and are normalized to unity.

The line-shape asymmetry in the RS of PS is fitted with the Fano function of Eq. (6.1). The goodness of the fit could be seen in Fig. 6.14 for the PS prepared on the c-Si wafers of resistivity 0.01–0.05 Ω cm under 488 and 632.8 nm excitation wavelengths. Table 6.2 gives the values of the fitting parameters to the measured spectra in Fig. 6.14 and also for the line-shape asymmetry in the RS of PS prepared on the c-Si wafers of resistivities 0.001–0.005 and 0.1–0.5 Ω cm under 488 and 632.8 nm excitation wavelengths.

The parameter Γ, even in PS, is dependent only on the doping concentration, and is very nearly the same as that of the respective bulk c-Si wafer. A small unsystematic variation of Γ with the anodization current density observed for all three doping concentrations could be the fitting error. The parameter q, on the other hand, in addition to its dependence on the doping concentration, is strongly dependent on the anodization current density, and even changes sign with the excitation wavelength. The change of sign in q has been found even for the bulk c-Si, but only for the wavelength well above the direct bandgap energy of c-Si [31]. The authors of Ref. [31] have given two possible explanations for this feature: (i) the change of c-Si band structure from bulk to surface bands and (ii) the significant contributions from the full anisotropic band structure for inter-valance band electronic transitions when above the critical points. In the case of PS, the former explanation could

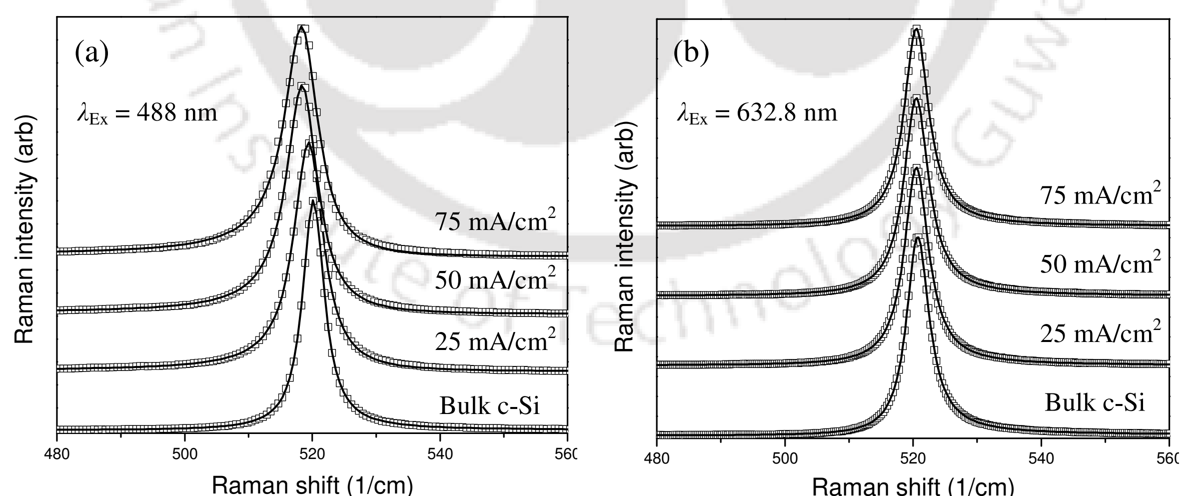

Figure 6.14 Measured (discrete) and fit (continuous) of the line-shape asymmetry of RS of both PS and the respective bulk c-Si wafer of resistivity 0.01-0.05 Ω cm under the excitation wavelengths (a) 488 nm and (b) 632.8 nm. The line-shape asymmetry is fitted with the Fano function of Eq. (6.1).

TH-1099_04612102

Table 6.2 The best fit values of q and Γ for the asymmetric line-shape of PS prepared on c-Si wafers of resistivities 0.001–0.005, 0.01–0.05 and 0.1–0.5 Ω cm under 488 and 632.8 nm excitation wavelengths. The 0 mA/cm^2 anodization current density corresponds to the respective c-Si wafers.

Resistivity (Ω cm)	Anodization current density (mA/cm^2)	q		Γ	
		488 nm	632.8 nm	488 nm	632.8 nm
0.001–0.005	0	15.17	6.77	4.08	4.13
	1	29.02	7.13	4.12	4.16
	5	-103.89	8.79	4.33	4.07
	25	-22.36	11.74	4.60	4.28
	50	-10.70	937.05	5.55	5.63
	75	-12.31	27.72	5.54	4.86
	100	-11.02	13.04	6.07	4.45
	150	-8.12	13.80	7.81	4.35
0.01–0.05	0	76.75	29.14	2.05	2.15
	25	-30.45	77.96	2.77	2.30
	50	-23.00	76.86	2.96	2.36
	75	-17.13	106.46	3.20	2.32
0.1–0.5	0	353.39	---	1.57	---
	5	-137.00	---	2.03	---
	25	-40.30	---	2.12	---
	50	-69.38	---	2.02	---
	75	-67.73	---	2.06	---
	100	-121.73	---	1.97	---
	150	-157.11	---	2.04	---

fit well. It is an obvious fact that the surface atoms are more in PS than in the c-Si wafer. With the increase of anodization current density, the number of surface atoms in PS increases from the c-Si wafer value, reaches to a critical value, and then decreases slowly. The variations in q for PS prepared on 0.001–0.005 Ω cm resistivity c-Si wafer with the anodization current density are similar to that of the number of surface atoms when recorded under 632.8 nm excitation wavelength.

In summary, the line-shape asymmetry of RS of PS prepared on doped c-Si wafers is due to the Fano effect. The coupling between the phononic and electronic RS is same as that of the respective bulk c-Si wafers. However, as the surface atoms are increasingly dominant in PS, the inter-valance band electronic RS is via surface bands.

6.3 SUMMARY

To summarize, a systematic study on the RS of PS with B-doping concentration and anodization current density variations is presented. The RS measurements reported in this thesis are preformed with low laser power so as to minimize the effect of local heating on the spectra. In low B-doping concentration wafers, the RS of PS is nearly identical to the bulk c-Si. The inference from the spectra contradicts the usual belief on the existence of Si nanostructures in PS matrix. The variation of RS intensity with the anodization current density is explained on the basis of composite nature of PS.

In high B-doping concentration wafers, the RS of PS is not identical to the respective bulk c-Si wafer. The Fano effect, which is the cause of line-shape asymmetry in bulk c-Si, is identified to be the cause of the line-shape asymmetry in the RS of PS also. For a quantitative understanding of the asymmetry, a curve fitting of the spectra is performed through the Fano function. Following, the effect of anodization current density on the line-shape asymmetry is understood as due to the surface bands.

6.4 REFERENCES

[1] H. Richter, Z. P. Wang, and L. Ley, Solid State Commun. **39**, 625 (1981)

[2] I. H. Campbell and P. M. Fauchet, Solid State Commun. **58**, 739 (1986)

[3] V. Paillard, P. Puech, M. A. Laguna, R. Carles, B. Kohn, and F. Huisken, J. Appl Phys. **86**, 1921 (1999)

TH-1099_04612102

[4] H. Münder, C. Andrzejak, M. G. Berger, U. Klemradt, H. Lüth, R. Herino, and M. Ligeon, Thin Solid Films, **221**, 27 (1992)

[5] Md. N. Islam and S. Kumar, Appl. Phys. Lett. **78**, 715 (2001)

[6] Md. N. Islam, R. N. Panda, A. Pradhan, and S. Kumar, Phys. Rev. B **65**, 033314 (2002)

[7] M. Yang, D. Huang, P. Hao, F. Zhang, X. Hou, and X. Wang, J. Appl. Phys. **75**, 651 (1994)

[8] S. –L. Zhang, X. Wang, K. –S. Ho, J. Li, P. Diao, and S. Cai, J. Appl. Phys. **76**, 3016 (1994)

[9] I. Gregora, B. Champagnon, L. Soviot, and Y. Monin, Thin Solid Films **255**, 139 (1995)

[10] M. A. Ferrara, M. G. Donato, L. Sirleto, G. Messina, S. Santangelo, and I. Rendina, J. Raman Spectrosc. **39**, 199 (2008)

[11] H. Münder, C. Andrzejak, M. G. Berger, T. Eickhoff, H. Lüth, W. Theiss, U. Rossow, W. Richter, R. Herino, and M. Ligeon, Appl. Surf. Sci. **56-58**, 6 (1992)

[12] D. Abidi, B. Jusserand, and J. –L. Fave, Phys. Rev. B **82**, 075210 (2010)

[13] Z. Sui, P. P. Leong, I. P. Herman, G. S. Higashi, H. Temkin, Appl. Phys. Lett. **60**, 2086 (1992)

[14] R. Tsu, H. Shen, and M. Dutta, Appl. Phys. Lett. **60**, 112 (1992)

[15] Y. Kanemitsu, H. Uto, Y. Masumoto, T. Masumoto, T. Futagi, and H. Mimura, Phys. Rev. B **48**, 2827 (1993)

[16] P. H. Khoi, N. T. T. Tam, P. H. Duong, and N. X. Nghai, J. Raman Spectrosc. **30**, 385 (1999)

[17] M. Balkanski, R. F. Wallis, and E. Haro, Phys. Rev. B **28**, 1928 (1983)

[18] J. Menéndez and M. Cardona, Phys. Rev. B **29**, 2051 (1984)

[19] E. Haro, M. Balkanski, R. F. Wallis, and K. H. Wanser, Phys. Rev. B **34**, 5358 (1986)

[20] J. Raptis, E. Liarokapis, and E. Anastassakis, Appl. Phys. Lett. **44**, 125 (1984)

[21] J. P. Russell, J. Phys. Radium **26**, 620 (1965)

[22] J. L. Birman, Phys. Rev. **131**, 1489 (1963)

[23] J. H. Parker, Jr., D. W. Feldman, and M. Ashkin, Phys. Rev. **155**, 712 (1967)

[24] P. A. Temple and C. E. Hathaway, Phys. Rev. B **7**, 3685 (1973)

[25] Z. Iqbal and S. Vepřek, J. Phys. C: Solid State Phys. **15**, 377 (1982)

[26] S. Vepřek, F. –A. Sarott, and Z. Iqbal, Phys. Rev. B **36**, 3344 (1987)

[27] F. Cerdeira, T. A. Fjeldly, and M. Cardona, Phys. Rev. B **8**, 4734 (1973)

[28] F. Cerdeira, T. A. Fjeldly, and M. Cardona, Phys. Rev. B **9**, 4344 (1974)

[29] M. Chandrasekhar, H. R. Chandrasekhar, M. Grimsditch, and M. Cardona, Phys. Rev. B **22**, 4825 (1980)

[30] F. Cerdeira, T. A. Fjeldly, and M. Cardona, Solid State Commun. **13**, 325 (1973)

[31] B. G. Burke, J Chan, K. A. Williams, Z. Wu, A. A. Puretzky, and D. B. Geohegan, J. Raman Spectrosc. **41**, 1759 (2010)

[32] P. Y. Yu, and M. Cardona, Fundamentals of Semiconductors, 3rd ed. (Springer, Berlin, 1996), p. 394

[33] H. R. Philipp and E. A. Taft, Phys. Rev. **120**, 37 (1960)

[34] U. Fano, Phys. Rev. **124**, 1866 (1961)

[35] V. I. Belitsky. A. Cantarero, M. Cardona, C. T. –Giner, and S. T. Pavlov, J. Phys.: Condens. Matter **9**, 5965 (1997)

[36] P. Y. Yu, and M. Cardona, Fundamentals of Semiconductors, 3rd ed. (Springer, Berlin, 1996), p. 397

[37] M. A. Kanehisa, R. F. Wallis, and M. Balkanski, Phys. Rev. B **25**, 7619 (1982)

Indian Institute of Technology Guwahati

TH-1099_04612102

CHAPTER

7

POROUS SILICON MULTILAYER STRUCTURES

So far, the thesis dealt with optical characterizations and optical responses and their interpretations of only single layer PS. This chapter presents the modulations in the electromagnetic wave propagation in multilayer PS structures.

The effective refractive index of PS has been found in Chapter 4 to depend only on the anodization current density when the other etching parameters like B-doping and electrolyte concentration are fixed. It has also been found in the same chapter that the anodization time affects only the thickness of the PS layer without any significant modifications on the microstructure of the material that has already been formed. That would mean the removal of Si atoms is predominantly at the PS/c-Si wafer interface. A modulation in the anodization current density in time would result in PS layers of different effective refractive indices in depth. These formation characteristics of PS are exploited in preparing PS multilayer structures with desired (effective) refractive indices and thicknesses.

PS multilayer structures are a class of dielectric multilayer structures. Dielectric multilayer structures have long been known in optics, and have a few commercial applications like optical filters, anti-reflection coatings, etc [1-4]. The specular reflectance

TH-1099_04612102

and transmittance of an electromagnetic wave on such structures can be calculated by transfer matrix (T-matrix) method [2-4].

The fact that dielectric multilayer structures can be made with ease using PS is known from the very early years of the discovery of PL from the material [5]. Since then, several complex multilayer structures have been realized using PS like UV filters [6], dielectric Bragg mirror [7], wideband mirrors [8], omnidirectional mirrors [9, 10], Rugate filters [11-13], coupled microcavity [14, 15], Fibonacci structure [16, 17], Thue-Morse structure [18, 19], and Wainner-Stark ladder [20-22], to mention a few. The present chapter deals with the extent of modulations in single layer optical response in the course of preparing the multilayer structures. For this purpose only simple multilayer structures of the form alternating high and low refractive index layers are considered. The prepared multilayer structures are characterized using specular reflectance measurements. The spectra are then compared with the theoretical simulations using T-matrix method.

7.1 CHOICE OF WAFER RESISTIVITY

Multilayer PS structures can be made on any resistivity c-Si wafer. However, as the structural and optical properties of PS are different on different resistivity c-Si wafers, for a good optical response and due to some practical constraints, only certain resistivity wafers are suitable for the preparation of multilayer structures. The factors that are considered for the choice of wafer resistivity to prepare multilayer PS structures are (i) good mechanical stability of the structure (ii) large variation in effective refractive index within the attainable anodization current density values (iii) low growth rate (iv) minimal effect of surface adsorbed chemical species on the effective refractive index and (v) less scattering and absorption losses.

It is from practical experience that the PS prepared on high resistivity c-Si wafers are very unstable especially when prepared using high anodization current densities. From the knowledge of optical characterizations of single layer PS, it has been found that the effective refractive index of those PS is largely contributed by the surface adsorbed chemical species that vary over time and also with the chemical species present in the ambient. These are the dominant factors that make the PS prepared on high resistivity c-Si wafers unsuitable for the preparation of multilayer structures. Of less dominant, the change

TH-1099_04612102

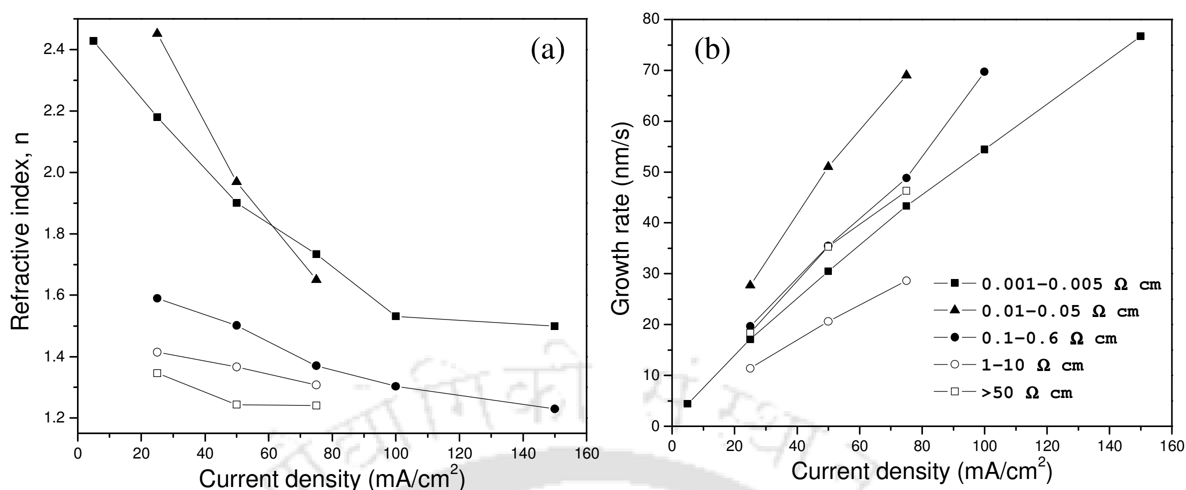

Figure 7.1 Effect of anodization current density on (a) effective refractive index at 700 nm radiation and (b) growth rate of PS prepared on various c-Si wafer resistivities.

in effective refractive index over the attainable range of anodization current densities is small as can be seen in Fig. 7.1(a). Figure 7.1(a) is a reproduction of Fig. 4.19(b) for ready reference.

On the other hand, PS prepared on low resistivity c-Si wafers are very stable, and their effective refractive indices are unaffected by the surface adsorbed chemical species. PS prepared on both 0.001–0.005 and 0.01–0.05 Ω cm resistivity c-Si wafers bear these features. The variation in effective refractive index with anodization current density is also appreciable on both these wafers. However, when considering the growth rate with anodization current density, PS prepared on 0.001–0.005 Ω cm resistivity c-Si wafer is more suitable for the preparation of multilayer PS structures due to its slow growth rate as can be seen in Fig. 7.1(b). Figure 7.1(b) is a reproduction of Fig. 4.19(a) for ready reference.

7.2 CHOICE OF REFRACTIVE INDEX AND GROWTH RATE

The necessary factors that are to be considered in preparing good optical response PS multilayer structures have already been given in the previous section (Section 7.1). The refractive index contrast between the layers should be high whereas, the growth rates of the individual layers should not be too high. The PS layers that satisfy these conditions are

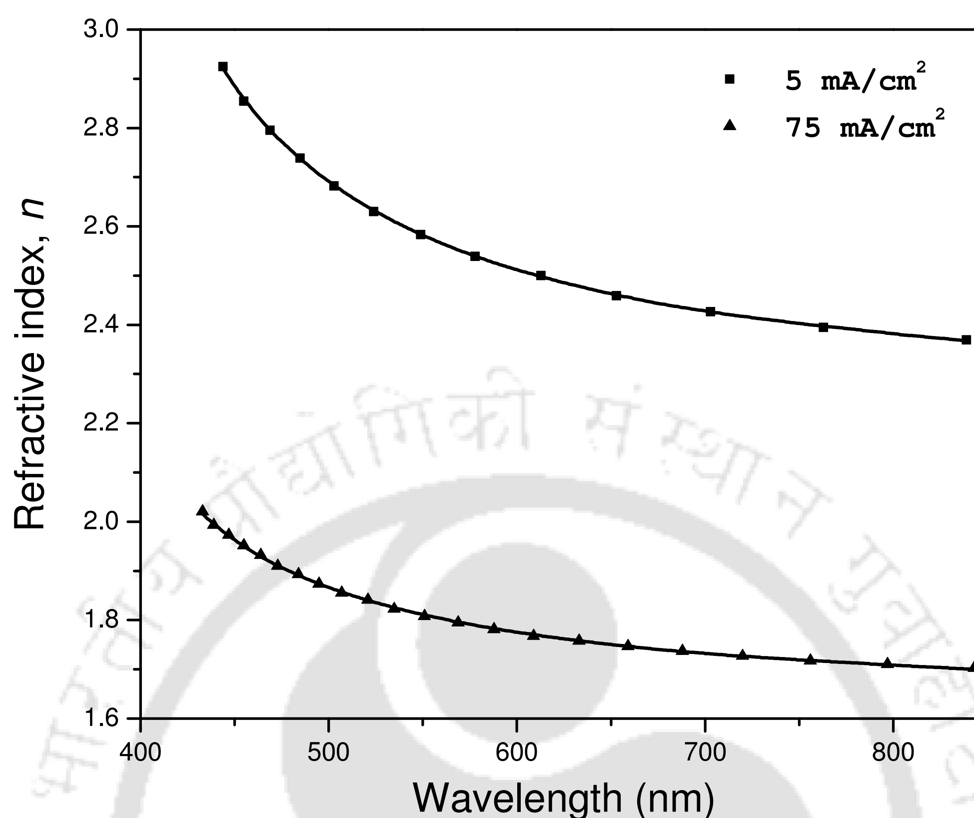

Figure 7.2 Dispersions of effective refractive indices of PS prepared on c-Si wafers of resistivity 0.001–0.005 Ω cm under 5 (top) and 75 (bottom) mA/cm^2 anodization current density. The discrete data points shown as symbols are experimental points and the continuous lines are the fit through Bruggeman's EMT.

Table 7.1 Details of anodization current density and time for the preparation of high and low refractive index layers, and their thicknesses and growth rates.

Anodization current density (mA/ cm^2)	Anodization time (sec)	Thickness (µm)	Growth rate (nm/sec)
5	210	1.0077	4.8
75	30	1.3420	44.7

the layers prepared on c-Si wafers of resistivity 0.001–0.005 Ω cm using 5 and 75 mA/cm^2 anodization current densities. Figure 7.2 shows the dispersions of refractive indices and Table 7.1 gives the growth rates of these PS layers. If, instead of 75 mA/cm^2, PS prepared using 100 mA/cm^2 anodization current density is considered, the refractive index contrast would be good, but as the growth rate is too high, it would be difficult to control.

TH-1099_04612102

The refractive indices and growth rates of PS for the two anodization current densities are determined using the procedure discussed in Chapter 3. Figure 7.2 shows the dispersion of refractive indices for 5 and 75 mA/cm^2 anodization current density and the Table 7.1 shows the growth rates of these PS along with the details of preparation conditions.

7.3 PS MULTILAYER STRUCTURES

The PS multilayer structures that are discussed in the following section consist of only two layers of differing optical properties – high and low refractive index layer. The high and low refractive index layers are prepared by 5 and 75 mA/cm^2 anodization current density, respectively. The spectral feature in the reflectance of PS multilayer structures like dielectric Bragg mirror and single microcavity are discussed in relation to the theoretical simulations of the identical structure using T-matrix method.

7.3.1 Dielectric Bragg mirror

Dielectric Bragg mirror (DBM) is a dielectric multilayer structure to produce nearly 100 % reflectance for a band of wavelengths in the electromagnetic spectrum. A schematic of the cross section of DBM is shown in Fig. 7.3. In order to have the reflectance band centred at λ_0, the individual layers must have their optical thicknesses equal to $\lambda_0/4$.

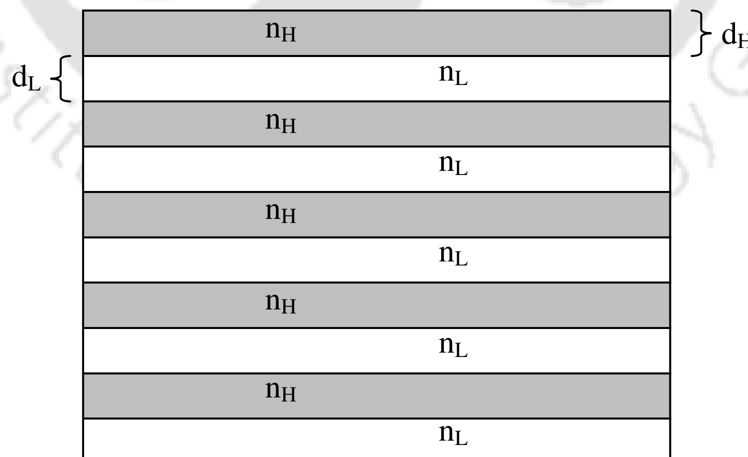

Figure 7.3 A schematic of the cross section of a free standing DBM of 5 periods. A period consists of one n_H and n_L layers. n_H (n_L) and d_H (d_L) are the refractive index and thickness of high (low) refractive index layers, respectively where $d_H = \lambda_0/4n_H$ and $d_L = \lambda_0/4n_L$ and λ_0 is the centre of the reflectance band.

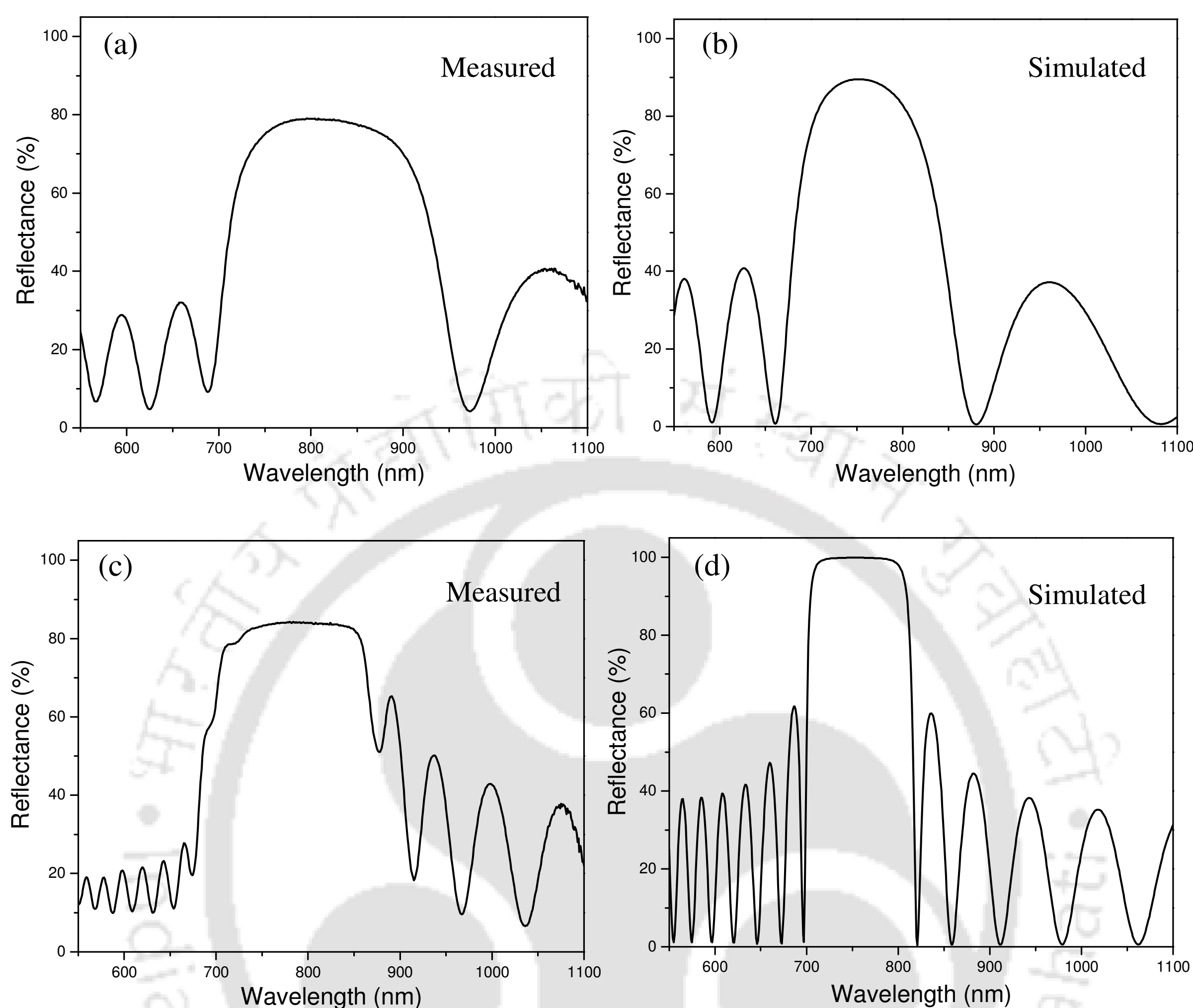

Figure 7.4 Measured specular reflectance spectra (left) of PS DBMs are compared with the theoretical simulations (right) of identical structures. The theoretical simulations are performed using T-matrix method. The high refractive index layers are prepared with 5 mA/cm^2 anodization current density for 20 sec and the low refractive index layers are prepared with 75 mA/cm^2 anodization current density for 3 sec. The estimated thicknesses of high and low refractive index layers are 86 and 109 nm, respectively. The DBM structure can be given in short as $[HL]^5$ for (a) and (b) and $[HL]^{15}$ for (c) and (d) where H and L denote high and low refractive index layers, respectively.

Two PS DBMs are prepared with differing number of periods – 5 and 15 periods. In Fig. 7.4, the measured specular reflectance spectra of PS DBMs are compared with the theoretical simulations of identical structures. For the purpose of simulation, the layers are considered to be homogeneous and transparent. So the magnitudes of the simulated spectra

TH-1099_04612102

are not affected by scattering and absorption, which are in real materials. The dispersions of refractive indices and thicknesses as obtained from single layer characterizations are used as inputs for the simulation.

It is observed in Fig. 7.4 that the prepared PS DBMs show strong reflection bands with their centres near around 800 nm. However, neither the reflectance band centre nor the width of the measured spectra clearly matches with the simulations. Also, the strong reflectance band in the prepared PS DBMs slightly blue-shifts with the increase of number of periods and in the simulation, no such shifts in the reflectance band with the increase of number of periods is observed. These mismatches in the band centre between the measurement and simulation and the blue-shift with the increase in number of periods would imply that the anodization process affects both the refractive index and thickness of multilayer structures. Only in the case of anodization with a fixed anodization current density, the removal of Si atoms is predominant at the PS/c-Si wafer interface. When there is a modulation in anodization current density, the higher anodization current density could remove the Si atoms from the layers that have already been anodized with lower anodization current density. In the process, the thicknesses of the layers prepared by both high and low anodization current densities and the refractive index of the layers prepared by low anodization current density are affected. However, the strong reflection band, which is the characteristic feature of a DBM, could still be retained very close to the predicted spectral range.

The mismatch in the reflectance band width between the measurement and simulation is a clear indication of the interfacial refractive index of PS layers is different from the bulk refractive index. In the simulations, it has been considered that the interfacial refractive index is same as that of the bulk of the layer despite an earlier note in Chapter 3 that in composite systems, the refractive indices at the boundaries are not same as that of the bulk of the material. It is only because the interfacial refractive indices could not be determined in the PS system and prior to this work, it has not been noted that the interfacial refractive indices could be different from the bulk of the material. These results could be considered as an explicit show up of the differences in the interfacial and bulk refractive indices. The wider band width of the measured spectra, in comparison with the simulated spectra, would imply that the actual reflectance at the boundaries of the layers is much stronger than that expected when the bulk and interfacial refractive indices are same.

7.3.2 Single microcavity

Single microcavity (SMC) is a specially designed dielectric multilayer structure that would forbid a band of wavelengths from propagating through the structure, but allows a very narrow region of the band centred at λ_0 to propagate through the structure. A schematic of the cross section of SMC is shown in Fig. 7.5.

The prepared PS SMC consists of 5 periods before and after the cavity layer. The refractive index of the cavity layer is same as that of the high refractive index layer with its thickness being doubled that of the high refractive index layer. In Fig. 7.6, the measured specular reflectance spectrum of PS SMC is compared with the theoretical simulation of identical structure. In this case also the layers are considered to be homogeneous and non-absorbing and the dispersions of refractive indices and thicknesses as the inputs for the simulation.

In Fig. 7.6(a), the narrow dip near around 800 nm in the reflectance band of the measured spectrum is an indication of the electromagnetic wave propagation into the structure. This feature can also be seen in the simulated spectrum under identical structure as in Fig. 7.6(b), however, at a slightly different wavelength position (~ 753 nm). The cavity wavelength is at the centre of the reflectance band in the simulation, whereas it is

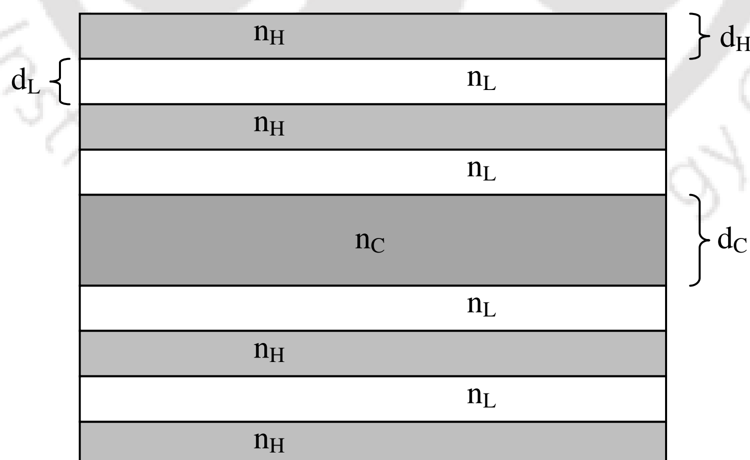

Figure 7.5 A schematic of the cross section of a free standing SMC with 2 periods before and after the cavity layer. n_H (n_L and n_C) and d_H (d_L and d_C) are the refractive index and thickness of high (low and cavity) refractive index layers, respectively where $d_H = \lambda_0/4n_H$, $d_L = \lambda_0/4n_L$ and $d_C = \lambda_0/2n_C$ and λ_0 is the centre of the reflectance band.

TH-1099_04612102

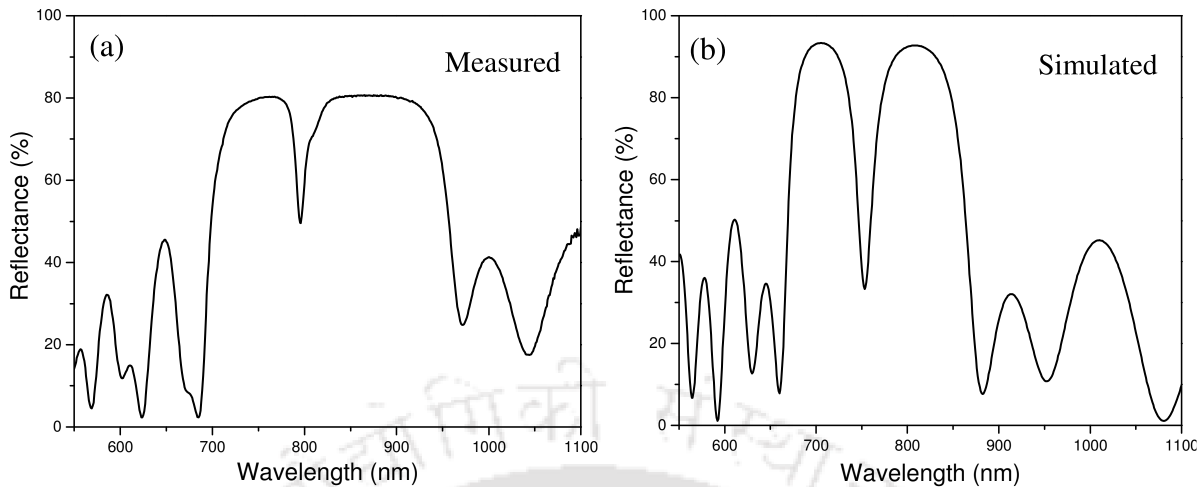

Figure 7.6 Measured specular reflectance spectra (left) of PS SMC is compared with the theoretical simulation (right) of identical structure through T-matrix method. PS SMC consists of 5 periods before and after the cavity layer. The high refractive index layers are prepared with 5 mA/cm^2 anodization current density for 20 sec and the low refractive index layers are prepared with 75 mA/cm^2 anodization current density for 3 sec. The estimated thicknesses of high and low refractive index layers are 86 and 109 nm, respectively. The cavity layer is prepared with 5 mA/cm^2 anodization current density for 40 sec. The SMC structure can be given in short as $[HL]^5HH[LH]^5$ where H and L denote high and low refractive index layers, respectively.

off-centred in the measured spectrum. These differences in the cavity between the measurement and the simulation are due to the changes in the bulk refractive index of low refractive index layers and the thicknesses of both high and low refractive index layers with the anodization process as seen in the case of DBMs. In additions to the shift of the cavity wavelength, the strong reflectance band in the simulated spectrum is not as broad and as flat as in the measured spectrum. These differences between the spectra are due to the poor prediction of the reflectance at the interfaces of the layers as the bulk refractive indices of the layers are used for the interfaces as well.

7.4 SUMMARY

To summarize, of the c-Si wafer resistivities, it is identified that PS prepared on 0.001-0.005 Ω cm resistivity wafer is better suitable for the preparation of multilayer PS structures. The PS multilayer structures are of the form of alternating high and low

refractive index layers. Before preparing the multilayer structures, the high and low refractive index layers prepared using 5 and 75 mA/cm^2 anodization current density, respectively are characterized for the refractive index and growth rate with the procedure described in Chapter 3. From the knowledge of refractive indices and growth rates of single layer PS prepared using 5 and 75 mA/cm^2 anodization current densities, PS multilayer structures like DBMs and SMC are prepared. The measured specular reflectance spectra of the PS multilayer structures are compared with the theoretical simulations using T-matrix method. The measured reflectance spectra of PS multilayer structures do not match exactly with the simulations; however, the features like reflectance band in the case of DBM and a narrow spectrum of propagating electromagnetic wave in the case of SMC are clearly observed. The mismatches in the spectra between the measured and the simulations are understood based on the changes introduced in the microstructure of PS that have already been anodized with the low anodization current density when performing the anodization with high anodization current density and the interfacial refractive index being different from the bulk refractive index.

7.5 REFERENCES

[1] P. Baumeister and G. Pincus, Sci. Amer. **223**, 59 (1970)

[2] M. Born and E. Wolf, Principles of Optics 7th ed. (Cambridge University Press, Cambridge, 1999), p. 386

[3] E. Hecht, Optics 4th ed. (Addison Wesley, San Francisco, 2002), p. 425

[4] A. K. Ghatak and K. Thyagarajan, Optical Electronics (Cambridge University Press, Cambridge, 1989), p. 57

[5] M. G. Berger, C. Dieker, M. Thönissen, L. Vescan, H. Lüth, H. Münder, W. Theiβ, M. Wernke, and P. Grosse, J. Phys. D: Appl. Phys. 27, 1333 (1994)

[6] D. Becerra and V. Agarwal, phys. stat. sol. (c) **4**, 1956 (2007)

[7] M. B. H. Breese and D. Mangaiyarkarasi, Opt. Express **15**, 5537 (2007)

[8] V. Agarwal and J. A. D. Rio, Appl. Phys. Lett. **82**, 1512 (2003)

[9] J. O. Estevez, J. Arriaga, A. M. Blas, and V. Agarwal, Appl. Phys. Lett. **94**, 61914 (2007)

[10] J. O. Estevez, J. Arriaga, A. M. Blas, and V. Agarwal, Appl. Phys. Lett. **93**, 191915 (2008)

TH-1099_04612102

[11] L. Moretti, I. Rea, L. Rotiroti, I. Rendina, G. Abbate, A. Marino, L. D. Stefano, Opt. Express **14**, 6264 (2006)

[12] M. B. H. Breese and D. Mangaiyarkarasi, Opt. Express **15**, 5537 (2007)

[13] L. Pavesi, G. Panzarini, and L. C. Andreani, Phys. Rev. B **58**, 15794 (1998)

[14] M. Ghulinyan, C. J. Oton, L. D. Negro, L. Pavesi, R. Sapienza, M. Colocci, D. S. Wiersma, Phys. Rev. B **71**, 094204 (2005)

[15] R. Sapienza, P. Costantino, D. Wiersma, M. Ghulinyan, C. J. Oton, L. Pavesi, Phys. Rev. Lett. **91**, 263902 (2003)

[16] V. Agarwal, J. A. D. Río, G. Malpuech, M. Zamfirescu, A. Kavokin, D. Coquillat, D. Scalbert, M. Vladimirova, and B. Gil, Phys. Rev. Lett. **92**, 097401 (2004)

[18] L. Moretti, I. Rea, L. Rotiroti, I. Rendina, G. Abbate, A. Marino, L. D. Stefano, Opt. Express **14**, 6264 (2006)

[19] V. Agarwal, M. E. M. –Ramos, J. Phys. D: Appl. Phys. **40**, 1 (2007)

[20] R. Sapienza, P. Costantino, D. Wiersma, M. Ghulinyan, C. J. Oton, L. Pavesi, Phys. Rev. Lett. **91**, 263902 (2003)

[21] V. Agarwal, J. A. D. Río, G. Malpuech, M. Zamfirescu, A. Kavokin, D. Coquillat, D.Scalbert, M. Vladimirova, and B. Gil, Phys. Rev. Lett. **92**, 097401 (2004)

[22] M. Ghulinyan, C. J. Oton, Z. Gaburro, L. Pavesi, C. Toninelli, D. S. Wiersma, Phys. Rev. Lett. **94**, 127401 (2005)

CHAPTER

8

CONCLUSIONS AND FUTURE SCOPES

Several investigations on the optical properties of PS exist in the literature. However, the present thesis differs from several of those investigations by comparing the measured data with the simulation, which is still not considered to be a very common practice. Based on these investigations, there are a few conclusions, which were not in the literature prior to this work. This chapter presents those conclusions and the future prospects of the investigations carried in the thesis work.

8.1 THESIS CONCLUSIONS

The overall conclusions from the thesis chapters are given below:

- Interference conditions of multiple beam interference pattern in thin films are unaffected by random inhomogeneity and interfacial roughness. When the determination procedures of refractive index and thickness are based only on the interference conditions, they are applicable to all thin films.
- Optical absorption is strongly influenced by inhomogeneity and interfacial roughness. On materials with inhomogeneity and interfacial roughness, the optical absorption could be understood in relation to incoherent spectral scattering.

TH-1099_04612102

- Optical constants of Si in PS are same as that of the bulk c-Si. The porous nature of the material affects only the effective refractive index, but not the refractive index of the microscopic Si regions in PS.
- Efficient visible PL of PS cannot be ascribed only to the chemisorbed reactive chemical species at the porewalls as they form the electronic states for the radiative recombination of the carriers. On the other hand, the Si regions in PS cannot be neglected as they posses the bulk optical properties of c-Si, where this phenomenon is not possible due to its indirect bandgap of 1.12 eV. The absorption states are the electronic states of bulk c-Si and the emission states are the electronic states of the reactive chemical species at the porewalls. As the phenomenon requires both the presence of c-Si regions and the reactive chemical species, PL is an emergent property due to the composite nature of PS.
- The studies on single layer optical properties of PS could only provide a qualitative picture of the optical response of multilayer PS structures.

8.2 SCOPE FOR FUTURE

A few scopes for future based on the present investigation are given below

- Development of determination procedures for interfacial refractive indices of practical thin films.
- Development of determination procedures for incoherent spectral scattering and extinction coefficient to explore newer scattering phenomena.
- Studies on the microstructure of PS with high resolution microscopes. This study, together the knowledge of the variations of growth rate and effective refractive index of PS with anodization current density and B-doping concentrations, would throw light on the formation kinetics of PS.
- Studies on the structural and optical properties of PS prepared on polycrystalline Si wafers. This study would be interesting as the carriers' transport is affected, in addition to the pore geometry, by the grain boundaries. Due to this additional spatial restriction in the transport of carriers, quantum confinement effects may visually be seen.

TH-1099_04612102

APPENDIX

The mathematical steps in the determination of interference fringe order *m* and the thickness *d* for the case of transmittance geometry are given here.

Determination of interference fringe order, m

Consider the interference conditions in the normal incidence transmittance spectrum for two adjacent interference orders

$$2\, d\, n_1 = \Omega\, \lambda_1 \tag{A.1}$$

$$2\, d\, n_2 = (\Omega - 0.5)\, \lambda_2 \tag{A.2}$$

where Ω is the interference order, which is to be determined.

From Eqs. (A.1) and (A.2), Ω is given as

$$\Omega = \frac{0.5\, \lambda_2}{(\lambda_2 - \lambda_1)} - \frac{2\, d\, (n_1 - n_2)}{(\lambda_2 - \lambda_1)} \tag{A.3}$$

In optically thin region of the spectrum, the denominator of second term, in Eq. (A.3), is several times greater than the numerator, and so Eq. (A.3) can be reduced to

$$\Omega_0 = \frac{0.5\, \lambda_2}{(\lambda_2 - \lambda_1)} \tag{A.4}$$

where the subscript ‘0’ is to indicate the approximation.

TH-1099_04612102

Determination of film thickness, *d*

For the determination of d, two spectral measurements at two different angles of incidence are necessary. In the following, the mathematical formulae are given for the case of one normal incidence transmittance and one oblique incidence reflectance measurements.

The interference conditions for the transmittance and the reflectance at a particular interference fringe order Ω would be given as

$$2\,d\,n_1 = \Omega\,\lambda_1 \qquad \text{(Transmittance)} \qquad \text{(A.5)}$$

$$2\,d\,(n_1^2 + \gamma - \sin^2\theta_1)^{1/2} = \Omega\,\lambda_2 \qquad \text{(Reflectance)} \qquad \text{(A.6)}$$

where Ω is the interference fringe order at λ_1 and λ_2 and γ compensates the dispersion of refractive index between λ_1 and λ_2.

From Eqs. (A.5) and (A.6), d would be given as

$$d = \left[\frac{\Omega^2\,(\lambda_1^2 - \lambda_2^2)}{4\,(\sin^2\theta_1 - \gamma)}\right]^{1/2} \qquad \text{(A.7)}$$

Since Eq. (A.7) contains an undetermined parameter γ, d is not calculable from Eq. (A.7). If $\gamma = 0$, then, Eq. (A.7) reduces to

$$d_0 = \left[\frac{\Omega^2\,(\lambda_1^2 - \lambda_2^2)}{4\,\sin^2\theta_1}\right]^{1/2} \qquad \text{(A.8)}$$

where the subscript '0' is to indicate the approximation.

Now, d_0 is although calculable and a close estimate of d, it can only be considered as a first step in the determination of d. A better estimation of d can be made through Eq. (A.7) once γ is found.

For the determination of γ, consider the interference condition, adjacent to the interference fringe order Ω, in the normal incidence transmittance, which is given as

$$2\,d\,(n_1^2 + \delta)^{1/2} = (\Omega + 0.5)\,\lambda_3 \qquad \text{(Transmittance)} \qquad \text{(A.9)}$$

where δ compensates the dispersion of refractive index between λ_1 and λ_3.

From Eqs. (3.16) and (3.20), δ would be given by

$$\delta = \frac{(\Omega + 0.5)^2\,\lambda_3^2 - \Omega^2\,\lambda_1^2}{4\,d^2} \qquad \text{(A.10)}$$

TH-1099_04612102

Considering the refractive index dispersion of the form $1/\lambda^p$, γ would be given as

$$\gamma = \frac{\delta\, \lambda_3^p\, (\lambda_2^p - \lambda_1^p)}{\lambda_2^p\, (\lambda_3^p - \lambda_1^p)} \tag{A.11}$$

Equations (A.7), (A.8), (A.10) and (A.11) are the necessary mathematical formulae for the determination of *d*. These equations are used in the iteration to obtain *d*. The flow chart of the iteration is given in Fig. A.1.

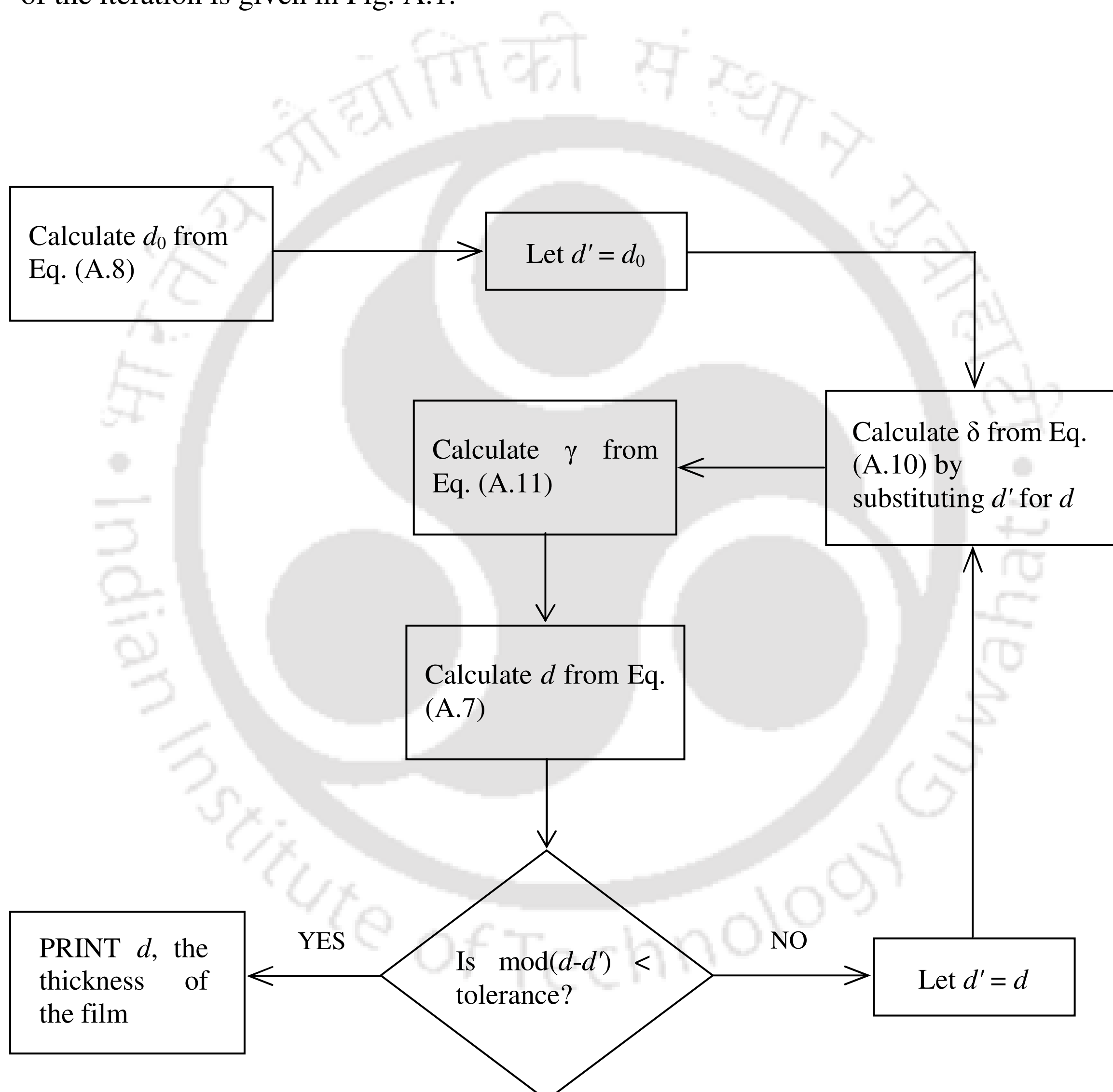

Figure A.1 Flow chart of the iterative procedure for the determination of film thickness *d*.

TH-1099_04612102